Analytical and Simulation Modeling of Terahertz Waveguides and Sensors based upon Plasmonic and Metamaterial Structures

A Dissertation submitted to the
Indian Institute of Technology, Guwahati
For the Degree of Doctor of Philosophy

Maidul Islam

INDIAN INSTITUTE OF TECHNOLOGY GUWAHATI
THz Photonics and Plasmonics Laboratory
Department of Physics
Indian Institute of Technology Guwahati
Assam - 781039, India
December 2017

Dedicated To My Beloved Parents

Declaration

Maidul Islam
THz Photonics and Plasmonics Lab
Roll No. 146121014
Department of Physics
Indian Institute of Technology Guwahati
Guwahati, India

I hereby declare that the results embodied in this thesis are the results of simulation and theory carried out by me at the Department of Physics, Indian Institute of Technology Guwahati (IIT G), in India under the supervision of **Dr. Gagan Kumar**. This thesis has not been submitted to any university/ institute or elsewhere for the award of any degree, diploma or associateship.

Maidul Islam

Date

Certificate

Dr. Gagan Kumar
Associate Professor
Department of Physics
Indian Institute of Technology Guwahati
Guwahati, India
email:gk@iitg.ernet.in

This is to certify that the work contained in the thesis entitled "**Analytical and Simulation Modeling of Terahertz Waveguides and Sensors based upon Plasmonic and Metamaterial Structures**" by **Mr. Maidul Islam** (Roll No. 146121014), a student of Department of Physics, Indian Institute of Technology Guwahati (IIT G) for the award of degree of Doctor of Philosophy, has been carried out under my supervision.

The present thesis or any part thereof has not been submitted elsewhere for award of any other degree, diploma or associateship.

Gagan Kumar

Date

ABSTRACT

Plasmonics and metamaterials have emerged as one of the most fascinating areas in photonics because of their significance in developing next generation miniaturized high speed components and sensitive devices. In the thesis work, the focus has been made in investigating the potential of plasmonic and metamaterial structures in the design and construction of terahertz waveguides and thin film sensors.

We have proposed a planar plasmonic terahertz waveguide comprising of one-dimensional array of sub-wavelength scale periodically arranged tilted pillars, where the propagation properties of the terahertz modes can be controlled through the bending of pillars. It is possible to propagate the terahertz wave more efficiently in a particular direction than the other with the proposed waveguide design. The ability to confine terahertz modes at a position where incident frequency becomes equal to the natural frequency of structures has been also discussed in the waveguide geometry.

In plasmonic terahertz waveguides, we have also investigated the role of internal corrugations in altering the propagation properties of the guided terahertz modes. The internal corrugations are found to effectively change the propagation properties and switch the propagation response from multimode to single mode for certain parameters of the structures. The role internal corrugations in slowing down the terahertz has also been comprehensively discussed.

We further investigate the potential of planar plasmonic terahertz waveguides as thin film sensors. In this novel study, we designed a plasmonic waveguide comprising of periodic rectangular grooves and filled them with analytes of different refractive indices. Various sensing parameters such as frequency shift, sensitivity and figure of merit of the fundamental plasmonic modes have been analyzed to establish the sensor characteristics of the proposed geometry. In order to explore

better sensing characteristics of the plasmonic waveguide, we have also examined the role of V-groves and compared results with the rectangular grooves.

The potential of planar terahertz metamaterials as thin film sensors has been widely investigated in last few years. In this context, several metamaterial configurations have been devised to effectively sense an analyte. We have examined the role of fundamental and higher-order resonances as thin film terahertz sensor. For this purpose, we have used a single split ring resonator (SRR) based terahertz metamaterial, which exhibits fundamental and higher order resonance modes subject to the polarization of electric field vector of incident terahertz radiation with respect to the gap of SRR. We have compared various sensing parameters for different resonances to understand their role and their effectiveness as a thin film terahertz sensor.

In order to understand and analyze the numerical observation in our study, we have modeled plasmonic and metamaterial structures with a semi-analytical transmission line approach.

ACKNOWLEDGEMENTS

I would like to pay heartiest thanks and regards to my thesis supervisor **Dr. Gagan Kumar** for his continuous support and help throughout my PhD work. This work would not be possible without his guidance, support and encouragement.

Next, I would like to thank Dr. Dibakar Roy Chowdhury for his active support and direct involvement in the research projects. Also, I thank Dr. Amir Ahmad for his fruitful comments and advice in the research work.

Then I would like to thank the rest of my thesis committee: Dr. Amarendra Kumar Sarma, Dr. Dilip Pal, Dr. Parameshwar K. Iyer for their encouragement, insightful comments, and suggestions.

My sincere thanks also go to the former and present HoDs of Physics, Prof. Saurabh Basu and Prof. Poulose Poulose for providing the opportunity to utilize different resources of the department for my PhD work.

Thanks to entire staff of the Department of Physics, IIT Guwahati.

I thank my friends in my surroundings: Koijam Monika Devi, S. Jagan Mohan Rao, Dr. Md. Gaffar, Dr. Sk. Obaidullah, Dr. Rashidul Islam, Md. Rezwan Habib, Nawaz Sarif Mallick, Alankrit Tomar, and Lakshya Gautam for the stimulating discussions and for the fun that we have during the PhD work.

I take this opportunity to sincerely acknowledge the financial support from Ministry of Human Resource and Development (MHRD), Government of India during my PhD.

Last but not the least, I would like to thank my parents, Mr. Faizul Islam and Mrs. Momataj Islam, for their support and inspiration throughout my research work. Their infallible love and support have always been my strength. Their patience and sacrifice will remain my inspiration throughout my life. I would also like to thank my dearest brother Mr. Mominul Islam. I want to express my gratitude to my dearest Mrs. Kostury Khatun for immense mental support and love.

And, finally my whole life including PhD work is dedicated to almighty **GOD, ALLAH**.

Contents

List of Figures

List of Tables

Chapter 1

Introduction

Contents

Terahertz (THz) frequencies have evolved as one of the most interesting and fascinating areas of research in last decade. The terahertz regime covers a very narrow region (0.1-10 THz) in the electromagnetic spectrum between the microwave and infrared region as indicated in Fig. 1.1. This region is also known as THz gap because of the lack of devices and components that are commonplace in other regions of the electromagnetic spectrum. The radiation of 1 THz has a period of 1 ps, a wavelength of 300 μm, a wave number of 33 cm^{-1} and a photon energy of 4.1 meV. The terahertz radiations are also known as T-rays and exhibit properties just like other electromagnetic radiations [1]. THz regime invites ap-

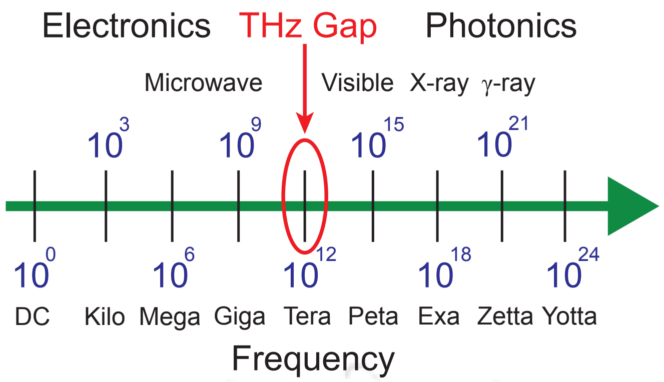

Figure 1.1: Schematic of THz region in the electromagnetic spectrum. The narrow region is termed as the THz gap as shown in the red color.

plications from both the electronics and photonics regions as it falls in the middle of them. The propagation of terahertz waves in a medium can be governed by Maxwell's equations. One of the beauty with THz waves is that they exhibit low photon energies and thus can't lead to the photoionization in biological tissues contrary to the X-rays. Therefore even if THz waves do cause any harm, then it is limited to the skin level. Therefore, terahertz radiations enable doctors to examine deep into tissues without any damaging effects. THz radiations can also detect differences in water content and density of a tissue. At THz frequencies, many molecules exhibit strong absorption and dispersion due to their rotational and vibrational transitions. These transitions are specific to the molecule and therefore enable spectroscopic finger-printing in the THz band [2]. The terahertz waves are also promising in imaging applications and therefore, they are capable of providing the structural information on a target along with the information on its constituents [3, 4]. Further, THz waves are transparent to most of the dielectric materials, such as cloth, paper, wood, and plastic etc., therefore, these waves are very useful for screening passengers at airports and prevention of criminal offenses. THz spectroscopy has the ability to characterize the electronic, vibrational and compositional properties of solids, liquids, and gases. With the use of terahertz radiations, it is also possible to distinguish plastic explosives concealed in a suitcase [5]. Furthermore, the detection of a binding state of the genetic materials such as DNA and RNA [6] using terahertz waves allow us a label-free method for the genetic analysis for future biochip technologies. In Fig. 1.2, some of the potential applications of terahertz waves have been highlighted, which have been investigated in last few years. The terahertz waves can potentially uncover the concealed weapons that criminal offenders carry at the places of national security importance. Fig. 1.2 (a) shows one such image of screening of a passenger usually carried out at the airports. Terahertz radiations have also great significance in medical applications. In Fig. 1.2 (b), the medical diagnosis of a cavity inside the teeth using THz imaging technology is shown. In medical operations also, the use of THz radiations is increasing because of the safe and invasive features associated with terahertz waves (Fig. 1.2 (c)).

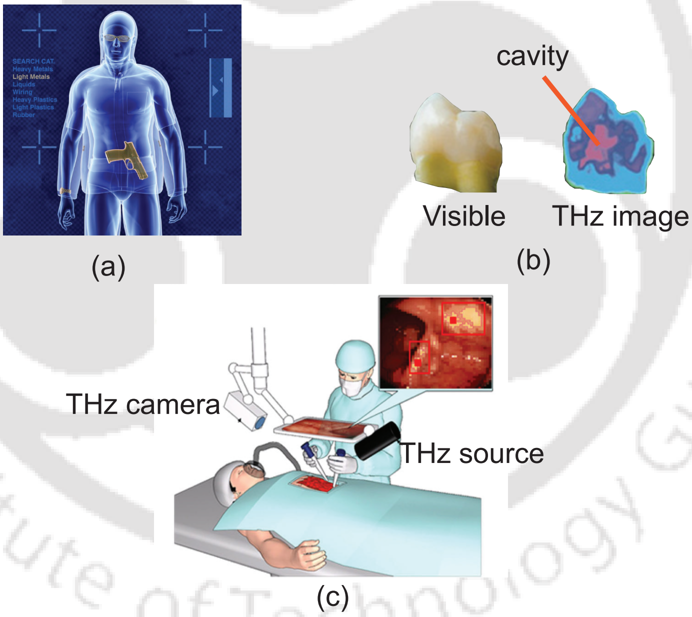

Figure 1.2: Some terahertz applications. (a) Shows identification of gun during security screening of a passenger at the airport. (`http://physicsworld.com/cws/article/news/2012/jun/12/new-tuner-could-bring-terahertz-to-the-masses`) (b) Depicts medical diagnosis of cavity inside the tooth using THz imaging. (`http://www.teraview.com/applications/medical/oral-healthcare.html`) (c) It indicates the application of terahertz radiation in medical operation.

The generation of broadband terahertz radiations and the detection of information carrying signals is extremely important to study of various terahertz applications. There are a variety of methods that can result in the generation of terahertz pulses. This includes photoconductive antennas, four-wave mixing in gaseous plasmas, photo-dember effect, optical rectification in nonlinear crystals viz. ZnTe, GaP, LiNbO3 etc [7–10]. The photoconductive (PC) antenna is one of the most frequently used components for the generation of terahertz waves. The antenna consists of two metal electrodes that are coated on a semiconductor substrate, Lt-GaAs with a small gap between them. A voltage source is connected to the two electrodes. In order to generate THz pulses, femtosecond laser pulses of suitable wavelength are incident into the gap, which results in the generation of charge carriers. The biased voltage results in the transient current density which his given by $J(t) = N(t)e\mu E_b$, where $N(t)$ is the density of the photo-carriers generated, e is the electronic charge, μ is the mobility of the carriers and E_b is the applied electric field. Since the photocurrent varies in time, it generates an electromagnetic pulse, whose electric field is proportional to $\partial J(t)/\partial t$ which is proportional to $\partial N(t)/\partial t$. Therefore, more the carriers are generated by the femtosecond pulse, stronger is the radiated terahertz field. It should be noted that other parameters such as bias voltage, materials properties as well as the areas between the transmission lines also plays an important role in defining the bandwidth as well as the radiated electromagnetic field.

Optical rectification is another widely used approach for the generation of terahertz pulses which has the advantage of extremely broad spectral bandwidth. Optical rectification is a second-order nonlinear optical effect. It is basically a difference-frequency generation with the frequency difference close to zero. Typically, femtosecond laser pulses are used to generate THz from Electro-optic (EO) crystals via optical rectification. Because a femtosecond pulse contains many frequency components, any two frequency components contribute to the difference-frequency generation, and the overall result is the weighted sum of all the contributions.

For probing terahertz, both coherence and incoherent techniques are used. For coherent detection, photoconductive antenna and electro-optic (EO) sampling are the most commonly used techniques. In a photoconductive antenna, femtosecond laser pulses and terahertz waveforms are mixed together in the antenna and transient current is measured to probe the terahertz pulses. The electro-optic sampling is based upon the Pockels effect [11]. The electric field of terahertz pulses is measured through a change in the optical polarization of the femtosecond pulses. Both the techniques have widely been investigated in last two decades. In the incoherent detection methods pyroelectric detectors, bolometers, and Golay cells are widely used for measuring the power of terahertz radiations [3, 12, 13].

1.1 Terahertz waveguides

The waveguides are essential ingredients to a variety of applications ranging from medical science to communication networks and systems. In terahertz regime, enormous efforts have been made to develop active and passive guided wave components. Several wave-guiding schemes have been exercised to transfer terahertz waves exhibiting low loss and high confinement of the modes aiming applications in diversified areas, which include metallic circular waveguides [14], parallel plate waveguides [15], metal wire waveguide [16], parallel plate photonic waveguides [17], polymer tube based THz waveguide [18] etc. For the construction of terahertz waveguides, both dielectric and metal substrates have been employed.

1.1.1 Terahertz waveguides using dielectric media

The use of dielectric media has been widely explored for their potential in terahertz waveguides in last few years. The dielectrics come in a variety of materials and easier to implement in the design and fabrication of terahertz waveguides. These features certainly make them suitable for terahertz applications, however strong absorption of terahertz waves in dielectrics make them unfavorable. Several efforts have been made to minimize losses and improve transmission characteristic of terahertz waves in dielectrics. This includes the use of polymers which not only allow ease of fabrication but also exhibit loss absorption losses at terahertz frequencies. For this purpose, several waveguide configurations have been employed which include hollow-core waveguides, solid-core waveguides, porous-core waveguides etc.

In hollow-core waveguides, THz waves propagate largely along the hollow core and only a small fraction of it propagates in the material which is mainly responsible for absorption losses. In this context, Dupuis *et al.* have experimentally investigated the transmission and loss characteristics of terahertz in a hollow-core dielectric waveguide made of Bragg fibers [19]. Further, Mitrofanov *et al.* reported the technique of dielectric lined hollow cylindrical metallic waveguide to reduce transmission loss and dispersion in hollow THz waveguide [20]. They achieved transmission loss of only 1 dB/m in their scheme. In efforts to reduce losses and optimize transmission characteristics, the hollow-core THz dielectric waveguides have also been investigated in different configurations such as 3-D printed hollow-core THz waveguide [21], hollow-core THz fiber with metamaterial cladding [22], polymer-based hollow-core bandgap fiber [23] etc.

In case of solid-core dielectric waveguides, terahertz wave propagation is based upon total internal reflection process, where the effective refractive index of the core is higher than that of the cladding. In this case, the terahertz waves suffer huge material absorption and result in the weakly confined modes in the waveguide. The efforts have been made to minimize losses using the subwavelength dimension of the waveguide. In this context, Grischkowsky and co-workers have proposed sapphire fibers and plastic ribbon based waveguides and reported a significant reduction in the losses under the optimum waveguide dimensions [24].

In order to reduce losses and improve confinement in solid core waveguide, in 2008, Hassani *et al.* and Atakaramians *et al.* Independently investigated porous-core dielectric waveguides for the transmission of terahertz waves [25, 26]. They introduced subwavelength scale air holes in the core of fibers, which not only reduce dielectric and bending losses but also lower frequency dependent dispersion losses.

1.1.2 Terahertz waveguides using conducting media

The conducting substrates such as metals exhibit non-dissipative behavior at terahertz frequencies, unlike the visible frequencies, however high reflection losses due to the finite conductivity of metal make them unsuitable for terahertz guided wave applications. In last few years, a considerable research interest has been made to reduce losses in metals and investigate guided wave characteristics in various different metallic configurations. In this context, McGowan *et al.* for the first time reported experimental investigations on the efficient coupling of THz radiation and transmission into the sub-millimeter circular metal waveguide using quasi-optical methods [14]. They obtained a waveguide transmission of about 40% of input THz power. In order to improve the coupling efficiency and reduce losses, Gallot *et al.* reported a comprehensive experimental and theoretical study on circular and rectangular metallic waveguides and observed a comparatively low-loss and very low dispersive propagation [27]. In 2001, Mendis *et al.* proposed parallel plate waveguide which was efficient for sub-picosecond pulse propagation with negligible group velocity dispersion [15]. They demonstrated low dispersive TEM mode propagation of THz pulses and discuss their potential in sensing and nonlinear pulse propagation.

Further, Wachter *et al.* proposed metallic slit waveguide for terahertz wave transmission with negligible dispersion and very low attenuation [28]. In 2008, Bingham *et al.* have experimentally investigated terahertz parallel plate photonic waveguide and demonstrated narrowband-pass and narrowband-reject high contrast frequency filtering response in the terahertz domain [29]. Such waveguides could be significant in the development of next-generation terahertz devices such as on-chip networks, interferometers, modulators and waveguide bands etc.

1.1.3 Silicon based terahertz waveguide

Recently, efforts have been made to replace metals with crystalline silicon for terahertz guided wave applications. In silicon, waveguides can be easily fabricated on a bulk scale using the photolithographic technique. Also, dielectric properties of silicon can be adjusted by controlling the dopant concentration, which gives us the flexibility to control propagation and confinement features of the wave. Therefore, silicon-based terahertz waveguides could be the building blocks for the next generation high-speed active terahertz systems. Several terahertz guided wave devices based upon silicon have been discussed both in theory and experiments. In this context, terahertz switch in silicon-based photonic crystal waveguide using self-imaging principle has been recently discussed. The waveguide is designed with triangular lattices, which support multimode propagation [30]. Their theoretical calculation found transmission up to 95.2 % which is important for designing of different kinds of photonic crystal switches. Further, Li *et al.* have reported compact and integrated terahertz switch based on the silicon photonic crystal [31]. In this case, air holes of triangular lattice structures are filled with liquid crystal of varying refractive index, from 1.51 to 2.01. The switching response is achieved via a dynamic shift of the photonic band gap. This switch promises rapid response time and low voltage operation could be significant to other THz applications.

In silicon waveguides, Tsuruda *et al.* have examined extremely low-loss terahertz wave propagation in a silicon based photonic crystal THz waveguide. The propagation loss of less than 0.1 dB/cm and bending loss of 0.2 dB/bend are reported in their study for 0.323-0.331 THz [32]. More recently, silicon-based terahertz plasmonic waveguides have been designed, fabricated and characterized for their capability in transmitting signal at terahertz frequencies [33–35]. We will discuss them in the section of terahertz plasmonic waveguides.

1.2 Terahertz plasmonics waveguides

The field of plasmonics has also emerged as one of the cutting edge areas of science and technology. Plasmonics deal with the excitation and propagation of surface plasmon polaritons at the metal-air or metal-dielectric interface. For the demonstration of terahertz waveguides in experiments and theory, the plasmonic approach has been extensively used in past few years. Before discussing terahertz plasmonic waveguides in detail, it is important to discuss surface plasmon polaritons and their propagation in conducting media.

1.2.1 Surface plasmon polaritons

Surface plasmon polaritons are the electromagnetic excitations at the interface of metal-air or metal-dielectric. When TM mode of an electromagnetic wave is incident on a planar smooth metal surface, then it induces surface charges at the interface. The induced surface charges undergo collective oscillations which result in the radiation of surface electromagnetic waves, also known as surface plasmon waves or surface plasmon polaritons. The amplitude of surface plasmon polaritons decays exponentially away from the interface in both the media. The magnetic field of the SPW is parallel to the surface and perpendicular to its direction of propagation while electric field has components parallel to the direction of propagation and perpendicular to the surface. The propagation of the surface plasmon polaritons and its typical mode profile is shown in Fig. 1.3.

The dispersion relation of the surface plasmon wave on a single metal-dielectric can be obtained by solving Maxwell's equations in both the media and applying appropriate boundary conditions [36]. The dispersion relation of the surface plasma wave on a single metal-dielectric interface is given by

$$k_{sp} = \frac{\omega}{c}\sqrt{\frac{\epsilon_1 \epsilon(\omega)}{\epsilon_1 + \epsilon(\omega)}}, \tag{1.1}$$

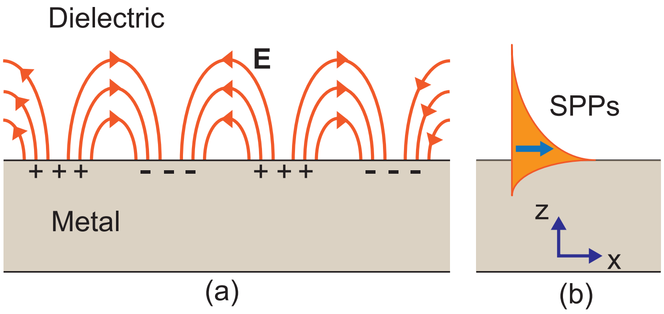

Figure 1.3: (a) Schematic illustration of electromagnetic wave and surface charges at the interface between the metal and the dielectric material, (b) the local electric field component is enhanced near the surface and decay exponentially with distance in a direction normal to the interface.

where, k_{sp} is the wave-vector of surface plasmon polaritons. ϵ_1 is the dielectric permittivity and $\epsilon(\omega)$ is the effective permittivity of metal.

The dispersion relation for surface plasmon wave at the metal-air interface is shown in Fig. 1.4. The dispersion curve follows the light line in the beginning and then it drifted away from the light line and saturates at a frequency is called surface plasmon frequency (ω_{sp}). Surface plasmon frequency corresponds to zero group velocity and therefore it leads to strong confinement of SPW along the waveguide which is significant to the construction of devices such as buffers, storage devices etc.

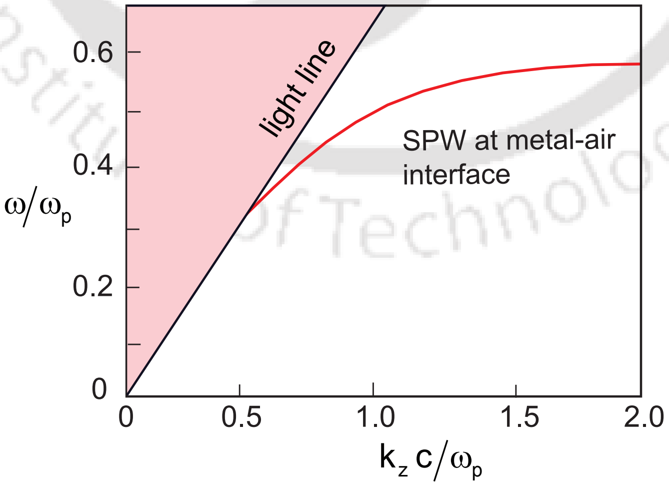

Figure 1.4: Dispersion for a Surface Plasmon Polaritons propagating at the metal-dielectric interface. The black line represents the light line.

It may be noted that for the same frequency, the wavenumber of surface plasmon polaritons is greater than the light line. This feature can be useful to beat the diffraction limit and construct miniaturized devices. The features such as lower wavelength and high electric field of the surface plasmons at the interface are important for several applications such as enhanced Raman spectroscopy, sub-wavelength imaging, improving solar cell efficiently, increased laser ablation, bio-sensors etc.

1.2.2 Terahertz surface plasmons using conducting media

The versatile applications of plasmonics can also be persuaded in the terahertz frequency regime. At terahertz frequencies, metals exhibit high conductivity and in fact behaves like a perfect conductor, therefore it is not possible to excite surface plasmons on metal at THz frequencies. To address it, Pendry and his co-workers in 2004, in their seminal work proposed the technique of periodic patterning of a conductive surface. A schematic of their geometry is shown in Fig. 1.5(a). Solving Maxwell's equations under appropriate boundary conditions, they calculated dispersion relation, which is given by [37].

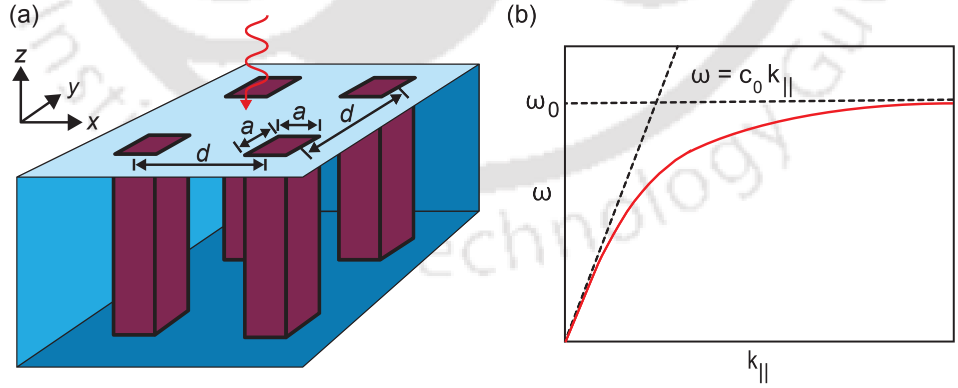

Figure 1.5: (a) Depicts schematic of the two-dimensional array of rectangular apertures (b) Shows dispersion relation of surface plasmon mode supported by the periodic array of rectangular apertures.

$$k_{||}^2 c^2 = \omega^2 + \frac{1}{\omega_{cut-off}^2 - \omega^2} \frac{64 a^4 \omega^4}{\pi^4 d^4}, \tag{1.2}$$

where,

$$\omega_{cut-off} = \frac{\pi c}{a\sqrt{\epsilon_h \mu_h}}, \tag{1.3}$$

In equation (1.2), $k_{||}$ is the wave vector along the metal surface, c is the free space light velocity, d is the distance between each hole, a is the length of these square apertures. ϵ_h and μ_h are the permittivity and permeability of any material that may be filling the holes.

From the dispersion relation shown in Fig. 1.5(b), it may be noted that the patterning of metal surface mimics the dispersion relation of a traditional surface-plasmon wave. The dispersion cut-off frequency depends upon the patterning parameters and therefore dispersion relation can be altered by changing them. This work led to significant advancements in the field of plasmonics at terahertz frequencies. The approach has been greatly used to investigate terahertz plasmonic waveguides and related applications, both theoretically and experimentally.

1.2.3 Developments in terahertz plasmonic waveguides

In terahertz plasmonic waveguides, subwavelength scale periodic structures are patterned in a conducting media, which results in the excitation of the terahertz surface plasmon polaritons. The terahertz SPPs propagate along the periodic structures which provide required skin depth to these waves. Several plasmonic waveguides have been investigated for their potential in different applications such as slow light devices [38], high speed communication [39], filters [40, 41] etc. In 2008, Williams *et al.* for the first time, experimentally reported highly confined surface plasmon polaritons propagation by structuring a dielectric and depositing a thick copper layer over it [42]. Subsequently, Zhu *et al.* reported planar plasmonic terahertz waveguides based upon the 1D array of apertures on thin stainless steel foil and demonstrated passive guided wave components [43]. In an attempt to reduce propagation loss, Kumar *et al.* experimentally examined the ability to guide THz radiation using 1D arrays of periodically spaced rectangular blind holes in stainless steel metal films [44]. The blind hole pattern led to the propagation of THz surface plasmons only on one side of the waveguide, thereby reducing losses. More recently, 3D printing techniques have been used to create plasmonic terahertz waveguides [45]. THz waveguides have also been widely investigated in theory in last decade [46–48]. Wood *et al.* have investigated dispersion properties of surface plasmon polaritons in slanted dimpled surface patterns and examined their field confinement in detail [49]. Rusina *et al.* have developed a fundamental understanding in designing the optimum and efficient metal / dielectric nanowaveguides suitable for the THz nanofocusing [50]. The nano-concentration of THz radiations is reported by considering a parallel plate waveguide that consists of a dielectric slab sand-witched between two thick metal plates.

The efforts have also been made in replacing metals with semiconductors for plasmonic guided wave devices at terahertz frequencies. In this context, Kumar *et al.* have experimentally demonstrated the guiding of terahertz modes in a waveguide comprising of sub-wavelength scale pillars in a highly doped silicon surface [33]. Several other plasmonic waveguides with their constituents including slanted grooves [49], V-grooves [34], inverted pyramids have been examined in recent times. The potential of plasmonic waveguides in actualizing terahertz devices has also been rigorously persuaded. You *et al.* have demonstrated a terahertz plasmonic sensor for sensing applications in a hybrid planar waveguide composed of a sub-wavelength plastic ribbon waveguide and a diffraction metal grating [51]. In 2008, Gan *et al.* reported a THz plasmonic waveguide with a gradual increase in the depth of structures and explored slow-light phenomena [38]. They showed that light of different frequencies can be trapped at different locations of a chip over a wide range of temperatures in the THz spectrum. Nagai *et al.* designed a parallel metal plate waveguide with a periodic array of pillars at its metal plates and examined an achromatic quarter wave plate for terahertz applications [52]. Very recently, Mittendorff *et al.* proposed a graphene-based waveguide for THz modulation [53]. In their work, the graphene sheets are perforated in a dielectric waveguide to tune the absorption of terahertz and hence modulates it. THz plasmonic waveguides have also been examined for their ability to filter a frequency band. In this context, Mendis *et al.* proposed a tunable filter based on the parallel plate waveguides, which allows low-pass, high-pass, band-pass, and band-stop filtering characteristics [54].

1.2.4 Design, fabrication and characterization of terahertz plasmonic waveguides

The optimum design of terahertz plasmonic waveguide is extremely important for the low loss and highly confined terahertz mode propagation and hence their significance in a variety of applications. For the design purpose, commercially available electromagnetic numerical simulation packages can be used. For our research work, we used commercially available CST Microwave Studio simulation software. This is an electromagnetic 3D numerical simulation tool with the options of both tetrahedral and hexahedral shaped meshing. The meshing size is chosen to be sufficiently small for attaining the high accuracy of results in the case of plasmonic waveguides. In simulations, we apply perfectly matched layer boundary condition in order to avoid reflections that can interfere with actual surface fields. The waveguides are excited using a broadband terahertz pulse at the one end of waveguide via a waveguide port. A separate waveguide port is used to detect terahertz surface plasmon polaritons at the other end. Owing to the high conductivity of metals at terahertz frequencies, the waveguides material is assumed to be a perfectly electrical conductor in simulations. In electric and magnetic field boundary conditions, we use electric field normal to the surface and magnetic field along the surface however perpendicular to the direction of propagation. The time domain signal is collected at the detection waveguide port and Fourier transformed to obtain frequency domain spectrum.

In order to examine, dispersion properties of the modes supported by the periodically patterned waveguides, we have used Finite Element Eigenmode solver of the CST numerical simulation package. We numerically model a structure as a unit cell under the periodic boundary condition in the direction of propagation. The phase is varied from 0 to 180 degrees in order to extract dispersion properties of the terahertz modes supported by the waveguide.

One can fabricate proposed terahertz plasmonic waveguide using thin metal sheets or highly doped silicon substrates. For thin metal sheet, laser micromachining technique may be used to make apertures in a periodic fashion and then, another planar metal film can be glued on its back using the conducting epoxy [44]. In silicon, one may use heavily doped crystalline silicon of carrier concentration $n \geq 10^{19}\ cm^{-3}$, which behaves like conductor with high conductivity at terahertz frequencies. The surface of the silicon can be coated with silicon dioxide ($\mathrm{SiO_2}$) layer of 1-2 μm thickness, grown via the technique of low-pressure chemical vapor deposition (LPCVD). Then, the surface can be patterned with periodic structures via photolithography. In next step, silicon can be etched via deep reactive ion etching (DRIE) to make rectangular grooves or pillars. For the fabrication of V-grooves, appropriately designed silicon can be etched in a mixture of potassium hydroxide, water, and isopropanol in the ratio of 60:30:10. The fabrication of plasmonic waveguides in silicon has been recently reported [33, 34]. The characterization of the proposed waveguides can be accomplished using the modified technique of terahertz time-domain spectroscopy [33].

Terahertz time domain spectroscopy (THz-TDS)

Terahertz time-domain spectroscopy is used to measure transmission properties of samples in the transmission modes and waveguide configuration. A schematic of the THz time-domain spectroscopic setup for characterizing planar terahertz waveguides is shown in Fig. 1.6(a).

In this setup, a beam from a femtosecond (fs) laser system is divided into two beams using a beam-splitter: the probe and pump beams. The pump beam is used to generate the THz pulses via optical rectification in ZnTe crystal, while probe beam is used to sample and obtain the pulse profile. For terahertz plasmonic waveguide measurements, the coupling of free space terahertz waveforms to the waveguide geometry is very important. The incident terahertz waves can be coupled via a shallow wide rectangular or circular groove. The impinging terahertz beam is linearly polarized in the direction perpendicular to the structures (i.e., with the magnetic field parallel to the grooves). The detection of THz field is performed via electro-optic (EO) sampling in which probe pulse is modulated with the THz surface plasmon polariton field. The mechanical delay stage provides the required time delay to the probe pulses for the detection of entire terahertz waveform. Since the spectroscopic measurements through this technique are carried out by recording the THz waveform in the time domain, this technique is called THz time-domain spectroscopy (THz-TDS). The time domain spectra can be Fourier transformed to obtain frequency domain spectra. Fig. 1.6(b) and (c) depicts time-domain terahertz pulse and its corresponding frequency domain spectra.

In the frequency domain spectra, the spectral resolution of THz-TDS, usually defined as, $\delta\omega$, is determined by the temporal scanning range, say T as the

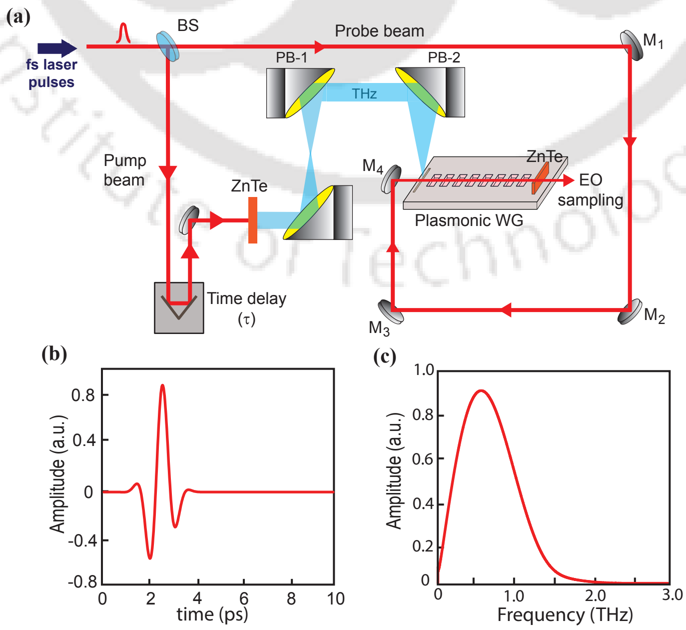

Figure 1.6: (a) Schematic of the terahertz time domain spectroscopy setup, (b) Time-domain waveform of single cycle THz pulse, (c) Frequency domain spectra of time domain THz pulse.

bandwidth of THz-TDS is given by,

$$\delta\omega = \frac{2\pi}{T}, \tag{1.4}$$

The bandwidth ($\triangle\Omega$) of terahertz time domain spectroscopy is given by,

$$\triangle\Omega = \frac{2\pi}{\delta T}, \tag{1.5}$$

where, δT is the temporal sampling interval. The THz-TDS technique provides both phase and amplitude information and hence becomes significant in extracting both the absorption and dispersion properties.

1.3 Terahertz metamaterials

1.3.1 Metamaterials

In last two decades, the field of metamaterials has emerged as one of the frontiers in modern trends of science and technology. Metamaterials are the engineered materials which have unique properties that are not usually found in nature. They are made up of metal and semiconductor, and exhibit properties depending upon the design of structures. In metamaterials, the constituents such as the split ring resonators (SRRs) [55–58], metal wires [59–61], fishnet structures [62–65] etc are periodically arranged on a planar substrate. The SRRs are the most popular and widely examined metamaterial structure. The research in metamaterial started in 1999 when Pendry *et al.* in their seminal work discovered strong local magnetic field in microstructures, which were made up of non-magnetic conducting sheets [66]. In 2001, Shelby *et al.* for the first time experimentally verified the negative index of refraction in the microwave region of electromagnetic spectrum [67]. Although this discovery was introduced in the microwave region, soon it led to the exploration of metamaterials in other parts of the electromagnetic spectrum.

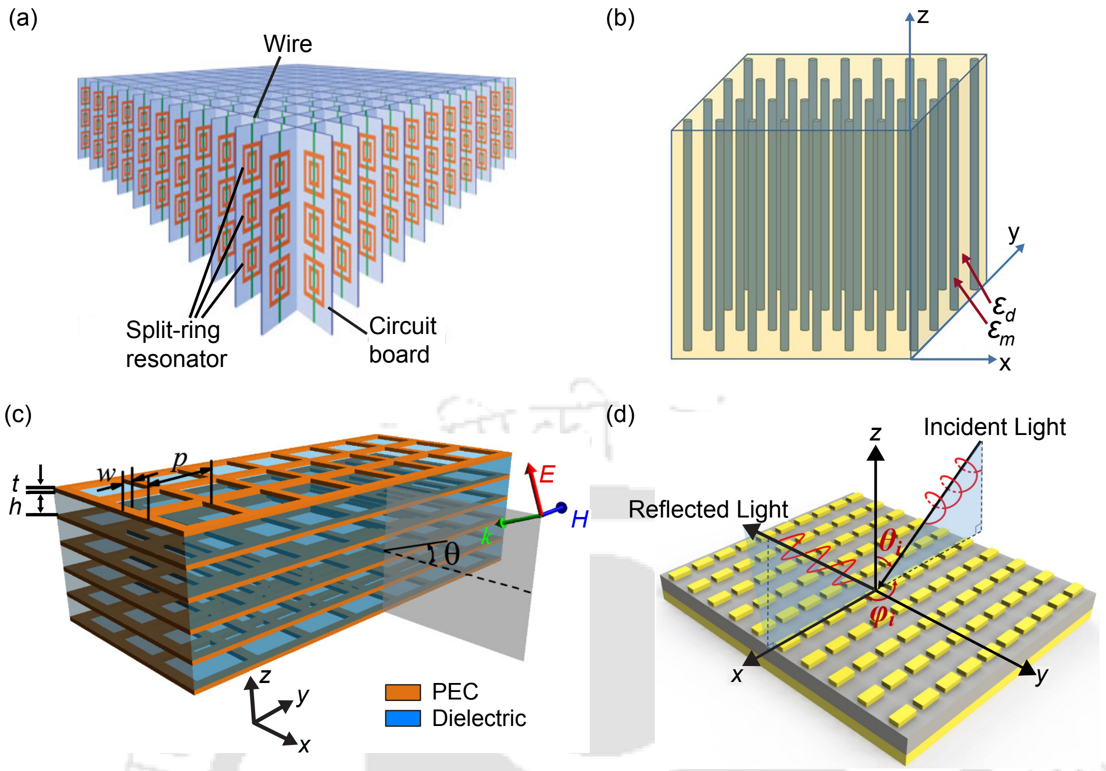

Figure 1.7: Some of the metamaterial geometries. (a) Depicts metamaterial geometry comprised of a two-dimensional array of SRRs having negative refractive index, (b) shows metal wires structured metamaterials for filtering application, (c) presents stacked fishnet structure based metamaterials for subwavelength imaging, (d) depicts plasmonic metamaterials based quarter and half wave plates.

Several metamaterial configurations and their applications in the construction of devices have been investigated since the inception of this field. Fig. 1.7 depicts few of the metamaterials structures that have been investigated in various frequency regimes of the electromagnetic spectrum. In Fig. 1.7(a), we show a two-dimensional isotropic left-handed metamaterial geometry that was first experimentally investigated by Shelby *et al.* in microwave regime [67]. Fig. 1.7(b) depicts a two-dimensional cubic structured metamaterial geometry consisting of thin metal wires of wire diameter 30 μm. The metal wire plasmonic metamaterials structures was investigated to filter high band frequencies [68]. In Fig. 1.7(c), stacked fishnet metamaterial geometry is shown which was used by Wei *et al.* to demonstrate broadband negative refraction and subwavelength imaging in long wavelength regime [64]. Fig. 1.7(d) shows half-wave and quarter-wave plates based on plasmonic metamaterial structures which enable high polarization conversion efficiency and efficient reflection for visible to near-infrared wavelength range [69]. Several other metamaterial geometries having constituents such as complementary split ring resonators (CSRRs), toroidal solenoid, and chiral structures etc. have also been investigated in past few years [70–74] while aiming applications in diversified areas.

1.3.2 Metamaterial structures for terahertz applications

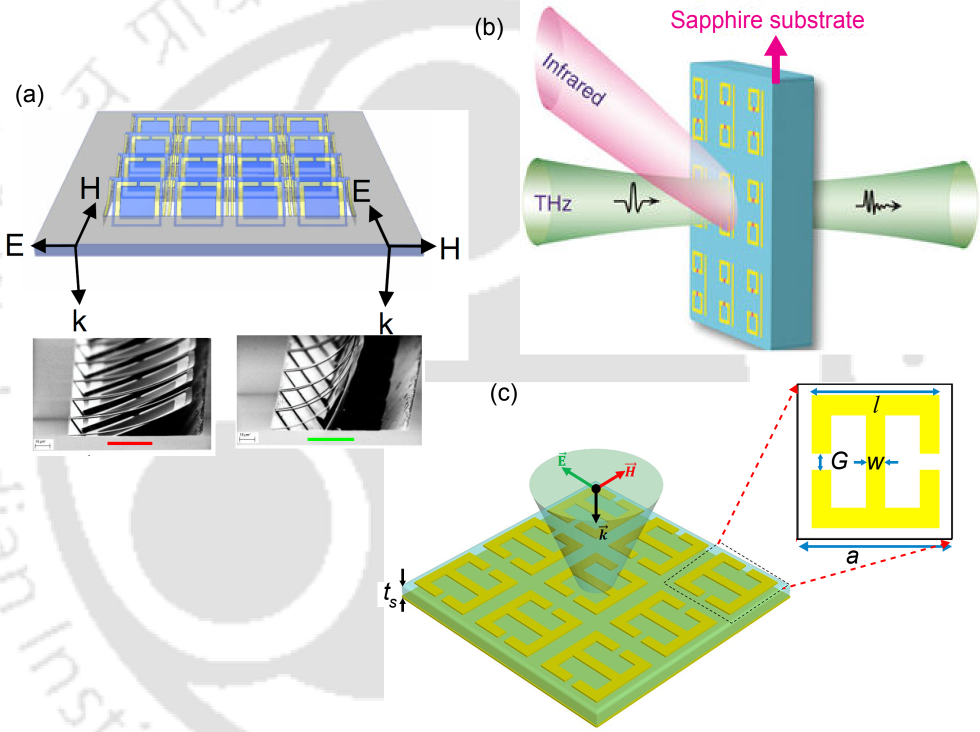

Figure 1.8: Some of the terahertz metamaterial geometries and their application in different areas. (a) Depicts reconfigurable terahertz metamaterial geometry comprising of SRRs rotated like a cantilever legs bend along with the scanning electron micrographs (SEM) of fabricated samples, (b) shows planar terahertz metamaterials structure based on common wire and SRRs to exhibit electromagnetic induced transparency with slow-light effect, and (c) presents terahertz metamaterial absorber based on three-layered structure comprised of SRR, dielectric, and metallic film.

The metamaterials can be designed with varying shapes and sizes of its constituents depending upon their applications in different domains of the electromagnetic spectrum. At terahertz frequencies, the metamaterial structures are relatively easier to fabricate because of the bigger sizes of its constituents. THz metamaterials could be significant in a variety of applications including absorbers, sensors, construction of next-generation photonic devices etc. [75–79]. In Fig. 1.8, some of the terahertz metamaterial geometries important to various device applications have been shown. Fig. 1.8(a) depicts a reconfigurable terahertz metamaterial geometry comprising of an array of bent SRRs along with the SEM pictures of fabricated samples. The geometry has the ability to provide tunable electromagnetic response which could be significant in designing reconfigurable cloaks and absorbers [80]. In Fig. 1.8(b), terahertz metamaterial configuration using photoconductive silicon is shown. Gu *et al.* used this configuration to investigate electromagnetically induced transparency and slow light effect in terahertz frequencies [81]. In Fig. 1.8(c), a three-layered metamaterial structure comprising of SRRs, dielectric, and a metallic film is shown that was used to demonstrate switchable and tunable terahertz absorber [76]. In other important contributions in terahertz metamaterials, Chowdhury *et al.* reported ultrafast optical control of near-field coupling between bright and dark mode resonances from two orthogonally twisted coupled resonators [82]. The findings could be important to design and construct ultrafast terahertz active devices. Singh *et al.* studied ultrafast resonance tuning under near-infrared photo-excitation in planar high-temperature superconducting terahertz metamaterials [83].

1.3.3 Thin film sensing using THz metamaterials

There has been considerable interest in investigating sensor applications using THz metamaterials. In the context of thin film sensing, O'Hara *et al.* reported the first article describing the sensing capability of terahertz metamaterials based on double SRRs and the limitations [84]. They varied the thickness of a dielectric over-layer of $\epsilon_r \sim 2.7$ on planar double SRRs to examine the frequency shift value using THz time-domain spectroscopy. Next, Tao *et al.* proposed biosensing application of THz metamaterials comprising gold SRRs in an ultra-thin substrate of 400 nm thick silicon nitride [85]. They investigated the increased sensitivity of SRR based metamaterial for the detection of doped and undoped protein thin films (silk fibroin) of different thicknesses. Thereafter, Withayachumnankul *et al.* examined the possibility to enhance thin film sensing capability of SRR based planar THz metamaterials using near-field technique of sub-diffraction THz source [86]. Near-field THz source reduces the number of resonators, thereby increasing Q factor of resonances. The Q-factor can be defined as $f_0/\triangle f$, where f_0 is the resonance frequency and $\triangle f$ is the full width at half maximum of the resonance mode. The high value of Q-factor is desirable for better sensing characteristics. More recently, Gupta *et al.* investigated thin film sensing with toroidal metamaterials [87]. Toroidal metamaterials consist of a double split gap square shaped metallic strips and results in high-Q resonances, which could have the way for more innovative sensing techniques.

1.3.4 Design, fabrication and characterization of terahertz metamaterials

Similar to plasmonic structures, the design of metamaterial structures and their response to the incident electromagnetic radiation can be accomplished using the electromagnetic simulation software package. It is important to optimize the design parameters before proceeding to the complex and expensive fabrication process. The metamaterial structures in the transmission configuration require unit cell boundary condition while considering one unit of the metamaterial constituent i.e. a meta-molecule. This results in a planar metamaterial geometry of infinite number unit cell structures. In this case also, two waveguide ports are used, one for the excitation signal and the other to detect transmitted THz radiation in the frequency domain.

The designed samples can be fabricated using the conventional photolithographic techniques. In photolithography, first, photo-resist is coated onto the silicon substrate. Thereafter, metamaterial structures are patterned using the properly designed mask and shinning the substrate with an ultra-violet light followed by a development process. Then, a thin layer of metal is evaporated using the e-beam or thermal evaporator. Finally, the metamaterials structures are obtained after the lift-off process in which residual photo-resist is removed.

The fabricated samples can be characterized using the THz-TDS technique discussed above through Fig. 1.6. In order to measure the transmission response, the metamaterial samples may be placed between the parabolic mirrors of the experimental setup. Another ZnTe crystal followed by electro-optic (EO) sampling may be used to measure the transmission response [88].

1.4 Theoretical modeling of plasmonic and metamaterial structures

The modeling of plasmonic and metamaterial structures is important to understand the terahertz transmission response through these structures. One can use semi-analytical transmission line theory to model plasmonics and metamaterial structures separately. Theoretical calculations based on transmission line model also help us to confirm the numerical findings, hence allow more physical insight inside the system.

1.4.1 Modeling of terahertz plasmonic structures

The transmission line approach in the context of plasmonic and metamaterial structures has been discussed and employed in the literature also [89, 90]. In our case, the transmission line model is governed by the lumped circuit elements having components as inductance (L), capacitance (C), and mutual inductance (M). The coupling of THz radiation to the plasmonic and metamaterial structures leads to the excitation of oscillating current inside the grooves, therefore, giving rise to inductance L. Because of the alternating currents, charge accumulation also takes place in certain regions of the groove which gives rise to effective capacitance C. In TL theory, the resonant behavior of plasmonic and metamaterial structures depend on the inductance (L) and capacitance (C) value only. The broadness of a resonance in numerical simulation can be attributed to the scattering, dispersion, and diffraction losses that a wave experiences when it propagates along the corrugated pattern.

We have used transmission line LC circuit model to understand and validate numerical observations in case of plasmonic waveguides and their application as sensors. We consider that a unit cell is comprised of two corrugations which are coupled through the mutual inductance M. The intrinsic impedance (Z_0) of the circuit can be calculated based upon the dimensions of the plasmonic geometry [89]. The circuit impedance (Z_S) depends on the circuit representing the corrugated structure. Finally, the transmission amplitude $t(\omega)$ corresponding to the intrinsic and circuit impedances can be calculated while solving the conventional form of transmission equation,

$$t(\omega) = \frac{2Z_S}{Z_0 + Z_S} \tag{1.6}$$

1.4.2 Modeling of terahertz metamaterial structures

In case of metamaterial structures, one can again use transmission line – RLC circuit model to explain the transmission properties through them. The circuit model under transmission line theory depends on the metamaterial design, specifically on single split ring resonator. The SRR loop corresponds to the inductive part, the internal reactance of SRR corresponds to resistance and the split gap of SRR is represented by capacitance in the model. The coupling between the resonances is represented by mutual inductance M. Similar to plasmonic structures, the substrate and circuit impedances can be used to calculate normalized transmission amplitude.

1.5 Plan of thesis

In thesis work, we have investigated terahertz waveguides and sensors using plasmonic and metamaterials structures. Using plasmonic structures, we have explored the possibility to guide highly confined terahertz modes along the corrugated pattern, whose properties can be altered with the parameters of the plasmonic structures. We have also investigated the potential of terahertz plasmonic waveguides as sensors and comprehensively discuss various sensing parameters that decide the sensing capability of a sensor. In metamaterial structures, the focus has been to investigate the role of fundamental and higher-order resonances supported by planar terahertz metamaterials in thin film terahertz sensor. The work proposed in this thesis has been divided into six chapters. A chapter wise summary of the thesis is as follows:

Chapter 1 presents an overview of the field of terahertz and briefly discusses the generation, detection, and applications of terahertz frequencies. We have also discussed the propagation of terahertz waveguide in conducting media, and dielectric medium including silicon. We have also illustrated the design, fabrication, and characterization of terahertz plasmonic and metamaterial structures in this chapter. Further, we have provided a brief overview of recent developments in the field of terahertz using plasmonic and metamaterial structures. The modeling aspect of such structures has also been discussed briefly in this chapter.

Chapter 2 investigates terahertz plasmonic waveguide using periodically arranged tilted pillars and control over the propagation properties of guided modes through the bending of pillars. A metal surface approximated as perfectly electrical conductor at terahertz frequencies is periodically corrugated with sub-wavelength scale tilted pillars thereby forming a plasmonic waveguide. The plasmonic waveguide supports highly confined guided terahertz modes at specific frequencies depending upon the pillar dimensions. We confirm the propagation of terahertz modes through a semi-analytical model that we employ specifically for our geometry. We observed that the propagation properties of the terahertz modes can be controlled by changing the bending of pillars. We have examined the propagation of the guided modes for different angles and directions of the pillars. Further, we examined terahertz plasmonic waveguides comprising pillars with increasing height, and investigate their ability in confining terahertz waves at a certain position where the natural frequency of a pillar matches to the incident frequency.

Chapter 3 discusses terahertz surface plasmon propagation properties in a waveguide comprising of sub-wavelength scale internally corrugated V-shape structures. The internal corrugations could be important to cause additional changes in the properties of modes of a terahertz waveguide. In the waveguide geometry, the structures are assumed to be periodically arranged in a thin sheet of metal and ensure plasmonic response of the waveguide. We comprehensively examine the effect of internal corrugations on the plasmonic properties of the guided modes supported by the waveguide. The mode properties are found to vary with the internal corrugations of the structures. We observe that multimode propagation can be switched into a single mode as the steps of internal corrugations increase. The findings are supported by a theoretical transmission line RLC circuit model. We also analyze the dispersion properties of the fundamental modes under the different steps of corrugations and calculate group velocity in order to understand the slow light behavior of the modes.

Chapter 4 investigates sensing capabilities of a planar plasmonic terahertz waveguide. The waveguide is comprised of a one-dimensional array of periodically arranged subwavelength scale corrugations in the form of rectangular dimples in order to ensure the plasmonic response. The terahertz waveguide transmission is observed for polyimide (as thin film) substance filling the dimples. The refractive index of the polyimide film is varied to examine various sensing parameters such as frequency shift, sensitivity, and Figure of Merit (FoM) of the fundamental plasmonic resonance supported by the waveguide. We employ a semi-analytical transmission line LC circuit model to elucidate our numerical observations. In efforts to improve sensing characteristics, we also examine sensing capabilities of a plasmonic waveguide having V-shaped corrugations and compare results with that of rectangular dimples. The proposed study could be significant in developing new terahertz sensors with improved sensitivity utilizing the plasmonic waveguides.

Chapter 5 examines thin film sensing capabilities of a terahertz metamaterial, which is comprised of an array of single split gap ring resonators (SRRs). The top surface of the proposed metamaterial structures is covered with a thin layer of analyte in order to examine various sensing parameters. The sensitivity and corresponding figure of merit (FoM) of the odd and even resonant modes are analyzed with respect to (w.r.t.) the different thicknesses of the coated analyte film. The sensing parameters of different resonance modes are elaborated and explained with appropriate physical explanations. We have also employed a semi-analytical transmission line model in order to validate numerical observations.

In **Chapter 6**, we summarize our work and future directions of terahertz research using plasmonic and metamaterial structures in the context of our study.

1.6 Publications

(a) Peer-reviewed Journal Publications

1. **Maidul Islam** and Gagan Kumar, "*Terahertz surface plasmons propagation through periodically tilted pillars and control on directional properties*", **Journal of Physics D: Applied Physics**, 49, 435104 (2016).

   (doi:10.1088/0022-3727/49/43/435104)

2. **Maidul Islam**, Dibakar Roy Chowdhury, Amir Ahmad, and Gagan Kumar, "*Terahertz guided mode properties in an internally corrugated plasmonic waveguide*", **AIP: Journal of Applied Physics**, 122, 053105 (2017).

   (doi:10.1063/1.4997451)

3. **Maidul Islam**, Dibakar Roy Chowdhury, Amir Ahmad, and Gagan Kumar, "*Terahertz plasmonic waveguide based thin film sensor*", has been published in **Journal of Lightwave Technology**, 35, 2763326 (2017).

   (doi:10.1109/JLT.2017.2763326)

4. **Maidul Islam**, S Jagan Mohan Rao, Gagan Kumar, B. P. Pal, and Dibakar Roy Chowdhury, "*Role of resonance modes on terahertz metamaterials based thin film sensors*", **Scientific Reports**, 7, 7355 (2017).

   (doi:10.1038/s41598-017-07720-9)

5. Dhiman Bhattacharya, Prasant K Sarswat, **Maidul Islam**, Gagan Kumar, and Michael L Free, "*Geometrical modifications and tuning of optical and surface plasmon resonance behavior of Au and Ag coated* TIO_2 *nanotubular arrays*", **RSC Advances**, 5, 70361-70370, (2015).

   (doi: 10.1039/C5RA12191D)

6. Koijam Monika Devi, **Maidul Islam**, Dibakar Roy Chowdhury, Amarendra K. Sarma, and Gagan Kumar, "*Plasmon induced transparency in graphene based terahertz metamaterial*", **Europhysics Letters**, 120, 27005, (2017).

   (doi: 10.1209/0295-5075/120/27005)

7. Nipon Dekha, **Maidul Islam**, Prashant K. Sarswat, Gagan Kumar, "*Enhancing solar cell efficiency with plasmonic behavior of double metal nanoparticle system*", **Vacuum**, 152, 285-290 (2018).

   (doi: 10.1016/j.vacuum.2018.03.026)

(b) Conference Publications

1. **Maidul Islam** and Gagan Kumar, "*Terahertz surface plasmon polaritons propagation in slanted pillar geometries*", CCP 2015 conference proceedings in Journal of Physics: Conference Series, 759, 012053(2016).

(doi:10.1088/1742-6596/759/1/012053)

2. **Maidul Islam**, Dibakar Roy Chowdhury and Gagan Kumar, "*Terahertz guided mode propagation in a planar plasmonic waveguide and slow light properties*", PHOTONICS 2016 conference proceeding, OSA, P1A-21(2016). **(doi.org/10.1364/PHOTONICS.2016.P1A.2)**

3. **Maidul Islam**, Dibakar Roy Chowdhury and Gagan Kumar, "*Terahertz plasmonic waveguide based thin film sensor*", is accepted in WRAP 2017, conducted by IEEE photonics society at Mahindra École Centrale, Hyderabad.

4. Koijam Monika Devi, **Maidul Islam**, Dibakar Roy Chowdhury, Amarendra K. Sarma, and Gagan Kumar, "*Exploring plasmon induced transparency in graphene based terahertz metamaterials*", is accepted in WRAP 2017, conducted by IEEE photonics society at Mahindra École Centrale, Hyderabad.

(c) Conferences/Workshops attended

1. Presented a poster entitled with "*Geometrical modifications and tuning of optical and surface plasmon resonance behaviour of Au and Ag coated* TiO_2 *nanotube arrays*" in TEQIP organized by IIT Guwahati on 31st October, 2015 at IIT Guwahati

2. Presented a poster entitled with "*Terahertz surface plasmon polaritons propagation in slanted pillar geometries*" in CCP 2015 organized by IIT Guwahati, 2-5 December, 2015 at IIT Guwahati.

3. Presented a poster entitled with "*Terahertz guided mode propagation in a planar plasmonic waveguide and slow light properties*" in Photonics 2016 organized by OSA and IIT Kanpur, 4-8 December, at IIT Kanpur.

***

Chapter 2

Tilted plasmonic structures based terahertz waveguide

Contents

Recently, a significant emphasis has been given towards the development of ultra-high speed communication and information systems [91–93]. In this context, THz waves have been widely examined owing to their ability in transferring signal at much higher speeds than the available communication systems [59, 94, 95]. In order to actualize terahertz devices, one needs to develop efficient waveguides that can exhibit low loss and high directional confinement for the propagating modes [33, 34, 96]. In last more than one decade, substantial efforts have been put forward in developing terahertz waveguides. In this direction, several waveguide geometries capable of guiding THz modes have been devised both experimentally and theoretically [35, 44–46, 97–101]. For terahertz propagation on a planar surface, plasmonic approach has been widely employed, which have been discussed in Section 1.2.3 in Chapter 1. Although, these studies immensely contributed to the field of THz wave communication, but the active and passive components in this frequency regime are still lacking. One of the challenge has been to selectively guide a terahertz mode in a particular direction more efficiently than any other direction. The guiding of terahertz wave in a particular direction under the low divergence can lead to a variety of applications such as remote sensing [102], substance identification [5] and high speed transmission of information [103].

In this chapter, we have explored the directional propagation of THz modes and their control through the tilting of pillars. The tilted structures have been shown to transfer terahertz signal more effectively in a particular direction than the other. In Section 2.1, dispersion relations of the corrugated patterns have been numerically examined, which indicate the plasmonic response of the proposed geometry. Time domain and frequency domain waveguide transmissions of the proposed plasmonic waveguide are analyzed in Section 2.2. A semi-analytical transmission line model is employed to independently confirm the numerically simulated results. The effective propagation of terahertz modes in a particular direction has been discussed via the control on the tilting of the pillars. Finally, the confinement of terahertz modes has been examined at a certain position of the waveguide comprising of pillars of increasing height. In Section 2.3, the results are summarized.

2.1 Waveguide dispersion properties

First, dispersion properties of the terahertz modes supported by the proposed waveguide geometry comprising one dimensional array of tilted pillars have been numerically investigated. The schematic of the designed planar plasmonic THz waveguide is shown in Fig. 2.1(a). The parameters l, h and w shown in the schematic represent length, height and width of the pillars. The substrate thick-

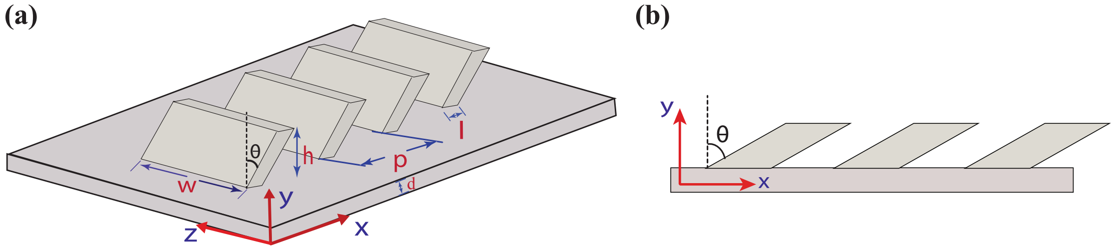

Figure 2.1: Schematic of the planar THz waveguide. (a) A 3-dimensional view of the waveguide comprising of one dimensional array of tilted pillars. The parameters l, w, h and p stand for length, width, height and periodicity of the pillars respectively. Parameter d is the thickness of the substrate. (b) depicts the side view of the waveguide comprising pillars tilted at an angle θ w.r.t. the normal.

ness is represented by d. The pillars are tilted through an angle θ and p is the periodicity of the pillars. In this study, angle θ is varied and corresponding propagation properties of the guided terahertz modes are examined while keeping other parameters constant. The constant parameters of the waveguide are: length (l) = 100 μm, width (w) = 500 μm, height (h) = 100 μm, periodicity (p) = 400 μm and thickness (d) = 100 μm. Fig. 2.1(b) depicts the side view of the proposed waveguide.

The dispersion relations of the fundamental terahertz modes supported by the proposed plasmonic waveguide are obtained using a finite element eigen mode solver. In the simulations, periodic boundary conditions are considered along the propagation direction and absorbing layers condition in the transverse direction. The waveguide substrate is approximated as a perfect electrical conductor (PEC) owing to the high conductivity of metals at terahertz frequencies. Further, tetrahedral shaped grids of size $\lambda/10$ is assumed in the simulations which indicates the subwavelength regime. The results of the dispersion relations for two different values of θ are shown in Fig. 2.2. The red trace represents dispersion relation for the pillars tilted at angle $\theta = 10°$, while blue trace corresponds to $\theta = 60°$. One may note that, for a particular pillar configuration, initially frequency monotonically increases with wavenumber and then saturates. For the case of pillars tilted at 10°, one can get a saturation in the curve at 0.33 THz. This value ideally corresponds to the zero group velocity for which the saturation frequency corresponds to the cut-off frequency. With the increase in the bending of the pillars, the dispersion curve shifted away from the light line and saturates to a lower value of frequency. For $\theta = 60°$, the cut-off frequency turns out to be 0.28 THz. This is because of the increase in the effective height of pillars when they are tilted at a larger angle.

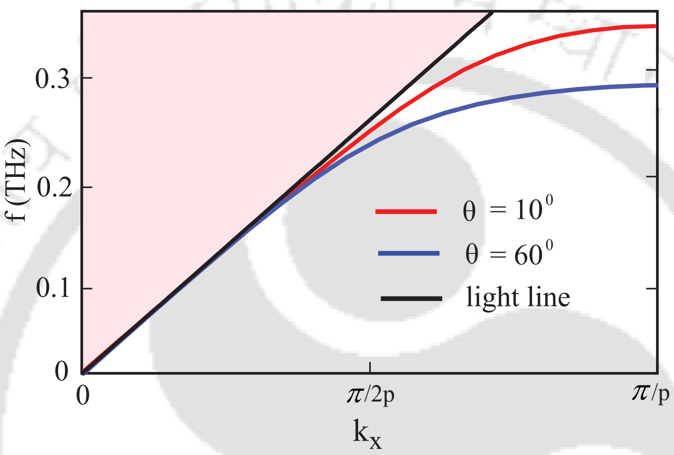

Figure 2.2: Numerically calculated dispersion properties of the fundamental terahertz surface mode. The solid black line represents the light line for the plane wave propagating in the free space above the waveguide. The red and blue curves correspond to the dispersion relations over the first Brillouin zones for the pillars tilted at angles 10° and 60° respectively. The other parameters are: $l = 100\ \mu m$, $w = 500\ \mu m$, $h = 100\ \mu m$, and $p = 400\ \mu m$.

2.2 Terahertz waveguide transmission: Simulation and analysis

One can excite terahertz waveguide with a discrete source of single cycle terahertz waveform from the one end of the waveguide. The terahertz signal is made to propagate along the corrugated pattern and terahertz time domain signal carrying the response is detected at the other end of the waveguide. The terahertz time domain signal is finally converted into the frequency domain spectra using Fast Fourier Transform (FFT) approach. For the simulations, finite element time domain solver has been used in the CST Microwave simulation software.

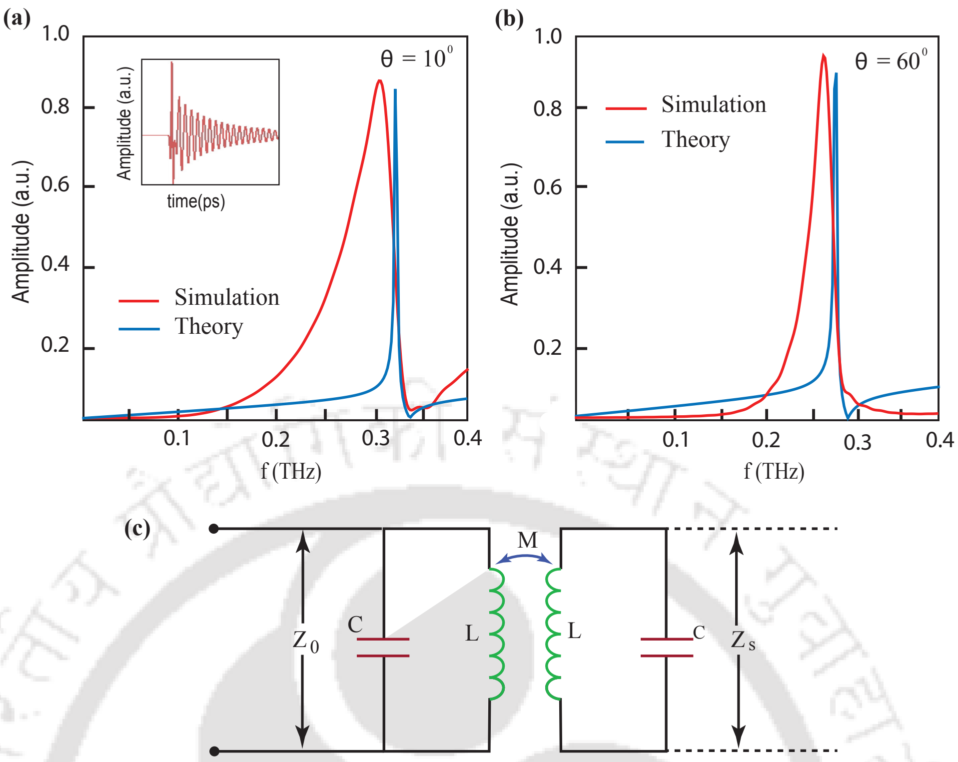

Figure 2.3: (a) and (b) represent the terahertz amplitude transmission from the simulation and theory for two waveguides with pillars tilted at 10° and 60° respectively. The red traces correspond to the numerically simulated results, while the blue traces represent waveguide transmission from an equivalent transmission line-LC circuit model. The other parameters are: length, $l = 400\ \mu m$, width, $w = 500\ \mu m$, height, $h = 100\ \mu m$ and periodicity, $p = 400\ \mu m$. The inset in (a) shows the numerically calculated time-domain signal corresponding to an angle, $\theta = 10°$. (c) Schematic of the transmission line-LC circuit model. L, C and M represent inductance, capacitance and mutual inductance of the circuit. Z_0 and Z_S correspond to the intrinsic impedance and circuit impedance respectively.

First, a 3 cm long planar waveguide with pillars tilted at 10° is examined. The result in the form of frequency domain spectra are shown in Fig. 2.3(a) through red traces. The inset shows the corresponding time domain signal. It is apparent that pillar pattern exhibit resonant behavior with anti-resonant frequency at 0.33 THz. One may note that the anti-resonance frequency matches with the saturation frequency of the dispersion relation for the same pillar parameters and bending angle. Similarly, in Fig. 2.3(b), the results are shown for plasmonic waveguide with pillars tilted at angle 60°. Again, the anti-resonant frequency is compared with the saturation frequency shown in Fig. 2 and they are found in good agreement. The anti-resonant frequency get red-shifted when the bending of the pillars is increased. In order to elucidate the resonant behavior of the plasmonic waveguide and confirm the anti-resonant frequencies of the modes, a semi-analytical transmission line model is employed specific to the waveguide geometry. The results of the amplitude transmission from the model are shown through blue traces. It is noticed that they also predict a resonant behavior and confirm the numerically simulated results for certain values of conductance, inductance and mutual inductance of the constituent pillars. The details of the analytical transmission line model are as follows:

In the semi-analytical model, metal is assumed to have very high carrier density with constituent pillars behaving like an LC circuit under the transmission line approximation. It is considered that a unit cell is comprised of two tilted pillars which are mutually coupled through the mutual inductance, M. The circuit model of a unit cell under the transmission line theory is shown in Fig. 2.3(c). Two pillars of the unit cell are represented by two LC circuits and mutual inductance M is responsible for the coupling of fields between the pillars during terahertz waveguide transmission. One can calculate the intrinsic impedance (Z_0) of this circuit [89], which is given by

$$Z_0 = \frac{120\pi}{\sqrt{\epsilon_i}[\frac{w}{d} + 1.393 + 0.667\ln(\frac{w}{d} + 1.444)]}, \tag{2.1}$$

where, ϵ_i is the effective dielectric constant of metal; w is the width of a pillar and d is the depth of substrate. Now, the impedance of this circuit model (Z_S) can be written as,

$$Z_S = \frac{\frac{L}{C} + \omega^2 M^2}{j[(\omega L - \frac{1}{\omega C}) - \omega M]}, \tag{2.2}$$

where, ω, L, C, and M represent angular frequency, inductance, capacitance, and mutual inductance respectively.

The normalized transmission amplitude, $t(\omega)$ of this transmission line-LC circuit model is given by

$$t(\omega) = \frac{2Z_S}{Z_0 + Z_S}, \tag{2.3}$$

Eq. (2.3) is used to calculate the waveguide transmission and predict anti-resonant frequencies of the resonant modes resulting from the tilted pillars of the plasmonic waveguide. As discussed above, the model enables to predict the anti-resonant frequencies corresponding to the pillars tilted at angles 10° and 60° for certain specific values of inductance, capacitance and mutual inductance which are given through Table 2.1.

Parameter	For tilt angle $\theta = 10^\circ$	For tilt angle $\theta = 60^\circ$
Inductance, L (fH)	13.4	13.4
Capacitance, C (pC)	3.43	4.8
Mutual Inductance, M (fH)	30.1	30.1

Table 2.1: Mutual inductance (M in fH) for different tilt angles used in TL-LC circuit model

Next, the terahertz waveguide transmission of the propagating terahertz modes is examined in the backward and forward directions of the pillar patterned waveguide. A schematic of this waveguide configuration is shown in Fig. 2.4(a). The terahertz source is placed at the center of the waveguide i.e. at $x = x_0$. Since the pillars are designed in both the directions, the incident terahertz will lead to plasmonic mode propagating in both the directions. The position $x = x_1$ corresponds to the position of detector in the forward direction i.e. terahertz propagating in the direction of bending of pillars, while the position $x = x_2$ represents the backward position i.e. pillar's bending opposing the direction of propagation. In the simulations, a 4 cm long waveguide is considered to examine THz waveguide transmission at a distance of 2 cm from the center in both the directions. The pillars of the waveguide are tilted in one direction. The frequency domain spectra indicates a difference in transmission amplitudes calculated at both the ends. The results are shown in Fig. 2.4(b), (c), and (d) for the pillars tilted at 10°, 40° and 60° with respect to normal respectively. The blue and red traces represent signal in the forward and backward directions respectively. For angle $\theta = 10^\circ$, an output amplitude of $\sim 91\%$ is achieved in the forward direction compared with the $\sim 75\%$ signal amplitude in the backward direction for the waves propagating

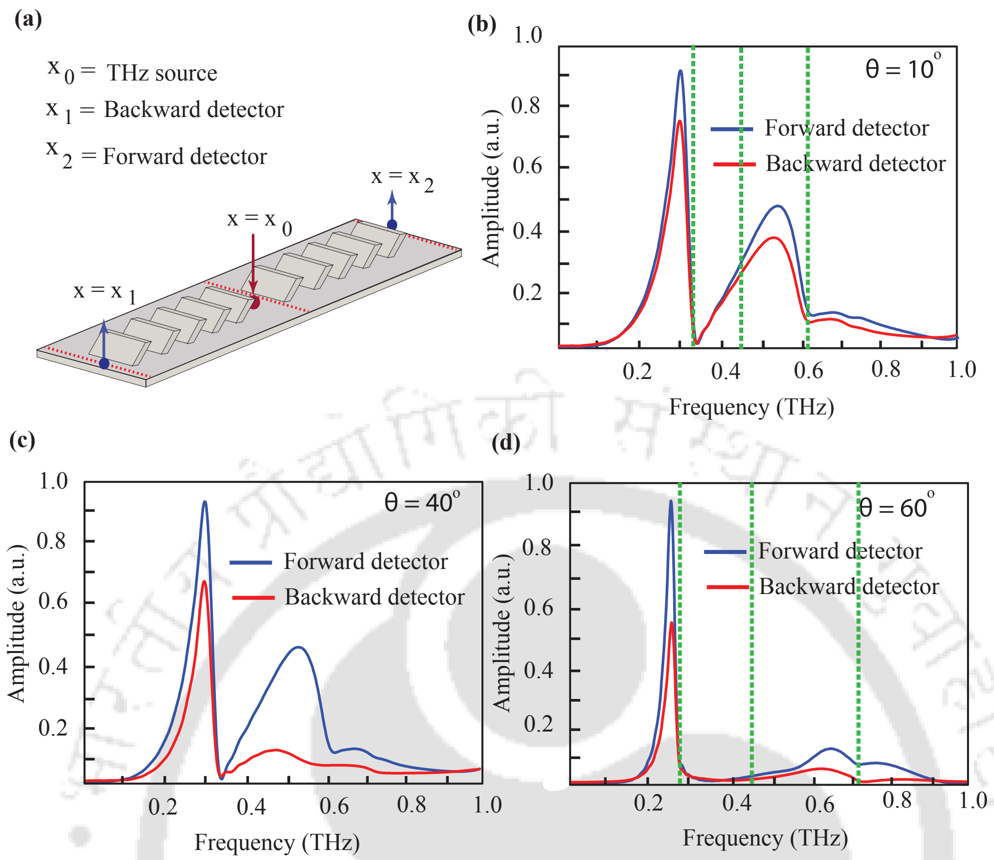

Figure 2.4: (a) Schematic of the THz waveguide depicting the positions of THz source, the backward detector, and the forward detector at $x = x_0$, $x = x_1$ and $x = x_2$ respectively. (b), (c) and (d) show the comparisons of THz amplitude transmission in the backward ($x = x_1$) and forward detector ($x = x_2$) positions for three different waveguides with pillars tilted at 10°, 40° and 60° respectively. The detectors are placed at a distance of 2 cm from the centre at both the ends.

an equal distance in both directions. While increasing the tilting of pillars, the waveguide transmission in the forward direction increases. For angles $\theta = 40°$ and 60°, an output amplitude of $\sim$ 93% and $\sim$ 94% in the forward direction are achieved, whereas signal amplitude drops to $\sim$ 67% and $\sim$ 54% in the backward detectors. Therefore, the proposed waveguides can allow to propagate the signal more effectively in a particular direction by changing the angle through which pillars are tilted.

Further, the field profiles of the terahertz modes supported by the proposed waveguide configuration are examined. The results are shown in Fig. 2.5 for the two different angles of 10° and 60° and other fixed values of the pillar dimensions i.e. length (l) = 100 μm, width (w) = 500 μm, height (h) = 100 μm, periodicity (p)

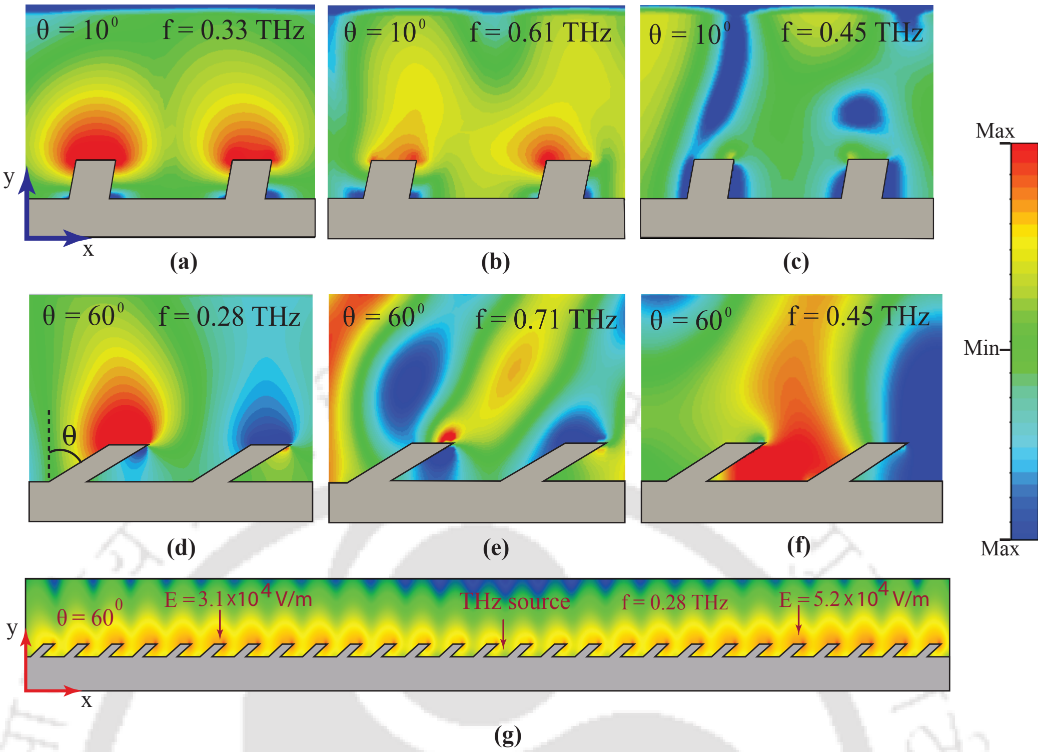

Figure 2.5: The field profiles of the THz modes in the x-y plane of the waveguide. (a) and (b) correspond to the fundamental (0.33 THz) and the higher order (0.61 THz) modes respectively, while (c) shows field profile at OFF-resonance i.e. 0.45 THz for the case with pillars tilted at an angle, $\theta = 10°$. Similarly, the field profiles for pillars tilted at angle, $\theta = 60°$ are shown in (d)-(f). Again, (d) and (e) correspond to the fundamental and higher order resonances, while (f) represents OFF resonance field, (g) shows electric field profile in both the directions keeping source at the center for the pillar tilted at $\theta = 60°$

.

$= 400\ \mu m$. The field profiles are examined at the first and second resonant (ON-resonances) frequencies and one OFF resonant frequency. For $\theta = 10°$, the first and 2nd resonances occur at 0.33 THz and 0.61 THz respectively. The field is strongly confined at the first resonance, however weakly confined at 2nd resonance as can be noticed through Fig. 2.5(a) and (b) respectively. At OFF-resonant frequency (0.45 THz), there is no field confinement at all as shown in Fig. 2.5(c). The field profiles for the angle $\theta = 60°$ at ON and OFF resonances are shown in Fig. 2.5(d)-(f). Again, fields are strongly confined at the resonant frequencies, however no confinement for OFF resonant modes. In Fig. 2.5(g), the electric field propagation is shown at the fundamental resonant frequency i.e. 0.28 THz along the waveguide comprising of pillars tilted at $\theta = 60°$, both in forward and backward directions.

As expected, the field propagates in both the directions of the waveguide when it is excited at the center i.e. $x = x_0$. For a fixed traveling distance in the forward and backward directions i.e. $x = x_1 = x_2$, the fundamental mode with similar field profiles is observed, however of different total field amplitudes. The ratio of the forward field amplitude to the backward field amplitude is calculated i.e. E_2/E_1 at $x_1 = x_2 = 1.5$ cm and it turned out to be 1.74. Clearly, the field amplitude is higher at $x = x_2$, indicating a more effective propagation in the forward direction.

In a terahertz plasmonic waveguide, the loss and confinement are the crucial factors to decide the performance of a waveguide. Therefore, these properties of the proposed geometry have also been examined for the guiding of terahertz modes. First, the confinement is analyzed in the transverse direction i.e. vertically

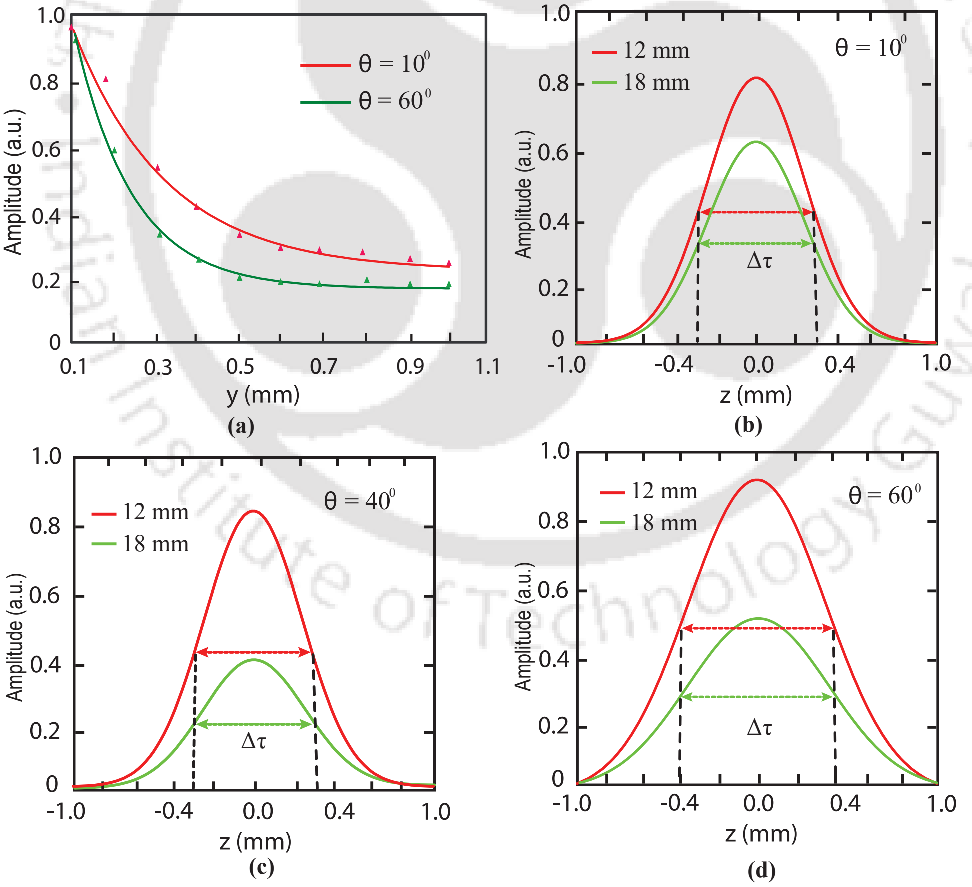

Figure 2.6: (a) The amplitudes of the fundamental THz surface mode probed at different positions vertically above the surface. The data is exponentially fitted to obtain the $1/e$ propagation lengths. (b), (c) and (d) Represent terahertz amplitude versus detector position in the lateral directions of the waveguide at $x = 12$ mm and $x = 18$ mm. The full width at half maximum (FWHM) is represented by $\Delta(\tau)$.

away from the surface. For this purpose, the total electric field is measured by translating the detectors away from the surface for the pillar angles 10° and 60° using the finite element time domain solver. Fig. 2.6(a) plots the measured peak spectral amplitude as a function of distance above the surface, along with an exponential fit which results in the $1/e$ propagation length of 0.52 mm for the bending angle $\theta = 10°$. The $1/e$ propagation length decreases as the angle increases. For $\theta = 60°$, it turns out to be 0.29 mm. Also the confinement of the fundamental terahertz modes has been evaluated in the lateral direction. This is done by placing detectors at different position in the lateral direction and measuring the total electric field amplitude. Fig. 2.6(b), (c), and (d) plot the calculated field amplitude as a function of the distance z in the lateral direction at two different positions, 12 mm and 18 mm, of the waveguide along the propagation direction for the bending angles $\theta = 10°$, 40°, and 60° respectively. Under the Gaussian fitting of the results, the calculated full-width at half-maximum (FWHM), $\Delta(\tau)$ are calculated to be $\sim$ 0.6 mm, 0.7 mm, and 0.8 mm for the bending angles $\theta =$ 10°, 40°, and 60° respectively for the fundamental guided THz mode.

Further, the ability of the pillar plasmonic waveguide to confine the fundamental terahertz modes at a certain position of the waveguide has been examined. A waveguide is designed, in which pillar height is gradually increasing in the steps of 10 μm, however other dimensions of the pillars i.e. length $(l) = 100$ μm, width (w) $= 500$ μm, and periodicity $(p) = 400$ μm remain fixed. In designing waveguide, pillar height is started with 10 μm and ended up with 550 μm. The waveguide geometry is excited with three different frequencies viz. 0.15 THz, 0.19 THz, and 0.24 THz, which correspond to the cut-off frequencies of the resonant modes for the pillar heights of 400 μm, 300 μm, and 200 μm, respectively. A similar study has been done for the slanted pillars pattern also for tilt angle of 60°. In this case, the excitation frequency was 0.28 THz which corresponds to the vertical pillar height of 100 μm. The cut-off frequencies are estimated from the dispersion relations of the fundamental modes calculated using Eigen mode solver of the simulation

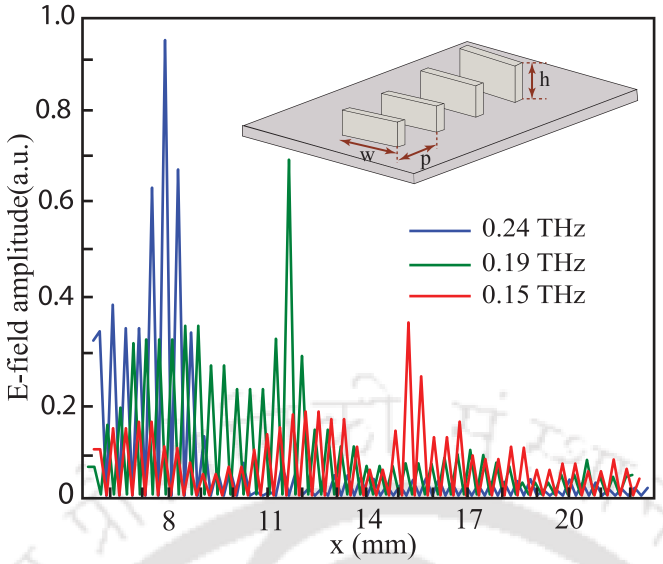

Figure 2.7: Variation of THz field amplitude, Ey versus distance, x i.e. the direction of propagation of the THz modes in a waveguide comprising pillars of increasing height. The red, green and blue traces correspond to 0.15 THz, 0.19 THz and 0.24 THz, respectively. The field is high at a position where incident THz frequency matches with the resonance frequency of the pillar. The inset shows the schematic of waveguide configuration with increasing height of the pillars.

package. The y-component of the electric field amplitude versus pillar position is plotted in Fig. 2.7. The inset shows the schematic of the waveguide configuration with increasing pillar height. One may note that the electric field amplitude at a particular frequency is higher at a certain pillar position. This occurs when incident frequency matches to the anti-resonant frequency of the resonant mode corresponding to a certain height of the pillar. In order to have a better understanding of the results, the electric field profiles are examined with waveguides excited by different frequencies. The results are shown in Fig. 2.8. Clearly, the fields of specific frequencies are highly confined at the positions where pillar′s height and corresponding resonant frequency matches to the incident frequency.

2.3 Discussions

In conclusion, the design, simulation and analysis of the terahertz modes in a plasmonic waveguide comprising sub-wavelength scale tilted pillars are presented. The dispersion relations of the fundamental THz mode supported by the pillars

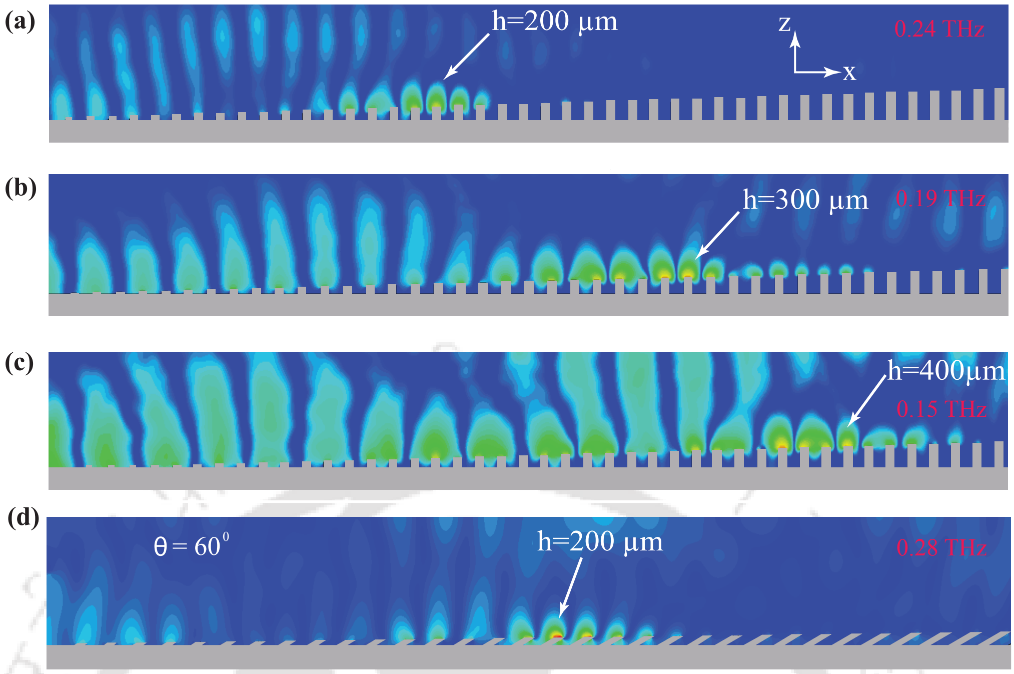

Figure 2.8: Field confinements of the fundamental THz mode in the x-y plane of the waveguide. (a) corresponds to the excitation frequency, 0.24 THz which results in field trapping at the pillar height, $h = 200\ \mu m$. Similarly, (b) and (c) correspond to frequencies 0.19 THz and 0.15 THz which show greater field confinements at 300 μm and 400 μm respectively. (d) shows field confinement for the slanted pillar pattern for tilt angle 60° at slanted height 200 μm, which corresponds to frequency 0.28 THz.

tilted at different angles are numerically calculated. An increase in the bending of pillars results in lower cut-off frequency and better field confinement of the THz modes. By arranging pillars on both sides of the incident THz, it is observed that the THz mode can be more effectively guided in a particular direction depending upon the orientation and angle through which pillars are tilted. The propagation of guided THz modes in tilted pillars waveguide is independently confirmed through a semi-analytical transmission line model. The model enables to predict the anti-resonant frequencies of the guided modes for certain specific values of inductance, capacitance and mutual inductance of the pillars. Further, field confinements of the fundamental THz modes are examined and a strong confinement of the modes is observed onto the pillars at resonant frequencies. For $\theta = 10°$, $1/e$ decay length is found to be $\sim$ 0.52 mm in transverse direction for the fundamental THz mode. Furthermore, the ability of confining a THz mode of certain frequencies is analyzed at a specific position. This is achieved by designing a terahertz waveguide with gradually increasing heights of the pillars. The present study on plasmonic waveguides could be significant in designing active networks, slow light systems and buffers operating at terahertz frequencies.

Chapter 3

Internally corrugated plasmonic terahertz waveguide

Contents

Plasmonic waveguides have the ability to support highly confined modes on the metal surface which could be significant in a variety of applications ranging from engineering to medical science. At terahertz frequencies, one can construct planar plasmonic waveguides by patterning the metal surface with periodical corrugations as discussed in Chapter 2. In order to use plasmonic guided wave devices in practical applications, one require rigorous and comprehensive understanding of the corrugated patterns and their effect on the plasmonic properties. It is also required to explore more optimal designs including internal corrugations of the structure in order to achieve desirable plasmonic responses.

The plasmonic waveguide geometries are capable of supporting highly confined guided modes that can exhibit slow light properties or in other words lower group velocities of the modes. The slow light systems have significance in the construction of photonic devices such as optical buffers, storage systems etc [104–106]. The development of slow light devices and related research has been pursued with great interest recently. In this context, Baba *et al.* have experimentally investigated a slow-light waveguide based on photonic crystal for buffering [107]. More recently, Zhang *et al.* numerically reported slow-light phenomena in periodic plasmonic waveguide [108]. They proposed dielectric-metal-dielectric and dielectric-dielectric-metal waveguide designs to realize slow-light effect exhibiting low loss. These investigations have been mostly carried out in the optical or near infrared domain. In terahertz domain, a limited but valuable investigations have been reported [109–111]. Manjappa *et al.* have showed the slow light behavior in terahertz metasurfaces [109]. Keshavarz *et al.* have proposed a two H-shaped structured planar semiconductor metamaterial and showed lower group velocity dispersion system [111]. More rigorous investigations on slow light in terahertz domain are required to be persuaded. It is also required to investigate the optimum geometry resulting in the lower group velocity. The alteration in the properties of guided modes supported by terahertz plasmonic waveguides and associated slow light properties are significant from the device construction point of view which are lacking in the terahertz regime. This issue can be addressed by incorporating internal corrugations in the plasmonic waveguides that can cause additional changes in the already propagating terahertz modes.

In this chapter, the guided mode propagation in the planar plasmonic terahertz waveguides comprising of periodically arranged internally corrugated V-shape structures are analyzed along with the slow light properties. In Section 3.1, the proposed waveguide geometry is discussed and the time-domain and frequency domain waveguide transmission spectra are examined under different steps of internal corrugations. A semi-analytical model in support of the numerically observed waveguide transmission results is reported in Section 3.2. Section 3.3 describes dispersion relations of fundamental modes supported by the waveguides under the different steps of corrugations. The slow light properties of the corrugated waveguides are examined in Section 3.4. In this section, we have also examined the trapping of light of certain frequency at a certain corrugation. Finally, in Section 3.5 the results are summarized.

3.1 Schematic of terahertz plasmonic waveguide

The schematic of the proposed plasmonic waveguide geometry is shown in Fig. 3.1. The waveguide geometry is comprised of periodically arranged V-shape structures with three steps of internal corrugations. The steps of internal corrugations are indicated by n. In this study, n is assumed as 2, 4, and 8 in order to examine the dependence of guided mode cut-off frequencies and their slow light properties on internal corrugations. It may be noted that if one increases the number of steps to infinity then the structure resembles with the V-groove. In this study of waveguide transmission with internal corrugations, the following parameters are considered and assumed to be constant: length (l) = 200 μm, width (w) = 1500 μm, depth (h) = 350 μm, thickness of substrate (d) = 800 μm, and periodicity (p) = 250 μm. The fabrication of this type of plasmonic waveguide has been discussed in Section 1.2.4.

3.2 Waveguide transmission: Simulation and theory

First, the waveguide amplitude transmission of the proposed terahertz plasmonic waveguides has been examined. In numerical simulations, the waveguides are excited with a discrete source of single cycle terahertz waveform from one end of the waveguide. The signal once coupled to the corrugated structures, propagates

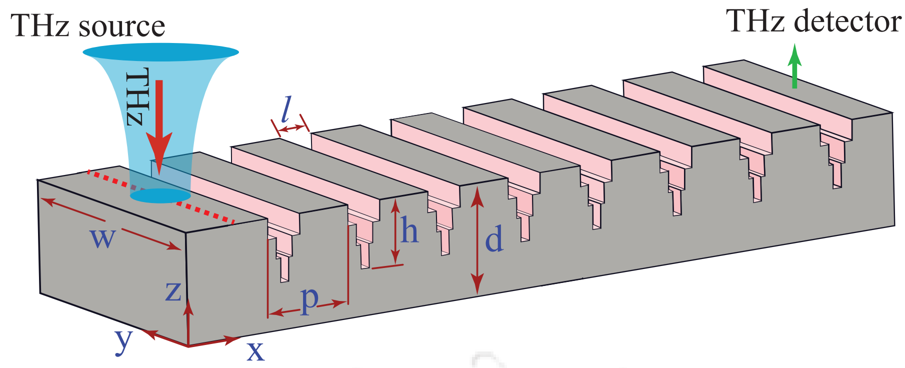

Figure 3.1: Schematic of a planar plasmonic THz waveguide. (a) 3-Dimensional view of the waveguide comprising one dimensional array of periodic corrugations. The parameters l, w, h and p represent the length, width, depth and periodicity of the structure. The thickness of the substrate is represented by d.

along the designed one dimensional waveguide and finally detected at the other end of the waveguide. The detected time domain signal is converted into the frequency domain spectra using Fast Fourier Transform (FFT). The numerical simulations are performed using finite element time domain solver of the CST Microwave Studio simulation software.

A 3 cm long planar waveguide is assumed with internal corrugations in the steps of n = 2, 4, and 8 while maintaining the depth of 350 μm. The results in the form of frequency domain spectra are shown in Fig. 3.2(a), (b), and (c) respectively. It is apparent that the periodically corrugated waveguide exhibit resonant behavior. As one increases n, the anti-resonant frequencies of the modes as well as the amplitude of the resonances gets changed. The anti-resonance frequency of the fundamental as well as higher order mode gets blue shifted with increasing steps of the internal corrugations. On the other hand, the amplitude of the fundamental mode increases with increasing n, however it decreases for the higher order mode. It is observed that for large n, the higher order mode nearly vanishes resulting in a single mode propagation . Therefore, internal corrugations may be used to switch the response of waveguide from multimode to single mode propagation.

In order to confirm the anti-resonant behavior of the proposed plasmonic

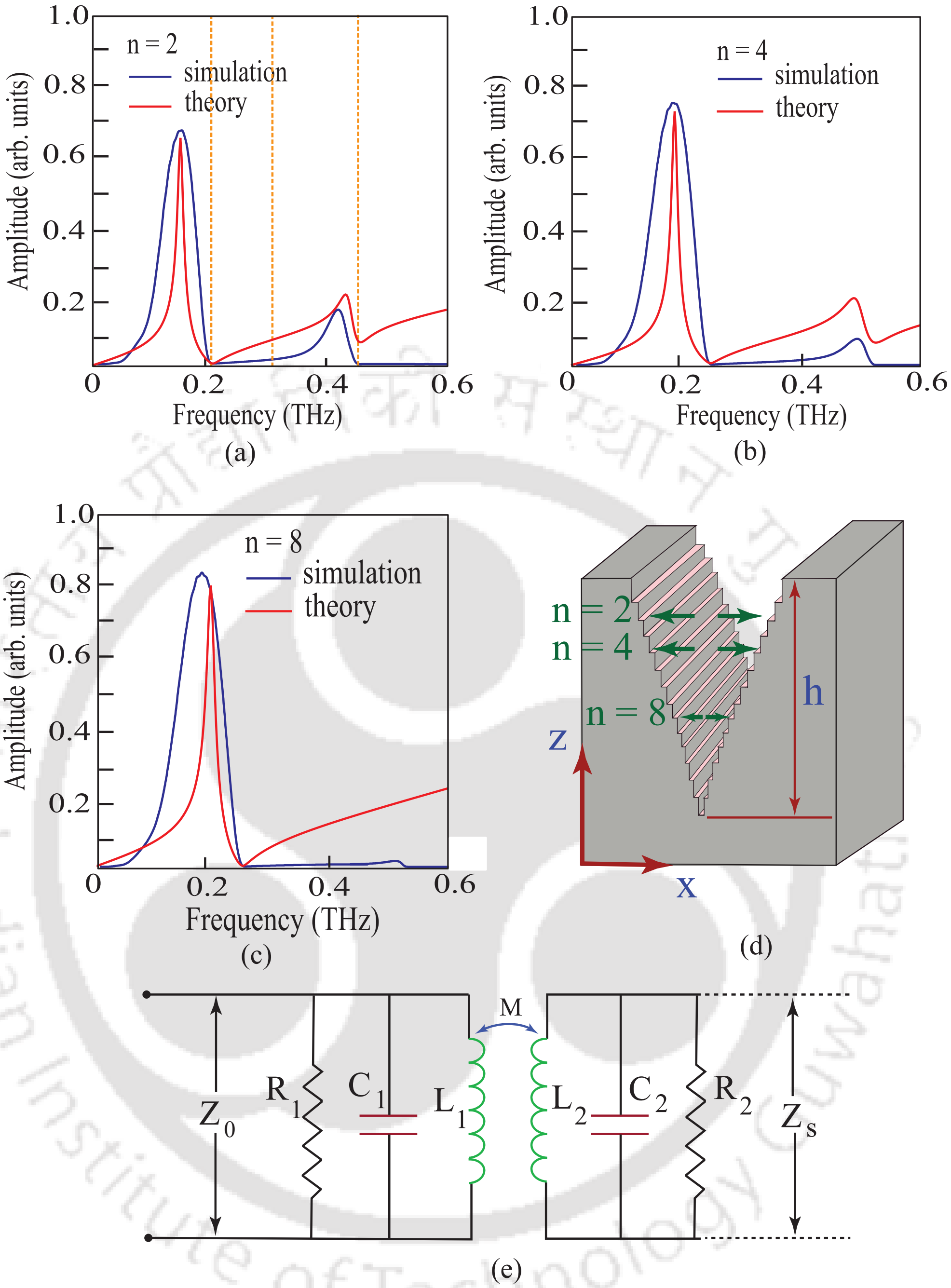

Figure 3.2: (a), (b) and (c) represent the terahertz amplitude transmission from the simulation and theory for the plasmonic waveguides comprising periodic structure with $n = 2$, 4 and 8 steps of corrugations. The blue traces correspond to the numerically simulated results, while the red traces represent waveguide transmission from an equivalent transmission line - *RLC* circuit model. (d) Depicts a 3-D view of an internally corrugated unit structure. (e) Schematic of the transmission line - *RLC* circuit model. The R_1, L_1, C_1 in the circuit represent the resistance, inductance, capacitance for 1^{st} resonance and R_2, L_2, C_2 represent the same for 2^{nd} resonance respectively. M is the mutual inductance of the circuit. The Z_0 and Z_S correspond to the intrinsic impedance and circuit impedance respectively.

waveguide, an equivalent semi-analytical transmission line model is employed. The results of the amplitude transmission from the model are shown through red traces in Fig. 3.2(a),(b) and (c). It is noticed that the theory predicts the resonant behavior of the waveguide in analogous to the numerically simulated results for certain values of resistance, inductance, capacitance, and mutual inductance for the different cases. The details of the analytical transmission line model are as follows:

In the semi-analytical model, metal is assumed to have a very high carrier density with V-shaped grooves behaving like an RLC circuit under the transmission line approximation. It is considered that a unit cell corresponds to one V-shape corrugated structure. The circuit model of a unit cell is represented by two RLC circuits where R_1, L_1, C_1 correspond to the 1st resonance and R_2, L_2, C_2 correspond to the 2nd resonance. These two resonances are coupled through the mutual inductance M. The circuit model of a unit cell under the transmission line theory is shown in Fig. 3.2(e). One can calculate the intrinsic impedance (Z_0) of this circuit [89], which is given by

$$Z_0 = \frac{120\pi}{\sqrt{\epsilon_i}[\frac{w}{d} + 1.393 + 0.667\ln(\frac{w}{d} + 1.444)]}, \tag{3.1}$$

where, ϵ_i is the effective dielectric constant of metal; w is the width of the groove and d is the thickness of the substrate. Now, the impedance of this circuit model (Z_S) can be written as,

$$Z_S = \frac{Z_1 Z_2 + \omega^2 M^2}{[Z_1 + Z_2 - 2j\omega M]}, \tag{3.2}$$

where, ω and M represent angular frequency and mutual inductance respectively. Z_1 and Z_2 correspond to the impedances due to the 1^{st} and 2^{nd} RLC circuits respectively. These impedances can be written as:

$$Z_1 = \frac{L_1 R_1}{L_1 + jR_1C_1(\omega L_1 - \frac{1}{\omega C_1})}, \qquad Z_2 = \frac{L_2 R_2}{L_2 + jR_2C_2(\omega L_2 - \frac{1}{\omega C_2})}, \tag{3.3}$$

The normalized transmission coefficient, $t(\omega)$ of this transmission line- RLC circuit model will follow the normal form

$$t(\omega) = \frac{2Z_S}{Z_0 + Z_S}, \tag{3.4}$$

From Eq. (3.4) one can calculate the waveguide transmission and predict anti-resonant frequencies of the resonant modes resulting from the internally corrugated V-shaped structures. As it is discussed above that this model enables to predict the anti-resonant frequencies corresponding to $n = 2$, 4, and 8 corrugated steps in the structures for certain specific values of resistance, inductance, capacitance and mutual inductance which are given in Table 3.1. The values of R, L, C, and M are obtained by fitting the transmission amplitude obtained through the simulation to the equation (5). One may note the resonances of the modes are broad in numerically simulated results. The broadness of a resonance can be attributed to the scattering, dispersion, and diffraction losses that a wave experiences when it propagates along the corrugated pattern. Such losses are not considered in the transmission line model. In order to examine the field confinement of the modes along the waveguide, field profiles are monitored at the ON and OFF resonant frequencies. The results are shown in Fig. 3.3 for $n = 2$ and the waveguide parameters are: length (l) = 200 μm, width (w) = 1500 μm, depth (h) = 350 μm, periodicity (p) = 250 μm. The field profiles are examined at the first and second

Parameter	$n = 2$	$n = 4$	$n = 8$
Resistance, R_1 (Ohm)	3.5	4	2.75
Inductance, L_1 (fH)	93.2	73.2	68
Capacitance, C_1 (pF)	5.8	5	5.45
Resistance, R_2 (Ohm)	0.45	0.4	0.5
Inductance, L_2 (fH)	8.14	8.27	0.84
Capacitance, C_2 (pF)	15.7	11.4	14.5
Mutual Inductance, M (fH)	96	76	96

Table 3.1: Different parameters used in TL-RLC circuit model for internal corrugations $n = 2$, 4, and 8.

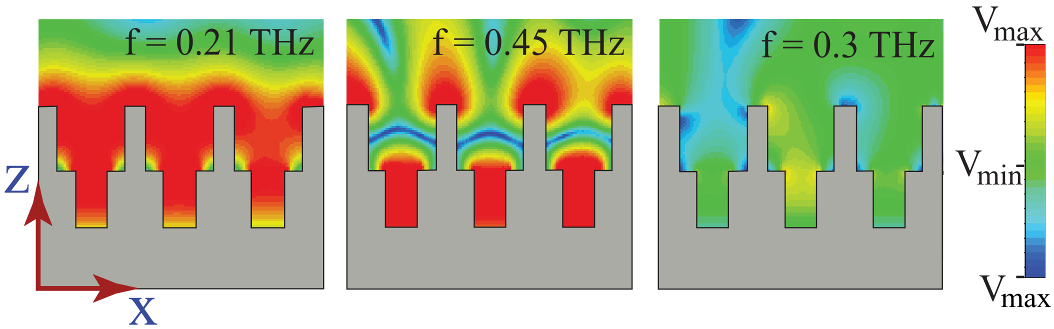

(a) (b) (c)

Figure 3.3: The field profiles of the THz modes in the x-z plane of the waveguide. (a) and (b) correspond to the fundamental (0.21 THz) and the higher order (0.45 THz) modes respectively, while (c) shows the field profile at OFF-resonance i.e. 0.3 THz for the case of $n = 2$.

resonant (ON-resonances) frequencies and one OFF resonant frequency. The first and second resonances occur at 0.21 THz and 0.45 THz respectively. The field is strongly confined at 1^{st} and 2^{nd} resonances as can be noticed in Fig. 3.3(a) and (b) respectively. At OFF-resonant frequency (0.3 THz), there is no confinement as it is apparent from Fig. 3.3(c).

3.3 Dispersion relations of the fundamental modes

Next, in order to further analyze the waveguide transmission results as well as validate the anti-resonant frequencies of the resonant modes, dispersion relations of the fundamental mode have been examined for three different steps of corrugations. In order to calculate dispersion relations, the technique of finite element Eigen mode solver is used, with a periodic boundary condition along the propagation direction and absorbing layers along the transverse direction. Perfect electrical conducting (PEC) boundary condition is assumed for metal substrate owing to its high conductivity at terahertz frequencies. The results of the dispersion relations for different steps of corrugations are shown in Fig. 3.4. The straight line in the figure indicates the light line. The blue, green, and red color traces represent dispersion relations of the fundamental modes for n = 2, 4, and 8 steps of the internal corrugations respectively. In the dispersion relations, it is notice that the

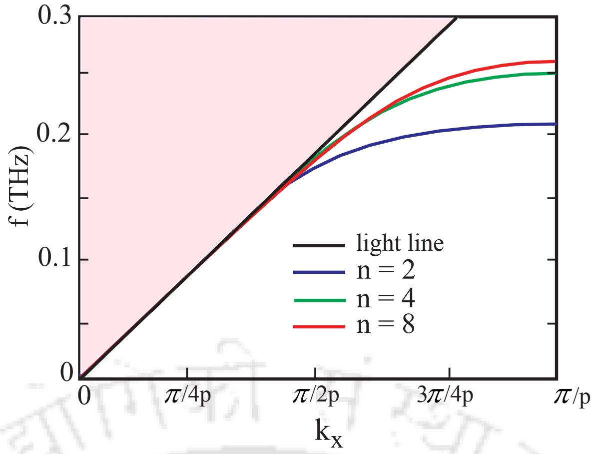

Figure 3.4: Numerically calculated dispersion properties of the fundamental guided terahertz mode in the proposed plasmonic waveguide for different steps of internal corrugations.

frequency monotonically increases in the beginning with the wavenumber, however it saturates for the large wave number. For $n = 2$, saturation frequency is found to be 0.21 THz. This value ideally corresponds to zero group velocity and represents the cut-off frequency of the fundamental mode. As n increases, the dispersion curves shift towards the light line and saturate to higher values. For $n = 4$ and 8, the cut-off frequencies turn out to be 0.25 THz and 0.26 THz, respectively. One may note that the anti-resonant frequencies obtained from frequency domain spectra in Fig. 3.2(a), (b), and (c) match with the saturation frequencies of the dispersion relations for the same design parameters.

3.4 Slow light properties of the plasmonic waveguides

The slow light devices operating at terahertz frequencies could be significant in the construction of terahertz buffers and storage applications. Next, the potential of the proposed waveguide configurations is examined in slowing down the propagating terahertz surface plasmon modes. In Fig. 3.5, the normalized group velocities (V_g /c) of the fundamental terahertz modes are plotted with respect to frequency observed in the plasmonic waveguides comprising n = 2, 4, and 8 steps

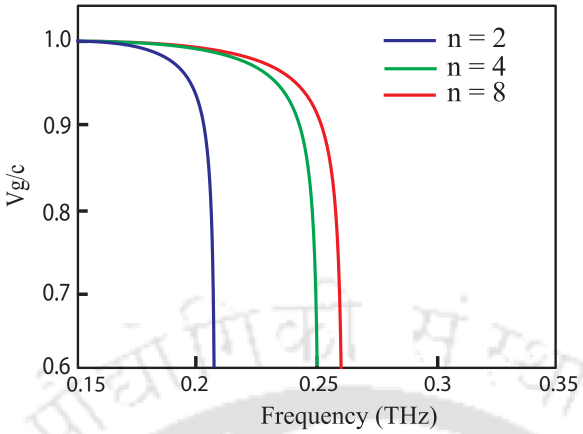

Figure 3.5: The variation of normalized group velocity versus frequency resulting from the plasmonic waveguide having different steps of internal corrugations. The other parameters are: length (l) = 200 μm, width (w) = 1500 μm, depth (h) = 350 μm and periodicity (p) = 250 μm

of internal corrugations. The depth of all the structures is assumed to be constant i.e. $h = 350\ \mu m$. The c and V_g represent velocity of light in the free space and group velocity of fundamental mode respectively. It is apparent from the figure that group velocity of the fundamental mode depends upon the internal corrugations of the structure. Therefore, one can tune the group velocity based upon the internally corrugated steps. Further, it can be noticed that an increase in internal corrugations results in higher group velocity of the fundamental mode.

Next the slow light properties of the internally corrugated V-shape structures are examined for different depths and compared to the V-grooves without internal corrugations. Three depths are assumed for this purpose h = 250 μm, 350 μm, and 450 μm for the study and results are shown in Fig. 3.6. In Fig. 3.6(a) normalized group velocity is shown w.r.t. frequency of the fundamental mode supported by internally corrugated V shape structure for three depths. One can notice that as the depth of structures increases, the group velocities vary and the curves saturate at different frequencies. For the depths of 250 μm, 350 μm and 450 μm, the group velocities becomes zero at 0.31 THz, 0.24 THz, and 0.21 THz respectively. Therefore, an increase in the depths of structures, results in lower group velocity i.e. slow-light behavior at a certain frequency. In Fig. 3.6(b), plasmonic waveguide having V-grooves are examined for same three depths, as discussed above however, without any internal corrugations, In this case, the saturation frequencies and group velocities are higher compared to the case of internally corrugated

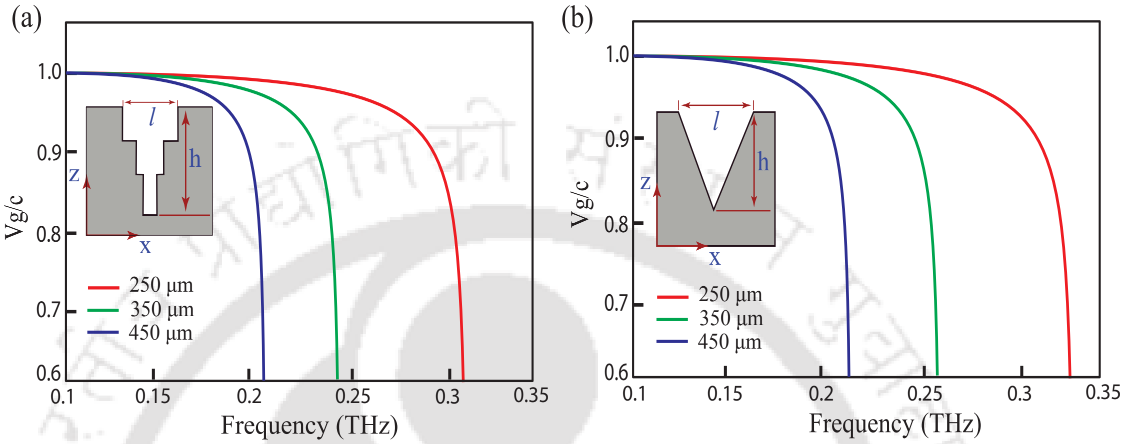

Figure 3.6: (a) and (b) show the variation of normalized group velocity versus frequency of the fundamental mode supported by the plasmonic waveguide comprising structures of different shapes for three different depths h = 250 μm, 350 μm, and 450 μm. The unit cell of the corresponding shape is shown in the inset.

V-shape structures. Therefore, internal corrugations in V-shape structure results in the reduction of group velocity. As the role of internal corrugations is quite important in controlling the slow-light properties of the modes, next a waveguide with gradually increasing depth of the internally corrugated structures is designed and examined to explore its ability to confine a specific frequency at a certain position indicating the slow-light behavior. The results are shown in Fig. 3.7. In the design, the depth of the structures is increased in the steps of 50 μm and number of corrugated steps i.e. n is also increased by one at every increment in the structure depth. The other parameters of the waveguide are assumed to be fixed i.e. length (l) = 200 μm, width (w) = 1500 μm and periodicity (p) = 250 μm. The depth of the first structure is 150 μm, while that of last one is 550 μm. In this waveguide, every structure exhibits a different resonant frequency. The waveguide is excited with three different frequencies i.e. 0.21 THz, 0.24 THz and 0.31 THz. The frequencies are found to be highly confined at different positions.

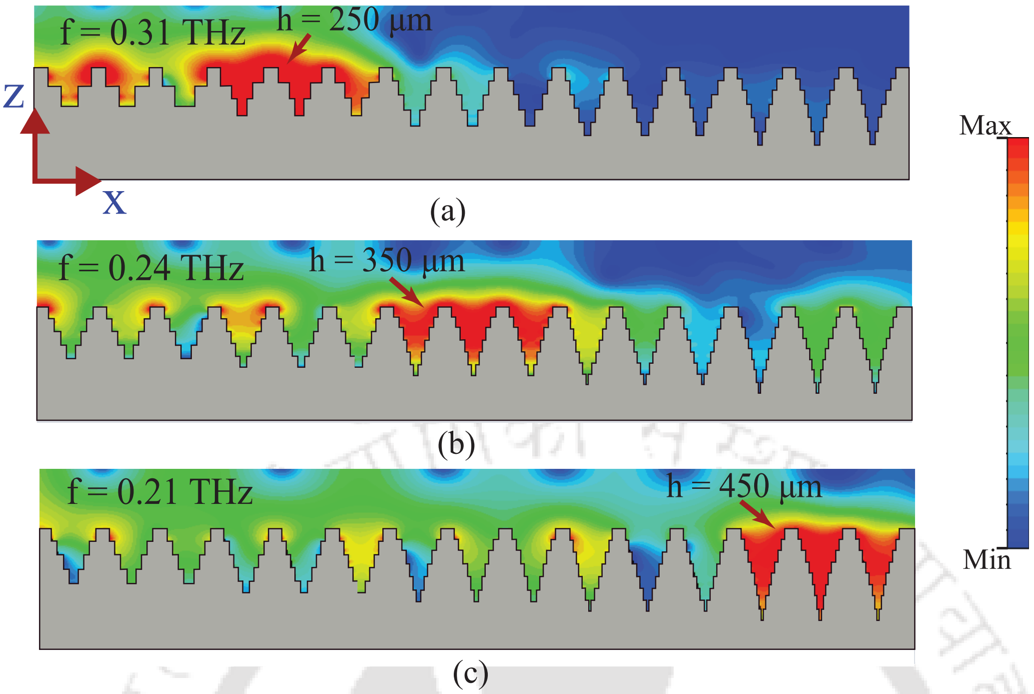

Figure 3.7: (a), (b), and (c) show the field confinements of the fundamental THz mode in $x-z$ plane of the waveguide. (a) Corresponds to the excitation frequency 0.31 THz which results in field trapping at the corrugation depth, h = 250 μm. Similarly, (b) and (c) correspond to frequencies, 0.24 THz and 0.21 THz, which show greater field confinements at h = 350 μm and h = 450 μm, respectively.

For instance, in the case of 0.21 THz incident frequency, the field is highly confined at h = 450 μm. The greater field confinement can be attributed to the matching of the cut-off frequency of a structure to the incident frequency.

Further, the slow-light effect is examined in the plasmonic waveguides comprising grooves of same depth and length, but an increasing number of internally corrugated steps. In order to do so, three planar plasmonic waveguides are designed comprising grooves of length l = 200 μm, width w = 550 μm and depth h = 550 μm. The periodicity (p) of the grooves is assumed to be 400 μm in all the waveguides. The internal corrugations are increasing by one step after two consecutive grooves of same step profile. The number of internal steps in the grooves are increased from n = 1 to n = 8 in all waveguides. The dispersion relations and resonant frequencies corresponding to different internal steps in the grooves are numerically examined for same length, depth, and periodicity of the internal corrugations. For n = 2, n = 6, and n = 8, the resonant frequencies turns out to

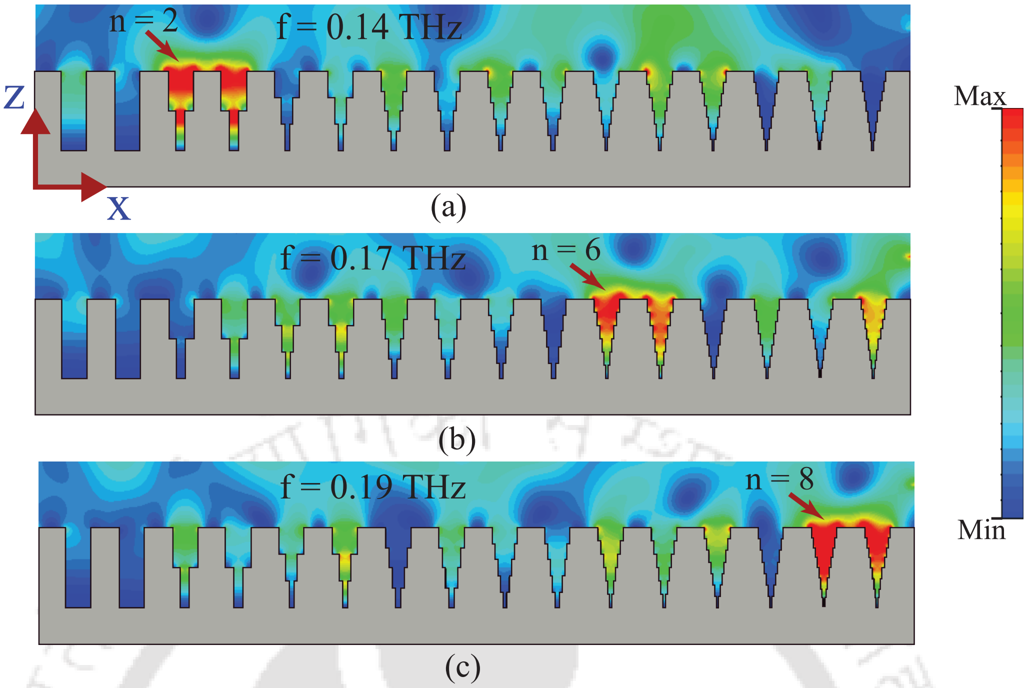

Figure 3.8: The electric field profiles of the terahertz surface plasmon modes in the $x-z$ plane of the plasmonic waveguides comprising grooves of same length, depth and periodicity at (a) 0.14 THz, (b) 0.17 THz, and (c) 0.19 THz. The fields are strongly confined at grooves having n = 2, n =6, and n = 8 for the excitation frequencies, 0.14 THz, 0.17 THz, and 0.19 THz, respectively. The groove parameters are: $l = 200\ \mu m$, $h = 550\ \mu m$, and $p = 400\ \mu m$.

be 0.14 THz, 0.17 THz, and 0.19 THz, respectively. In order to have an appreciation of slow light effect, the waveguides are excited with three frequencies viz. 0.14 THz, 0.17 THz, and 0.19 THz. The results of electric field profiles at these frequencies are shown in Fig. 3.8. In Fig. 3.8(a), it may be observed that the frequency, 0.14 THz strongly confines at the grooves having internal step, n =2. Similarly, frequencies, 0.17 THz and 0.19 THz are strongly confined at n = 6 and n = 8 respectively as indicated in Fig. 3.8(b) and (c). The strong confinement of electric field at a certain groove clearly indicates the slow light property of the THz wave of specific frequency.

3.5 Discussions

In conclusion, the terahertz guided mode propagation is numerically examined and analytically modeled in a plasmonic waveguide comprising of sub-wavelength scale structures corrugated internally. The proposed geometries support highly confined guided modes whose properties are found to vary with the internal corrugations. It is observed that for a specific set of parameters of the structures, the higher order resonance vanishes with the increase in the steps of internal corrugations. The dispersion properties are also numerically analyzed with respect to different corrugations in support of the resonant behavior of the proposed waveguides. The resonant behavior of the THz mode has been independently confirmed through a semi-analytical transmission line model. Further the slow light properties of the fundamental modes supported by the waveguides are examined under different steps (n) of internal corrugations. As one increases the number of corrugated steps within the structures, the group velocity increases. The results are compared with the plasmonic waveguides comprising of V grooves without internal corrugations. The modes in internally corrugated V-shape structure are found to exhibit lower group velocities. The slow-light properties of the fundamental modes are also investigated in waveguides comprising of gradually increasing depth of internally corrugated structure. It is observed that a specific frequency (e.g. 0.31 THz) is strongly confined to a structure ($h = 250\ \mu m$) where its resonant frequency matches with incident frequency. The guided mode properties of the proposed plasmonic waveguide and their dependence on internal corrugations of the structures could be significant in the construction of terahertz devices such as terahertz buffers, storage devices etc.

Chapter 4

Plasmonic terahertz waveguide based sensor

Contents

There has been considerable interest in developing plasmonic waveguides in last decade. The design, fabrication, and characterization of plasmonic waveguides as well as recent developments in this area have been discussed in detail in Chapter 1. Even though several remarkable developments have been reported in plasmonic terahertz waveguides, none of the studies has been focused on their potential as sensors to the best of our knowledge.

The sensing applications at terahertz frequencies have been widely exploited using the technique of parallel plate waveguide (PPWG). This technique relies on two parallel metal plates sandwiching a thin layer of air gap where the analyte is adsorbed on one of the plates. Terahertz is coupled from one end of the waveguide and absorption features of the analyte resulting from its molecular vibrations are probed at the other end. In this context, Mendis and Grischkowsky had first reported the undistorted and low loss TEM propagation of terahertz pulses into the parallel plate copper waveguide, which could be significant in a variety of applications including sensing [15]. The initial demonstration of the parallel plate waveguide led to the measurement of 20 nm water layer using the technique of terahertz time domain spectroscopy (THz-TDS) [112]. Subsequently, Melinger *et al.* experimentally characterized the terahertz (THz) vibrational spectroscopy of organic polycrystalline thin films using THz-TDS in this configuration. It was observed that vibrational line widths could be narrower if the waveguide films are cooled to liquid nitrogen temperature because of the suppression of inhomogeneous broadening [113]. Laman *et al.* have used this technique for the identification and line narrowing of the terahertz vibrational modes of several different small biological tissues [114].

In plasmonic waveguides, the electric field of terahertz mode is strongly confined in the grooves and therefore, could be important in sensing analyte with greater sensitivity when it is filling the grooves. Unlike PPWG, where low loss TEM mode is used to probe the absorption features, the sensing in plasmonic waveguide is achieved via the frequency shifting technique of the terahertz mode for different refractive indices of the analyte. The waveguide technique also offers longer interaction of the analyte with the surface mode, resulting in better sensing characteristics compared to the direct transmission approach.

In this chapter, we examine the sensing capabilities of the fundamental resonance mode supported by the plasmonic waveguide comprising of rectangular corrugations. In our efforts to improve sensing characteristics, we have also examined sensing capability of the V-grooves constituting the plasmonic waveguide and compared sensing parameters with that of the rectangular grooves. In Section 4.1, we have examined the dispersion relations of the fundamental modes supported by the plasmonic waveguide comprising rectangular grooves filled with different refractive indices of the polyimide. We calculated corresponding frequency domain waveguide transmission spectra to establish the sensing capability of the plasmonic waveguide in Section 4.2. A semi-analytical transmission line model to confirm numerically observed waveguide transmission results is described in Section 4.3. Section 4.4 discusses various sensing parameters viz. frequency shift versus refractive index, the sensitivity and the figure of merit of the fundamental mode in case of rectangular grooves and V-grooves. In Section 4.5, we have discussed the results.

4.1 Schematic of THz plasmonic waveguide sensor and dispersion properties

The schematic of the proposed plasmonic waveguide geometry is shown in Fig. 4.1(a). The waveguide geometry is composed of a metallic substrate having periodically arranged one dimensional array of rectangular grooves. The top surface of the waveguide along with the grooves are filled with the polyimide. The grey and yellow colors in the schematic indicate the metal substrate and the polyimide respectively. The groove parameters are given as: length (l) = 0.5 mm, width (w) = 0.2 mm, depth (h) = 0.5 mm. The thickness of metal substrate, (d) is 0.8 mm and periodicity (p) is 0.4 mm. The periodicity of the substrate is assumed to be fixed throughout our study. The total length of the waveguide is considered to be 30 mm. The excitation of plasmonic waveguide with a single cycle THz waveform and its detection have been discussed in Chapter 2. The detected time domain signal is converted into the frequency domain spectra using Fast Fourier Transform (FFT). Again we use CST Microwave Studio simulation software to perform our numerical study. The THz plasmonic waveguide sensor design can be fabricated, which has been discussed in Section 1.2.4 in Chapter 1.

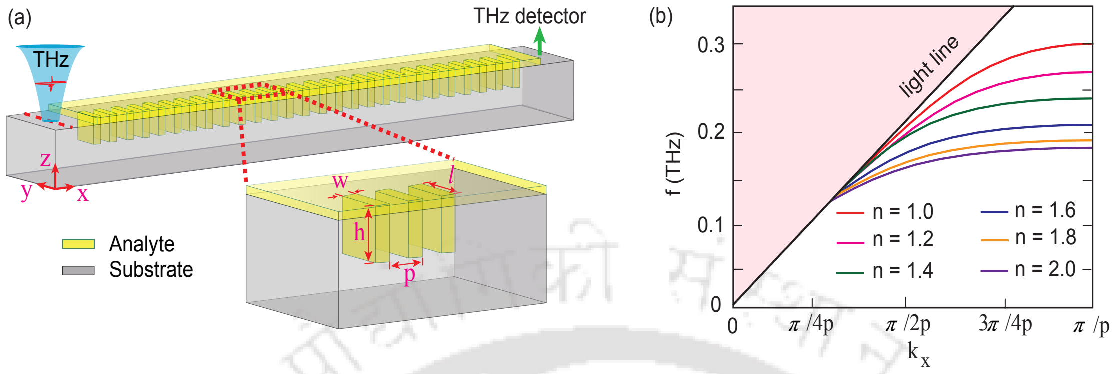

Figure 4.1: Schematic of a planar plasmonic THz waveguide. (a) 3-Dimensional view of the waveguide comprising one dimensional array of periodic corrugations. The parameters 'l', 'w', 'h' and 'p' represent the length, width, depth and periodicity of the structure. The analyte is present in the rectangular dimples as well as on the substrate. (b) Numerically calculated dispersion relations of the fundamental terahertz mode in the proposed plasmonic waveguide having dimples filled with analytes of different refractive indices.

In order to ensure plasmonic response of the waveguide with and without analyte, we first examined dispersion relations of the fundamental modes in the proposed waveguide geometry. To calculate dispersion relations, we used the technique of finite element Eigen mode solver, with a periodic boundary condition along the propagation direction and absorbing layers along the transverse direction. We assumed perfect electrical conducting (PEC) boundary condition for metal substrate owing to its high conductivity at terahertz frequencies. The results of the dispersion relations for different refractive indices of analyte are shown in Fig. 4.1(b). The black colored straight line in the figure indicates the light wave. The traces with different colors represent dispersion relations of the fundamental mode for different refractive index values (n) of the polyimide. In the dispersion plots, it may be noticed that the frequency monotonically increases with the wavenumber initially, however it saturates at the boundary of 1st Brillouin zone. For 'n' =1, we get saturation frequencies at 0.3 THz. This value ideally corresponds to zero group velocity. When the refractive index of the substance increases, the dispersion curve shifts away from the light line and saturates to a lower value. For, ‘n’ = 1.2, 1.4, 1.6, 1.8, and 2, the cut-off frequencies turn out to be 0.27 THz, 0.24 THz, 0.21 THz, 0.19 THz, and 0.18 THz, respectively.

4.2 Plasmonic waveguide based sensing: Simulation and theory

In order to investigate sensing capabilities of the proposed plasmonic waveguide, we used the technique of frequency shift of the fundamental mode of the waveguide transmission with the change in refractive index of the polyimide. More specifically, we focused on a change in the anti-resonant frequency of the modes when grooves are filled with analyte with respect to the intrinsic anti-resonant frequencies (i.e. without any analyte). It may be noted that the anti-resonant frequencies are quite significant in plasmonic waveguides as they occur from interference of discrete spectrum and continuum spectrum. First, we study waveguide transmission spectra of the plasmonic waveguide having rectangular grooves without any analyte. The corresponding frequency domain spectrum is reflected by the red trace for $n = 1$ in Fig. 4.2. Subsequently, the polyimide substance of different refractive index is filled in the grooves and corresponding waveguide transmission is calculated. One may use the technique of spin coating or drop casting for depositing analyte into the grooves as well as onto the surface. In the waveguide transmission spectra, a shift in the anti-resonant frequency is observed as the grooves are filled with the analyte. For ‘n’ =1, the anti-resonant frequency is found to appear at 0.3 THz, however it shift to 0.18 THz when analyte refractive index is $n = 2$. For our study, we varied refractive index as ‘n’ = 1, 1.2, 1.4, 1.6, 1.8, and 2.0 and observed a red shift in the anti-resonance frequency of the fundamental mode. Clearly, the shift in frequency is observed because of an interaction between the highly confined electric field of the mode at the surface and the analyte present there.

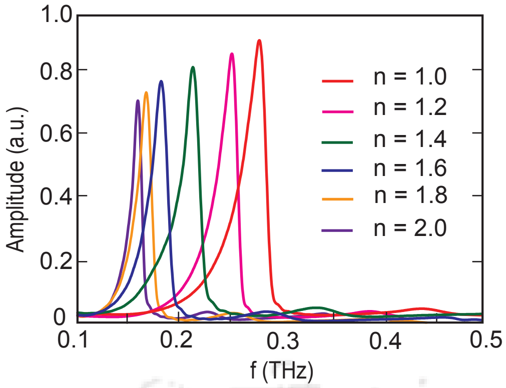

Figure 4.2: Numerically simulated frequency domain terahertz waveguide transmission for the plasmonic waveguides having rectangular dimples filled with refractive indices of i.e. 'n' = 1, 1.2, 1.4, 1.6, 1.8, and 2.

4.3 Semi-analytical transmission line model

In order to confirm resonant behavior of the proposed plasmonic waveguide with and without analyte, we employ an equivalent semi-analytic transmission line model. The model not only validates our numerical findings, but also allow more physical insight inside the system. The transmission line approach in context of plasmonic structures has been discussed in detail in reference 63. The schematic of the transmission line LC (TL -LC) circuit model is shown in Fig. 4.3(a). In the semi-analytical model, we assumed metal to have very high carrier density with constituent rectangular corrugations behaving like an LC circuit under the transmission line approximation. We consider that a unit cell comprises of two corrugations which are coupled through the mutual inductance, M. Each resonance of the corrugations of the unit cell is represented by an LC circuit. The intrinsic impedance Z_0 of this circuit [89] is given by

$$Z_0 = \frac{120\pi}{\sqrt{\epsilon_i}[\frac{w}{d} + 1.393 + 0.667\ln(\frac{w}{d} + 1.444)]}, \qquad (4.1)$$

where, ϵ_i is the effective dielectric constant of metal; w is the width of a groove and d is the depth of substrate. Now, the impedance of this circuit model (Z_S)

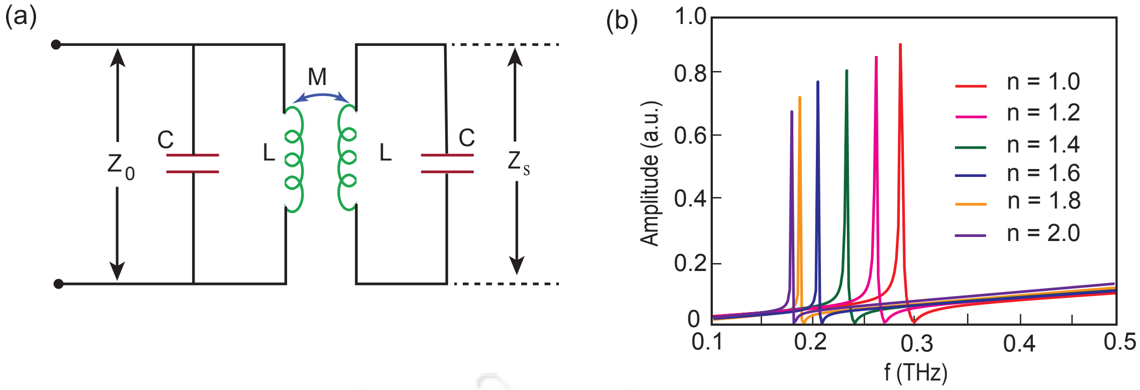

Figure 4.3: (a) Schematic of the TL-LC circuit model. The L and C in the circuit represent the inductance and capacitance, respectively. The mutual inductance of the circuit is represented by M. The Z_0 and Z_S correspond to the intrinsic impedance and circuit impedance respectively. (b) Depicts waveguide transmission from transmission line theory. Different colored traces correspond to different refractive indices i.e. 'n' = 1, 1.2, 1.4, 1.6, 1.8, and 2.

can be written as,

$$Z_S = \frac{\frac{L}{C} + \omega^2 M^2}{j[(\omega L - \frac{1}{\omega C}) - \omega M]}, \tag{4.2}$$

where, ω, L, C, and M represent angular frequency, inductance, capacitance, and mutual inductance, respectively.

The normalized transmission amplitude, $t(\omega)$ of this transmission line-LC circuit model is given by,

$$t(\omega) = \frac{2Z_S}{Z_0 + Z_S}, \tag{4.3}$$

We use Eq. (4.3) to calculate the waveguide transmission and predict varying nature of anti-resonant frequencies of the fundamental mode resulting from the polyimide of different refractive indices. The transmission results from the TL-model are shown in Fig. 4.3(b). The model enables us to predict the anti-resonant frequencies corresponding to different refractive indices (n) of polyimide for certain values of inductance, capacitance and mutual inductance which are given in Table 4.1. It may be noted that the numerically simulated waveguide transmission gives rise to broader resonance compared to the one obtained through transmission line model. The broadness of resonance in numerical simulations can be attributed to the scattering, diffraction and dispersion losses experienced by the wave as it propagates along the corrugated pattern. These losses contribute significantly to the loss of signal and hence to the broadening of spectrum. The loss due to these effects cannot be included exactly in the transmission line model. The model describes a simple yet useful semi-analytical approach to explain the resonant behavior, where focus has been primarily paid to the anti-resonance frequencies. The anti-resonance frequencies correspond to the sharp dips on the high frequency side of the each resonance. The anti-resonance dips have been shown to arise in the transmission properties of such structures because of the Fano interference phenomenon [115]. The interest in anti-resonance frequency arises because they are the relevant parameters, not the frequencies associated with the resonance peaks. This has been demonstrated through different articles in the past [44, 116, 117].

Refractive index n	L (fH)	C (pF)	M (fH)
1.0	13.4	4.18	30.1
1.2	13.4	4.98	30.5
1.4	13.4	6.35	30.5
1.6	13.4	7.95	31.5
1.8	13.4	9.55	31.55
2.0	13.4	10.47	31.55

Table 4.1: The inductance, capacitance, and mutual inductance values from the TL-LC circuit model for different refractive indices (n) of the polyimide.

4.4 Sensing characteristics of plasmonic waveguides

In order to comprehensively analyse the sensing characteristics of the proposed plasmonic waveguide, we further examine frequency shift, sensitivity and figure of merit of the fundamental mode supported by the waveguide comprising rectangular grooves. Since the shape and size of the corrugations are crucial to determine the confinement of a mode to the surface, therefore in effort to improve the sensing characteristics, we examine plasmonic waveguide comprising V-grooves of same width and depth. The sensing characteristics of V-grooves are compared to that of the rectangular grooves. The choice of V-grooves has been made as they promise strong confinement of the modes at the metal-air interface [34]. The strong confinement to the surface in highly desirable for sensing applications as the analyte at the surface extensively interacts with the wave of the order of several wavelengths.

In Fig. 4.4, we plot frequency shift of the fundamental mode versus refractive index of the polyimide filling the rectangular grooves of the plasmonic waveguide. For comparison, the frequency shift response for the same amount of analyte i.e. 0.025 mm^3 in case of V-groove is also plotted in the same figure. The blue and red traces in the figure correspond to rectangular grooves and V-grooves, respectively. We varied refractive index (n) as 1, 1.2, 1.4, 1.6, 1.8, and 2 to determine the frequency shift. As the refractive index increases, we observe a linear shift in the anti-resonant frequency of the fundamental mode. The shift is more prominent in case of V-grooves, indicating better sensing characteristics of the V-grooves compared to the rectangular grooves.

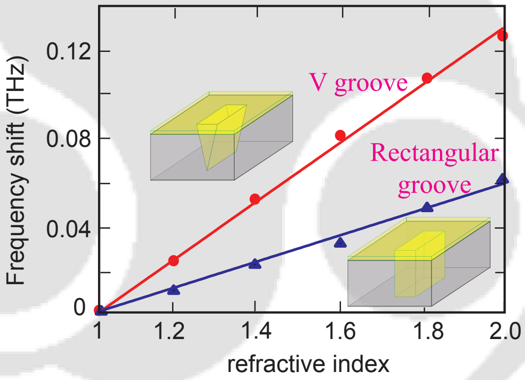

Figure 4.4: The variation of frequency shift of the fundamental mode versus refractive index of the polyimide substance for the two plasmonic terahertz waveguide. The red corresponds to the plasmonic waveguide having V-grooves, however blue line represent the case of rectangular grooves.

For comprehensive understanding of the sensing parameters, subsequently we examined sensitivities of the fundamental mode for the plasmonic waveguides with rectangular and V grooves with respect to the increasing quantity of polyimide substance. In order to do so, we varied the refractive index (n) of analyte as 1, 1.2, 1.4, 1.6, 1.8, and 2 for each of the quantity. The frequency shift i.e. $\triangle f$ is plotted versus refractive index to obtain the sensitivity of the mode corresponding to a certain quantity of analyte using $\triangle f/\triangle n$. The response of sensitivity versus analyte quantity ($\triangle V$) is plotted in Fig. 4.5(a). It may be noted that as the volume of the analyte increases, the sensitivity also monotonically increases. For the same quantity of analyte, the sensitivity is about five times higher for the V-grooves compared to the rectangular grooves. For instance, for analyte quantity, $\triangle V \simeq 0.018\ mm^3$, the sensitivity of fundamental mode in V-grooves turns out to be ≃ 0.11 THz / R.I, however it is ≃ 0.02 THz / R.I in case of rectangular grooves.

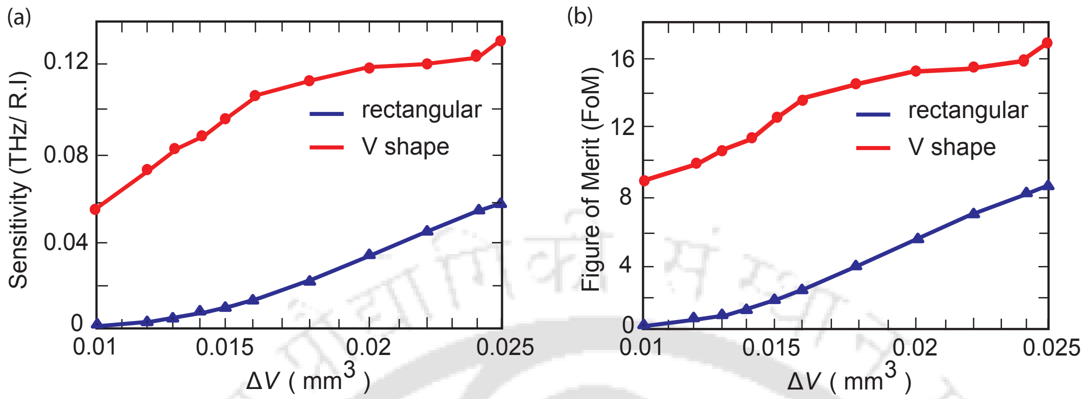

Figure 4.5: Numerically calculated sensitivity and FoM of the fundamental mode of the plasmonic waveguides having V-grooves and rectangular grooves. (a) It represents the variation of sensitivity versus quantity of the analyte filling the grooves. In (b) the variation of the Figure of Merit is plotted versus the analyte quantity. The sensitivity and the FoM values are reported to higher in case of V-grooves.

Further, we analyse the FoM of the fundamental mode of the plasmonic waveguide for different quantities of the analyte. The FoM is defined by the ratio of sensitivity and full width at half maxima (FWHM) of the plasmonic mode. In calculating FoM, we first calculated FWHMs using transmittance values of the transmission output. To compare, we find FoM results for the case of V grooves as well using the same methodology. In comparing FoM results, the analyte quantity was taken to be same for both the cases. The results are shown in Fig. 4.5(b). The FoM values increase as the analyte quantity is increased within the grooves. The FoM of the fundamental plasmonic mode is observed to be much higher in case of V-grooves as compared to the rectangular grooves. The higher values of sensitivity and FoM in case of V-grooves are believed to be due to the higher field confinement of the modes in V-grooves structures. We have examined electric field profiles of the modes in rectangular and V-grooves in Fig. 4.6(a) and (b), respectively. The field profiles are examined at the resonant frequencies of the fundamental modes i.e. at 0.30 THz for the case of rectangular grooves and 0.32 THz for V-grooves. Both the structures exhibit strong confinement of the modes to the surface of waveguide. The field confinement is higher within V-grooves which points to its better sensing characteristics. The results indicate that the sensing characteristics of a plasmonic waveguide depend upon its constituent parameters. Therefore, more extensive efforts to examine the role of planar plasmonic waveguides and their field confinement to the surface are required so that the optimized sensing characteristics of such waveguides can be achieved.

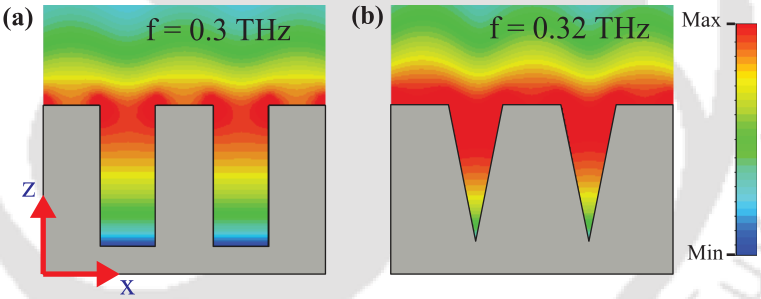

Figure 4.6: The field profiles of the fundamental THz modes in the x-z plane of the plasmonic waveguide. (a) represents field profile in the rectangular groove at resonance frequency 0.30 THz, while (b) depicts field profile at 0.32 THz which is resonant frequency of the fundamental mode in the V-grooves.

4.5 Discussions

We have examined the capability of a planar plasmonic terahertz waveguide to sense an analyte. The rectangular dimples of the waveguide are filled with a polyimide substance of varying refractive indices. We observe a linear shift in the anti-resonant frequency of the fundamental resonance mode with an increase in the refractive index of the analyte. In order to investigate sensing characteristics of the proposed waveguide, we calculated sensitivity and figure of merit of the fundamental mode with different quantities of the analyte. We found that with the increase in quantity of the analyte, both the sensitivity and FoM values increase. We employed a semi-analytical transmission line model to understand and validate numerical findings. In an effort to improve sensing capability of the plasmonic waveguide, we have examined sensing capability of the plasmonic waveguide comprising subwavelength scale V-grooves. For the same amount of analyte, we observed that the V-grooves offer better sensitivity as well as FoM as compared to the rectangular grooves because of their strong field confinement to the surface. For instance, in case of analyte quantity $\simeq 0.025\ mm^3$, the sensitivity and FoM values for the waveguide with V-grooves are found to be $\simeq$ 0.13 THz / R.I and 16.75. However, for rectangular grooves, the sensitivity and FoM turned out to be $\simeq$ 0.06 THz / R.I and 8.74 respectively. It indicates that the shape and size of the grooves and hence the electric field confinement of a mode to the surface are vital in determining the sensing capability of a plasmonic waveguide for the same quantity of material. The plasmonic waveguide based sensing could be significant in the construction of next generation high sensitive terahertz sensors.

Chapter 5

Terahertz metamaterials based thin film sensing

Contents

Metamaterials are the artificially designed material which can be used to alter the incident light at will. The metamaterials have found promising applications in diverse areas viz. medical diagnostics, food quality control, bio-sensing, detection of noxious gases, development of ultra-high speed communication devices etc [59, 78, 94, 118, 119]. There has been considerable interest in exploring metamaterials at terahertz frequencies for several interesting phenomenon and applications [55, 120–123] which include THz modulation [124, 125], polarization rotation [59], development of broadband photonic devices [82, 126], resonance bandwidth enhancement [124, 127], resonance mode hybridization [82, 126, 128–133], electromagnetic induced transparency [134], active chirality [129, 135–137], sensing

[138–141] etc. Terahertz metamaterials have also emerged as the potential candidate for thin film detection of analytes and several designs have been employed for greater sensitivity of the analytes. In this context. Singh *et al.* have reported terahertz sensing with high- quality factor resonances in metasurfaces [78]. The line widths of such resonances are extremely narrow and results in greater sensitivity of the analytes. In the context of bio-sensing, Xu *et al.* introduced gold nanoparticles into the terahertz metamaterials to improve the sensitivity of the protein detection [138]. The results indicate that the introduction of gold nanoparticles with high refractive indices result in the detection with enhanced sensitivity.

Despite several research investigations and studies, a comprehensive study of sensing capabilities of different resonance modes in terahertz metamaterials has not yet been reported in the literature. In this chapter, this aspect has been explicitly focused and the usefulness of sensing performances of the odd and even resonance orders in case of a single split gap ring resonator (relatively simple geometry) based THz metamaterials is reported. For this study, a lossless analyte of different thicknesses has been used above the metamaterial structures. The refractive index of the coated thin film is varied in order to calculate the sensitivity and figure of merit (FoM) of the different resonance modes.

In Section 5.1, the design of metamaterial structures along with numerical simulations are discussed. Terahertz transmission properties of the designed metamaterials are examined in Section 5.2 for the orthogonal polarizations of the incident terahertz i.e. parallel and perpendicular to the split gap of the SRR. In this section, sensitivity and corresponding figure of merit are calculated for different resonance modes by varying the refractive index of the analyte film for several different thicknesses. In Section 5.3, a semi-analytical transmission line (TL)-*RLC* circuit model is employed to validate and analyze numerical observations. Finally, the results are summarized and discussed in Section 5.4.

5.1 Metamaterial design and numerical simulations

The optimum design of the terahertz metamaterial (THz) is highly crucial to sense an analyte with greater sensitivity. The design consists of two dimensional array of periodically arranged single split gap ring resonator (SRR). A thin layer of analyte is coated on top of the SRR surface. Analyte is considered as coating material which is transparent to terahertz and exhibits no loss. To find out sensitivity, the thickness of the analyte is varied as d = 2, 4, 5, 6,..., 14, 15, 16,.., 20 μm. A schematic of the proposed configuration is shown in Fig. 5.1. Silicon is taken as the substrate and on its surface SRRs are periodically placed with a periodicity of 46 μm in both the x- and y - directions. The SRRs are made of gold with thickness 200 nm and outer dimensions for length and breadth as 36 μm x 36 μm. The capacitive gap (g) and line width (w) of the resonator are assumed to be of 4 μm each. The above geometrical parameters are kept constant throughout the

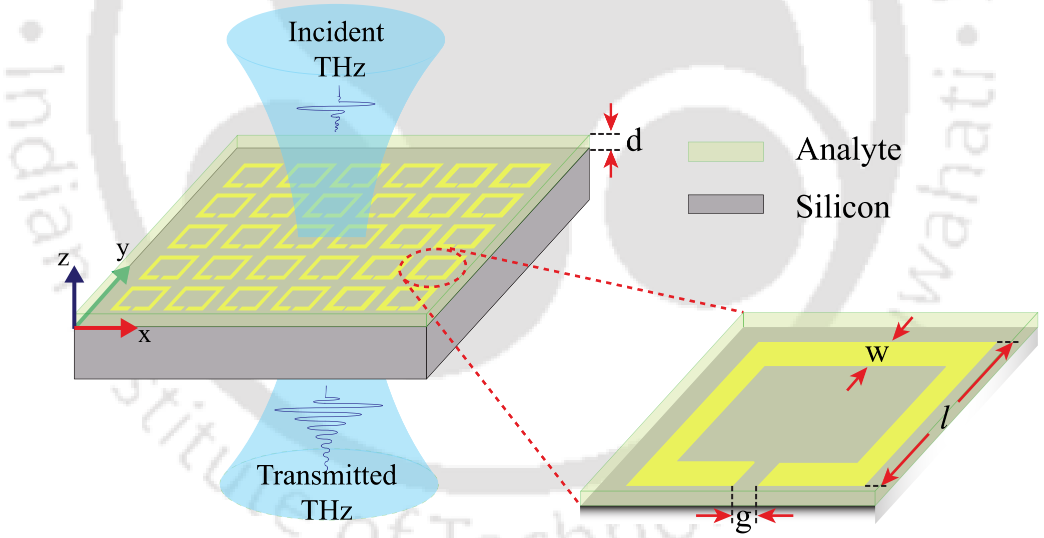

Figure 5.1: Schematic of planar Terahertz metamaterial geometry consisting of SRRs on silicon substrate. A single unit cell consists of SRR of gold metal (magnified for a closer view). The yellow region represents SRR. SRR has outer dimensions of l x l = 36 μm x 36 μm. The w and g in the schematic stand for the width and the split gap of SRR, respectively. Parameter d represents variable thickness of the analyte, which can be varied. Green colored y-axis represents polarization direction of the electric field of incident Terahertz beam.

study.

The terahertz transmission is examined through the sample for both the orthogonal polarizations. In one set of simulations, electric field polarization is assumed to be parallel to the split gap of SRR and in the other case, the polarization is taken to be perpendicular to the gap. For the case of THz polarization parallel to the gap, two resonances are found, which is termed as 1^{st} and 3^{rd} order resonances whereas in case of other polarization, a single resonance appears between the 1^{st} and 3^{rd} order resonances, which is called as the 2^{nd} order resonance [142]. For the numerical study also, commercially available numerical software, CST Microwave Studio has been used. In the numerical simulations, again tetrahedral meshing has been adopted for the configured geometry with periodic boundary conditions. The waveguide ports for the source and detector are employed. The electrical properties of the analyte and the silicon substrate in the simulations are defined with the electrical permittivities of $\epsilon = 3.5$ and $\epsilon = 11.9$, respectively. The terahertz transmission properties and corresponding sensing characteristics are discussed in the next section.

5.2 Terahertz transmission and sensing characteristics

Terahertz transmittance is examined through the designed metamaterials with and without analyte layers. A plane polarized THz radiation is incident onto the top of the metamaterial surface. The transmittance through the designed metamaterial configuration is examined for the two orthogonally polarized incident terahertz waveforms. This results in the excitation of odd and even order resonances as shown in Fig. 5.2. The results are shown in Fig. 5.2 for three different thicknesses of the analyte film. In Fig. 5.2, red traces represent the case for $d = 0$ μm i.e. when there is no analyte layer on the designed metamaterial. In this case, 1^{st},

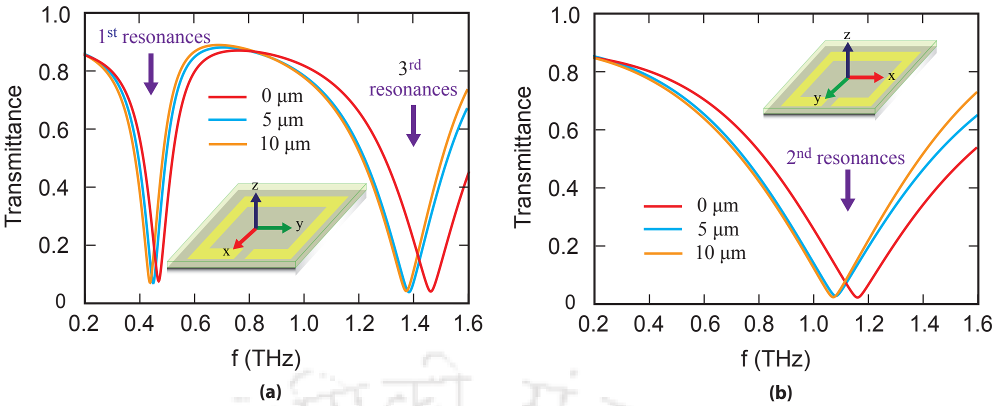

(a)

(b)

Figure 5.2: Numerically calculated THz transmittance through the metamolecule with and without the analyte as described in this work. (a) Shows transmittance for polarization parallel to split gap which yields two resonances 1^{st} and 3^{rd} order; (b) Depicts the same for polarization perpendicular to the gap, which yields 2^{nd} order resonance.

2^{nd} and 3^{rd} order resonance dips occur at 0.50 THz, 1.16 THz, and 1.47 THz, respectively. In the figures, the blue and orange color traces correspond to $d = 5$ μm and $d = 10$ μm, respectively. It may be noted that as the analyte thickness is increased, the resonance frequencies of the odd as well as even order resonance modes get red shifted by different magnitudes.

In order to comprehensively understand the reason(s) behind shift in characteristic resonance dips with variation in thickness of the analytes, THz transmission properties of the metamaterials are numerically analyzed with varying thickness of the analyte layer. The results are depicted in the form of the contour plots shown in Fig. 5.3. Fig. 5.3(a) shows the transmittance when the polarization is parallel to the split gap for different analyte thicknesses whereas, Fig. 5.3(b) shows the transmittance results when the polarization is perpendicular to the gap. In these plots, frequencies are considered ranging from 0.2 THz to 1.6 THz to accommodate the odd and even resonance modes of the designed metamaterials covered with analyte of variable thickness from $d = 0$ μm to $d = 20$ μm. The intensity of the terahertz transmission is represented by the different colors of the contour plots. The positions of the resonance dips are indicated with the dotted white color trace inside the contour plots. It is apparent from the plots that frequency shift in the resonance dip is prominent only up to about 14 μm thickness of the

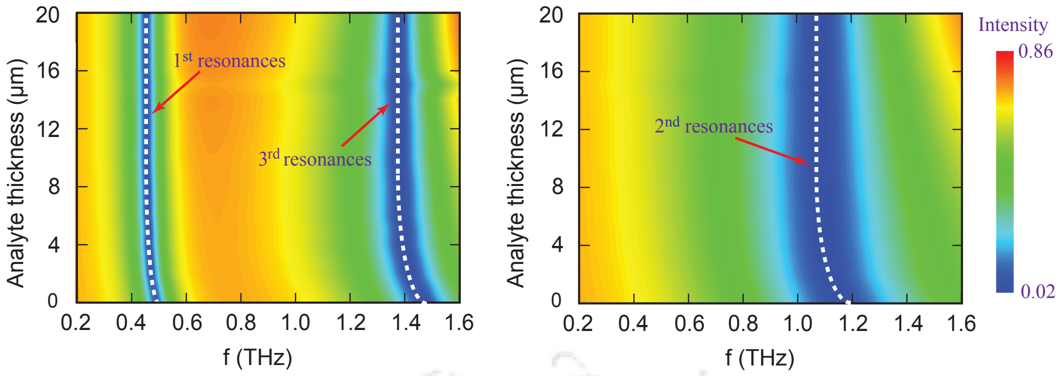

(a) (b)

Figure 5.3: Contour plot of numerically simulated THz transmittance for different analyte thicknesses. Color bar shows the magnitude of transmission intensity. (a) Represents contour plot for polarization parallel to the split gap which clearly shows two blue colored regions around white dashed line for 1^{st} and 3^{rd} order resonances, respectively; (b) Depicts the same for polarization perpendicular to split gap i.e. for 2^{nd} order resonance.

analyte layer. It may be noted that the shift of resonance frequency is predominantly caused by the change in the capacitance of different resonance modes. The size of the resonators is intentionally kept fixed, therefore the parameter affecting resonance shift is due to capacitance alone. Capacitance of the resonance is dependent on the near field distribution of the electric field lines. These field lines are highly concentrated close to the resonator and recedes away from the resonator. Beyond a certain distance (14 μm in case of our resonator) from the resonator, the electric field lines almost vanish and become insignificant. Therefore presence of any analyte beyond 14 μm (in this study) from the resonator has virtually no influence/impact on the capacitance. Hence, frequency shift saturates around 14 μm in our study. This is because of the limited spread of the electric field lines surrounding the resonator.

Further, more specifically, the shift in the resonance frequency of the odd and even order modes is examined with respect to the intrinsic resonances (i.e. without any coated layer) for different thicknesses of the coated analyte layer. The results are shown in Fig. 5.4(a). As the analyte thickness is varied, we observe a corresponding shift in the resonance frequencies for each mode. Initially, the resonance frequency shift increases monotonically with the analyte thickness, however around $d = 12\ \mu m$, it attains almost a constant value. In this figure, three different colored traces i.e. red, green and blue color represent frequency shift plots for 1^{st}, 2^{nd} and 3^{rd} order resonances, respectively. Next, the sensitivities are calculated corresponding to the odd and even order resonances. The sensitivity of the metamaterial is closely related to the refractive index or the dielectric constant of the ambient material. Sensitivities for the analyte thicknesses of d = 2, 4, 5, 6,..., 14, 15, 16,.., 20 μm have been derived. In order to find out sensitivity, the refractive index of analyte is varied as $n = 1$, 2, 3 and 4 for each of the thicknesses. As refractive index of the film changes, a distinct resonance frequency shift is achieved with respect to the resonance frequency, when there is no analyte i.e. $d = 0\ \mu m$. The refractive index versus frequency shift is plotted, which results in a linear line. The slope of this straight line indicates the sensitivity, which has the unit of THz per unit refractive index i.e. (THz / R.I.). Fig. 5.4(b) shows the plot of the calculated sensitivities for different thicknesses corresponding to 1^{st}, 2^{nd} and 3^{rd} order resonances.

Further, figure of merits (FoM) of the three resonance modes are analyzed w.r.t different thicknesses of the analyte film. FoM is defined as the ratio of sensitivity and full width at half maxima (FWHM). In calculating FoM, first FWHMs are calculated for different analyte thicknesses using transmittance values of the transmission output. Fig. 5.4(c) shows the plot of FoMs for different analyte thicknesses. In this figure, the red, green and blue colored traces represent FoM plots for 1^{st}, 2^{nd}, and 3^{rd} order resonances, respectively. One may notice that FoM increases with the increase in the analyte thickness. 1^{st} and 3^{rd} order resonances demonstrate higher FoM values compared to the 2^{nd} order resonances. So, electric field polarization parallel to the split gap is more useful as a sensing device than the polarization perpendicular to the gap. As previously stated, in our designed metamaterials, we have intentionally kept the size of the resonator is assumed to be fixed, which results in constant value of inductance. However, because of the change in coated material thickness or utilizing different refractive index materials,

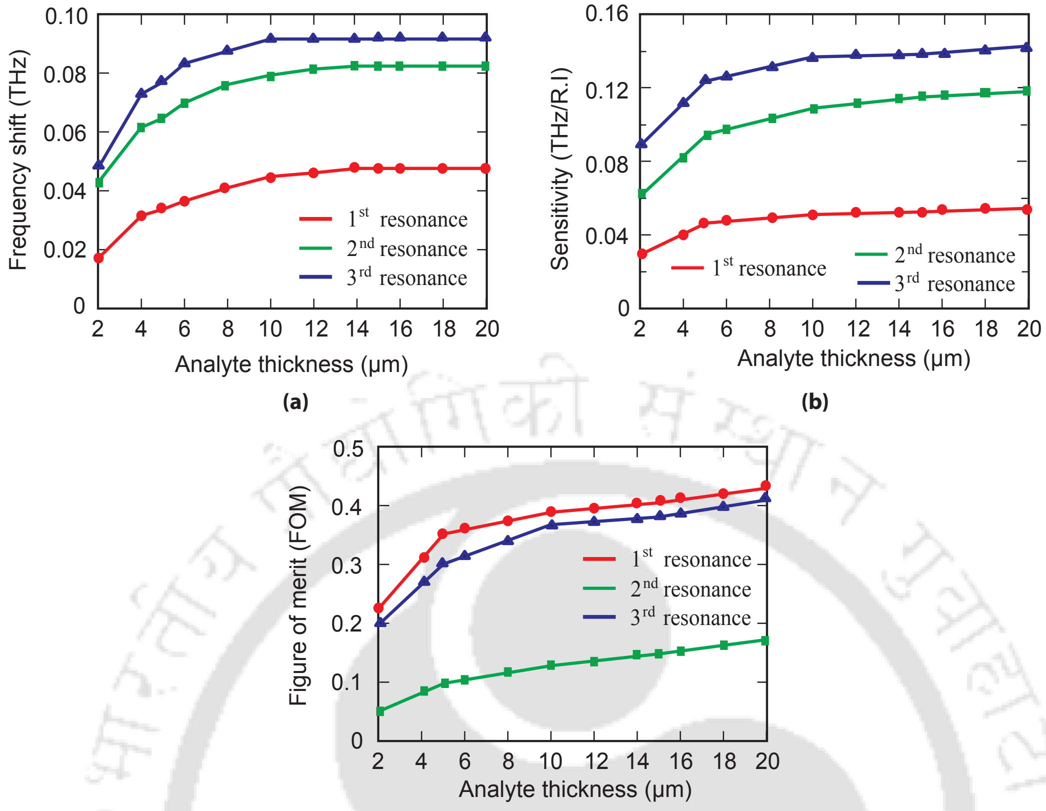

(a)

(b)

(c)

Figure 5.4: Frequency shift, sensitivity and calculated figure of merit. (a) Shows plot of frequency shift corresponding to different analyte thickness with respect to the resonance frequency when there is no analyte for three different resonances. (b) and (c) depicts the sensitivity and FoMs plots, respectively for different thicknesses corresponding to three different resonances.

the effective capacitances of the split ring resonators can change. This affects the odd order resonance modes in larger extent compared to the even order modes, hence higher values of FoM are observed in case of the odd order resonances. In order to validate the physical explanation, the electric field profiles at 1^{st}, 2^{nd} and 3^{rd} order resonances are monitored for the intrinsic MMs. The induced field distributions are shown in Fig. 5.5. The field is strongest in the split gap at 1^{st} order resonance (Fig. 5.5(a)) while at the 2^{nd} and 3^{rd} order resonant frequencies, the field is comparatively weakly confined, see Fig. 5.5(b) and (c). This clearly indicates that the effective capacitances for the odd order modes are more sensitive to the permittivity of the coated materials compared to the even order modes.

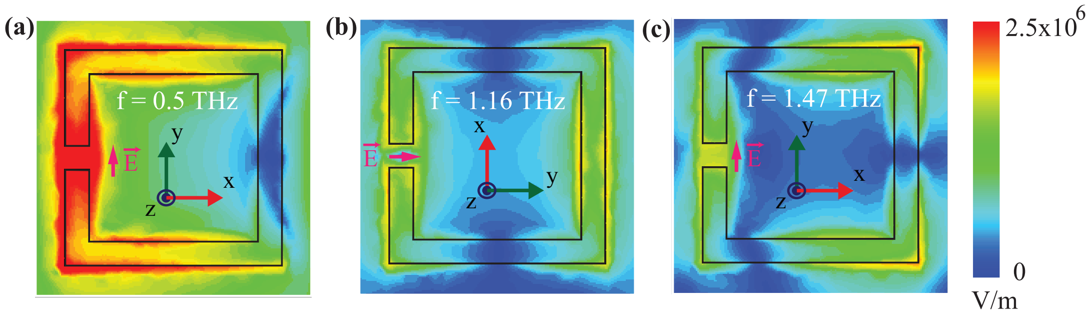

Figure 5.5: (a), (b), and (c) represents the Electric field profiles of 1^{st}, 2^{nd} and 3^{rd} resonances at 0.5 THz, 1.16 THz, and 1.47 THz, respectively. The green colored y-axis signifies the polarization direction of the incident electric filed.

5.3 Semi-analytical Transmission line model

In order to confirm resonant behavior of the designed metamaterials, a semi-analytic transmission line (TL) - RLC model is employed specific to the geometry

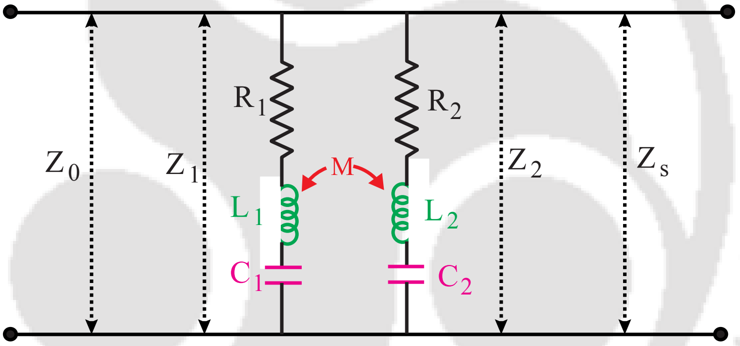

Figure 5.6: Schematic of TL-RLC circuit model. The circuit components R_1, L_1, C_1 represent resistance, inductance and capacitance related to lower order resonance and R_2, L_2, C_2 represent the same related to higher order resonance. M is the mutual inductance, responsible for coupling between resonances. Z_1 and Z_2 are impedances due to two circuits, respectively whereas Z_0 and Z_S represent impedances of free space and silicon substrate, respectively.

[90]. RLC stands for resistance, inductance, and capacitance, respectively. The circuit model of the geometry under the transmission line theory is shown in Fig. 5.6. The results of the transmittance from the model are shown in Fig. 5.7(a) and (b). Fig. 5.7(a) corresponds to 1^{st} and 3^{rd} order resonances whereas Fig. 5.7(b) corresponds to 2^{nd} order resonance. In the figure, different colored plots correspond to transmittance from the TL-RLC circuit model for different analyte thicknesses. It is noticed that they predict a similar resonant behavior and confirm the numerically simulated results for certain values of resistance, inductance,

capacitance and mutual inductance for typical SRR design. The details of the analytical transmission line model are as follows:

SRR is assumed as an equivalent RLC circuit where it is typically considered that split gap corresponds to the capacitive part, the SRR loop corresponds to the inductive part and the internal reactance of SRR is represented by the resistance part. The numerical findings show three resonances, 1^{st} and 3^{rd} order resonances together for polarization parallel to the split gap and 2^{nd} order resonance alone for polarization perpendicular to the gap. The resonant frequencies of a RLC circuit model always inversely depend on the square root of the product of inductance and capacitance. Keeping this in mind, two inductively coupled RLC circuits have been taken in parallel combination. In order to fit the 1^{st} and 3^{rd} order resonances together L_1, C_1 values are taken from 1^{st} RLC circuit, which correspond to the 1^{st} resonance and L_2, C_2 values from the 2^{nd} RLC circuit, which correspond to the 3^{rd} resonance.

These two resonances are mutually coupled through the mutual inductance M. Next, to match the 2nd order resonance with the numerical results all the circuit parameters R_1, L_1, C_1, R_2, L_2, and C_2 are adjusted with a suitable mutual inductance (M) value. From the circuit model shown in Fig. 5.6, one can calculate the circuit impedance (Z_{ct}) as,

$$Z_{ct}(\omega) = \frac{Z_1 Z_2 + \omega^2 M^2}{[Z_1 + Z_2 - 2j\omega M]}, \tag{5.1}$$

where, ω and M represent angular frequency and mutual inductance respectively. Z_1 and Z_2 correspond to the impedances due to the 1^{st} and 2^{nd} RLC circuits, respectively. These impedances can be written as:

$$Z_1 = R_1 + j(\omega L_1 - \frac{1}{\omega C_1}), \qquad Z_2 = R_2 + j(\omega L_2 - \frac{1}{\omega C_2}), \tag{5.2}$$

One can note that the circuit impedance Z_{ct} does not include the impedance due to the substrate. In Fig. 5.6, Z_0 and Z_S represent impedances of free space and silicon substrate, respectively. The values of Z_0 and Z_S are 377 Ω and 103 Ω, respectively. The overall impedance $Z(\omega)$ of the typical design including the effect of the Z_{ct} and Z_S in parallel combination can be written as

$$Z(\omega) = \frac{Z_S(Z_1 Z_2 + \omega^2 M^2)}{Z_S(Z_1 + Z_2 - 2j\omega M) + (Z_1 Z_2 + \omega^2 M^2)}, \tag{5.3}$$

The normalized transmission amplitude, $t(\omega)$ of this transmission line -*RLC* circuit model is given by,

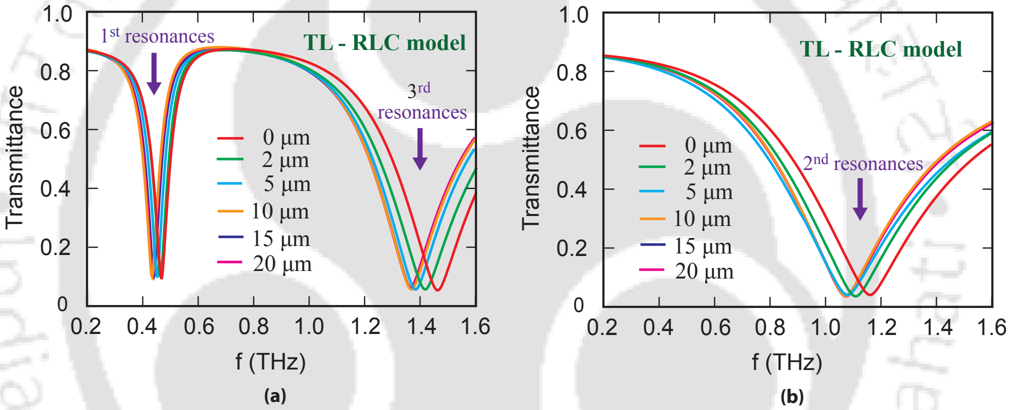

Figure 5.7: Terahertz transmittance through the typical metamaterial geometry obtained from TL-*RLC* circuit model for different thicknesses of analyte. The results are in good agreement with the numerical findings. (a) Terahertz transmittance for polarization parallel to the split gap of SRR. (b) Represents the transmittance for polarization perpendicular to the gap of SRR.

$$t(\omega) = \frac{2Z(\omega)}{Z_0 + Z(\omega)}, \tag{5.4}$$

Eq. (5.4) is used to calculate the transmittance and predict resonant frequencies due to the parallel and perpendicular polarization with the split gap for certain specific values of resistance, inductance, capacitance and mutual inductance, which are defined in Tables 5.1 and 5.2. The values of R_1, L_1, C_1, R_2, L_2, C_2, and M are obtained by fitting the transmission amplitude from the simulation using equation 5. One can notice that the calculated transmittance is in good agreement with the numerical simulations.

Thickness (μm)	R_1 (ohm)	L_1 (pH)	C_1 (fF)	R_2 (ohm)	L_2 (pH)	C_2 (fF)	M (pH)
0	10	135	0.75	8	34	0.366	-15
2	10	140	0.778	8	35	0.38	-15
5	10	141.8	0.8	8	37.1	0.37	-15
10	10	142	0.825	8	38	0.37	-15
15	10	142.2	0.83	8	38	0.37	-15
20	10	142.2	0.83	8	38	0.37	-15

Table 5.1: Resistance, inductance, capacitance, and mutual inductance for 1^{st} and 3^{rd} resonances for different thicknesses of the analyte.

Thickness (μm)	R_1 (ohm)	L_1 (pH)	C_1 (fF)	R_2 (ohm)	L_2 (pH)	C_2 (fF)	M (pH)
0	10	39.7	0.49	10	31.7	0.62	-1.5
2	10	41.9	0.5	10	33.56	0.63	-1.5
5	10	42.9	0.51	10	34.4	0.63	-1.5
10	10	43.7	0.51	10	35.7	0.63	-1.5
15	10	43.85	0.51	10	35.85	0.63	-1.5
20	10	43.85	0.51	10	35.85	0.63	-1.5

Table 5.2: Resistance, inductance, capacitance, and mutual inductance for 2^{nd} resonances for different thicknesses of the analyte.

5.4 Discussions

In this work, thin film sensing potentials of the fundamental and higher order resonant modes are analyzed for a simple metamaterials design consisting of single gap split ring resonators. Sensitivity and the corresponding figure of merit (FoM) for the different resonance modes supported by the designed metamaterials have been calculated. It is observed that the fundamental resonance mode results in the highest FoM compared to the other resonance modes. The better sensing capability to the fundamental resonance is attributed to its strong electric field confinement within the split gap. Further, it is observed that the odd order resonances act as better thin film sensors compared to the even order resonances. In order to confirm our numerical findings, a semi-analytical transmission line model is employed and found that numerical observations agree well with the theory. Because of technological ease, planar metamaterials are extremely good platform for thin film sensing including bio-sensing, temperature sensing, etc. This comprehensive study on sensing capabilities of different resonance modes in terahertz metamaterials could be significant in the construction of futuristic sensor devices. Although this work has been carried out at terahertz frequencies, this is a generic study and is applicable for other frequency domains of the electromagnetic spectrum too.

Chapter 6

Summary and direction of future work

6.1 Summary

In this thesis, we have numerically and analytically examined terahertz waveguides and sensors using plasmonic and metamaterials structures. The subwavelength scale structures are periodically arranged in a one-dimensional fashion in order to design terahertz plasmonic waveguide. The waveguide supports highly confined terahertz modes depending upon the shape and sizes of the structures. The control over the propagation properties can be significant in the construction of terahertz plasmonic devices such as sensors and modulators.

We investigated terahertz surface plasmon propagation in a plasmonic waveguide comprising of periodically designed tilted pillars. The tilting of pillars allows us to propagate terahertz modes more efficiently in a particular direction and hence control the directional properties of the modes. The propagation of guided THz modes in the waveguide was independently confirmed through a semi-analytical transmission line model. The ability to confine a THz mode of certain frequencies at a specific position along the waveguide was also analyzed by designing pillar of increasing height.

The propagation of terahertz surface plasmon mode in a plasmonic waveguide is also susceptible to the internal corrugations of the structures. By designing a plasmonic waveguide with subwavelength scale V shape structures and inducing internal corrugations in the form of step profile, one can switch multimode waveguide transmission to single mode propagation. Internal corrugations are also found to cause slow light effects in the plasmonic waveguides. As the number of corrugated steps in the structures was increased, the group velocity of the fundamental mode was found to increase. The slow-light properties of the fundamental modes are also investigated in waveguides comprising of gradually increasing the depth of internally corrugated structures. The transmission response of waveguide was analyzed and confirmed by a transmission line RLC circuit model.

Planar plasmonic terahertz waveguides exhibit strong field confinement of the modes, which could be significant to several applications including sensors. We have investigated the capabilities of plasmonic waveguides as thin film terahertz sensors. We designed a plasmonic waveguide comprising of rectangular grooves and examined various sensing parameters such as frequency shift, sensitivity, and figure of merit of the fundamental mode supported by the waveguide by filling grooves with analytes of different refractive indices. In order to improve sensing characteristics of the plasmonic waveguide, we also examined V-groove structures and compared results with that of rectangular grooves. The V-groove structures offered better sensing characteristic because of strong electric field confinement of the modes along the corrugated pattern.

In terahertz metamaterials, we investigated the role of resonances supported by planar terahertz metamaterials in sensing analytes. Planar terahertz metamaterial configuration is examined with orthogonal polarizations of the incident terahertz in order to excite fundamental and higher modes. Various sensing parameters viz. frequency shift, sensitivity, and figure of merit are calculated for different resonant modes due to orthogonal polarizations of electric field vector. The fundamental resonance is found to exhibit better sensing characteristics because of its strongest electric field confinement within the split gap. Further, it is observed that the odd order resonances act as better thin film sensors compared to the even order resonances. In order to confirm our numerical findings, we employed a semi-analytical transmission line model and found that numerical observations agree well with the theory.

6.2 Future work

The study of plasmonic and metamaterials structures reported in this thesis can be used to investigate several important applications and build devices in the terahertz domain. In our plasmonic waveguides, we have not focused on the overall loss and confinement characteristics, which are highly important for the efficient waveguide system. In future work, we will analyze loss and degree of confinement of the modes in plasmonic waveguides w.r.t different shapes and sizes of the plasmonic structures. The plasmonic structures will be optimized to achieve low loss and highest possible confinement of the modes. We are planning to fabricate the optimized waveguide geometries using photolithography technique. The fabricated waveguide geometries will be experimentally characterized using the modified technique of THz-time domain spectroscopy techniques, discussed in Chapter 1.

We are planning to explore plasmon induced transparency (PIT) using the plasmonic metamaterial structures in the waveguide configuration. Zhang *et al.* [143] have reported plasmonic induced transparency in plasmonic metamaterials in the transmission configuration. The proposed plasmonic waveguides can be used to demonstrate this effect more prominently because of the longer interaction of the incident radiations with the plasmonic structures. In order to demonstrate PIT effect in waveguide configuration, we will study different plasmonic structures for their ability to exhibit dark and bright plasmonic modes having nearly same resonance frequencies. The destructive interference effect will be analyzed at the other end of the waveguide to demonstrate PIT effect.

In our work on plasmonic waveguide based thin film sensor, we have investigated sensing characteristics of the fundamental plasmonic mode. However, plasmonic waveguides have been found to exhibit higher order resonances as well [43, 44]. In this context, Zhu *et al.* have shown that three resonance modes can be propagated simultaneously along the waveguide by properly designed plasmonic structures. The higher order modes can be equally important to the sensor applications. In future work, we will investigate the role of higher order resonance and examine their sensing characteristics. These waveguides will also be fabricated using suitable fabrication techniques and their sensing capability will be experimentally examined using THz-TDS.

In terahertz metamaterials, the present study could be extended to the design of asymmetric metamaterial structures. Certain asymmetric metamaterial structures can selectively excite high quality factor dark modes. In future, we plan to explore the sensing capabilities of these modes and explore the possibility to improve sensing characteristics of the planar metamaterial structures.

Bibliography

[1] Xi-Cheng Zhang and Jingzhou Xu. *Introduction to THz wave photonics*, volume 29. Springer, 2010.

[2] Chuji Wang and Peeyush Sahay. Breath analysis using laser spectroscopic techniques: breath biomarkers, spectral fingerprints, and detection limits. *Sensors*, 9(10):8230–8262, 2009.

[3] Hai-Bo Liu, Hua Zhong, Nicholas Karpowicz, Yunqing Chen, and Xi-Cheng Zhang. Terahertz spectroscopy and imaging for defense and security applications. *Proceedings of the IEEE*, 95(8):1514–1527, 2007.

[4] Shuchang Liu, Oleg Mitrofanov, and Ajay Nahata. Near-field terahertz imaging using sub-wavelength apertures without cutoff. *Optics express*, 24(3): 2728–2736, 2016.

[5] Hai-Bo Liu, Yunqing Chen, Glenn J Bastiaans, and X-C Zhang. Detection and identification of explosive rdx by thz diffuse reflection spectroscopy. *Optics Express*, 14(1):415–423, 2006.

[6] T Globus, D Woolard, M Bykhovskaia, B Gelmont, L Werbos, and A Samuels. Thz-frequency spectroscopic sensing of dna and related biological materials. *International Journal of High Speed Electronics and Systems*, 13(04):903–936, 2003.

[7] Ajay Nahata, Aniruddha S Weling, and Tony F Heinz. A wideband coherent terahertz spectroscopy system using optical rectification and electro-optic sampling. *Applied physics letters*, 69(16):2321–2323, 1996.

[8] DJ Cook and RM Hochstrasser. Intense terahertz pulses by four-wave rectification in air. *Optics letters*, 25(16):1210–1212, 2000.

[9] VM Agranovich, YR Shen, RH Baughman, and AA Zakhidov. Linear and nonlinear wave propagation in negative refraction metamaterials. *Physical Review B*, 69(16):165112, 2004.

[10] Mark E Barnes, Sam A Berry, P Gow, Duncan McBryde, Geoff J Daniell, Harvey E Beere, David A Ritchie, and Vasilis Apostolopoulos. Investigation of the role of the lateral photo-dember effect in the generation of terahertz radiation using a metallic mask on a semiconductor. *Optics express*, 21(14): 16263–16272, 2013.

[11] Q Wu, TD Hewitt, and X-C Zhang. Two-dimensional electro-optic imaging of thz beams. *Applied Physics Letters*, 69(8):1026–1028, 1996.

[12] E Budiarto, J Margolies, S Jeong, J Son, and J Bokor. High-intensity terahertz pulses at 1-khz repetition rate. *IEEE Journal of Quantum Electronics*, 32(10):1839–1846, 1996.

[13] Nobuhiko Sarukura, Hideyuki Ohtake, Shinji Izumida, and Zhenlin Liu. High average-power thz radiation from femtosecond laser-irradiated inas in a magnetic field and its elliptical polarization characteristics. *Journal of applied physics*, 84(1):654–656, 1998.

[14] RW McGowan, G Gallot, and D Grischkowsky. Propagation of ultrawideband short pulses of terahertz radiation through submillimeter-diameter circular waveguides. *Optics letters*, 24(20):1431–1433, 1999.

[15] Rajind Mendis and Daniel Grischkowsky. Undistorted guided-wave propagation of subpicosecond terahertz pulses. *Optics letters*, 26(11):846–848, 2001.

[16] Hua Cao and Ajay Nahata. Coupling of terahertz pulses onto a single metal wire waveguide using milled grooves. *Optics express*, 13(18):7028–7034, 2005.

[17] Yuguang Zhao and Daniel R Grischkowsky. 2-d terahertz metallic photonic crystals in parallel-plate waveguides. *IEEE transactions on Microwave Theory and Techniques*, 55(4):656–663, 2007.

[18] Daru Chen and Haibin Chen. A novel low-loss terahertz waveguide: Polymer tube. *Optics express*, 18(4):3762–3767, 2010.

[19] Alexandre Dupuis, Karen Stoeffler, Bora Ung, Charles Dubois, and Maksim Skorobogatiy. Transmission measurements of hollow-core thz bragg fibers. *JOSA B*, 28(4):896–907, 2011.

[20] Oleg Mitrofanov, Richard James, F Aníbal Fernández, Themistoklis K Mavrogordatos, and James A Harrington. Reducing transmission losses in hollow thz waveguides. *IEEE Transactions on Terahertz Science and Technology*, 1(1):124–132, 2011.

[21] Tian Ma, Hichem Guerboukha, Martin Girard, Andrew D Squires, Roger A Lewis, and Maksim Skorobogatiy. 3d printed hollow-core terahertz optical waveguides with hyperuniform disordered dielectric reflectors. *Advanced Optical Materials*, 4(12):2085–2094, 2016.

[22] Haisu Li, Shaghik Atakaramians, Richard Lwin, Xiaoli Tang, Zhuzheng Yu, Alexander Argyros, and Boris T Kuhlmey. Flexible single-mode hollow-core terahertz fiber with metamaterial cladding. *Optica*, 3(9):941–947, 2016.

[23] Ajanta Barh, Ravi K Varshney, Bishnu P Pal, GP Agrawal, and BMA Rahman. Design of a polymer-based hollow-core bandgap fiber for low-loss ter-

ahertz transmission. *IEEE Photonics Technology Letters*, 28(15):1703–1706, 2016.

[24] SP Jamison, RW McGowan, and D Grischkowsky. Single-mode waveguide propagation and reshaping of sub-ps terahertz pulses in sapphire fibers. *Applied physics letters*, 76(15):1987–1989, 2000.

[25] Alireza Hassani, Alexandre Dupuis, and Maksim Skorobogatiy. Low loss porous terahertz fibers containing multiple subwavelength holes. *Applied Physics Letters*, 92(7):071101, 2008.

[26] Shaghik Atakaramians, Shahraam Afshar, Bernd M Fischer, Derek Abbott, and Tanya M Monro. Porous fibers: a novel approach to low loss thz waveguides. *Optics Express*, 16(12):8845–8854, 2008.

[27] G Gallot, SP Jamison, RW McGowan, and D Grischkowsky. Terahertz waveguides. *JOSA B*, 17(5):851–863, 2000.

[28] Markus Wächter, Michael Nagel, and Heinrich Kurz. Metallic slit waveguide for dispersion-free low-loss terahertz signal transmission. *Applied Physics Letters*, 90(6):061111, 2007.

[29] Adam L Bingham and Daniel R Grischkowsky. Terahertz 2-d photonic crystal waveguides. *IEEE Microwave and Wireless Components Letters*, 18(7): 428–430, 2008.

[30] Zhangjian Li, Yao Zhang, and Baojun Li. Terahertz photonic crystal switch in silicon based on self-imaging principle. *Optics express*, 14(9):3887–3892, 2006.

[31] Jiusheng Li, Jinlong He, and Zhi Hong. Terahertz wave switch based on silicon photonic crystals. *Applied optics*, 46(22):5034–5037, 2007.

[32] Kazuisao Tsuruda, Masayuki Fujita, and Tadao Nagatsuma. Extremely low-loss terahertz waveguide based on silicon photonic-crystal slab. *Optics express*, 23(25):31977–31990, 2015.

[33] Gagan Kumar, Shanshan Li, Mohammad M Jadidi, and Thomas E Murphy. Terahertz surface plasmon waveguide based on a one-dimensional array of silicon pillars. *New Journal of Physics*, 15(8):085031, 2013.

[34] Shanshan Li, Mohammad M Jadidi, Thomas E Murphy, and Gagan Kumar. Terahertz surface plasmon polaritons on a semiconductor surface structured with periodic v-grooves. *Optics express*, 21(6):7041–7049, 2013.

[35] Shanshan Li, Mohammad M Jadidi, Thomas E Murphy, and Gagan Kumar. Plasmonic terahertz waveguide based on anisotropically etched silicon substrate. *IEEE Transactions on Terahertz Science and Technology*, 4(4): 454–458, 2014.

[36] Gagan Kumar and VK Tripathi. Anomalous absorption of surface plasma wave by particles adsorbed on metal surface. *Applied Physics Letters*, 91 (16):161503, 2007.

[37] JB Pendry, L Martin-Moreno, and FJ Garcia-Vidal. Mimicking surface plasmons with structured surfaces. *Science*, 305(5685):847–848, 2004.

[38] Qiaoqiang Gan, Zhan Fu, Yujie J Ding, and Filbert J Bartoli. Ultrawide-bandwidth slow-light system based on thz plasmonic graded metallic grating structures. *Physical review letters*, 100(25):256803, 2008.

[39] Thomas Kleine-Ostmann and Tadao Nagatsuma. A review on terahertz communications research. *Journal of Infrared, Millimeter, and Terahertz Waves*, 32(2):143–171, 2011.

[40] Shichao Song, Fuhe Sun, Qin Chen, and Yaxin Zhang. Narrow-linewidth and

high-transmission terahertz bandpass filtering by metallic gratings. *IEEE Transactions on Terahertz Science and Technology*, 5(1):131–136, 2015.

[41] Jin Tao, Bin Hu, Xiao Yong He, and Qi Jie Wang. Tunable subwavelength terahertz plasmonic stub waveguide filters. *IEEE Transactions on Nanotechnology*, 12(6):1191–1197, 2013.

[42] Christopher R Williams, Steven R Andrews, SA Maier, AI Fernandez-Dominguez, L Martín-Moreno, and FJ Garcia-Vidal. Highly confined guiding of terahertz surface plasmon polaritons on structured metal surfaces. *Nature Photonics*, 2(3):175–179, 2008.

[43] Wenqi Zhu, Amit Agrawal, and Ajay Nahata. Planar plasmonic terahertz guided-wave devices. *Optics express*, 16(9):6216–6226, 2008.

[44] Gagan Kumar, Albert Cui, Shashank Pandey, and Ajay Nahata. Planar terahertz waveguides based on complementary split ring resonators. *Optics express*, 19(2):1072–1080, 2011.

[45] Shashank Pandey, Barun Gupta, and Ajay Nahata. Terahertz plasmonic waveguides created via 3d printing. *Optics express*, 21(21):24422–24430, 2013.

[46] Shashank Pandey, Barun Gupta, Ashish Chanana, and Ajay Nahata. Non-drude like behaviour of metals in the terahertz spectral range. *Advances in Physics: X*, pages 1–18, 2016.

[47] Binbin Hong, Nutapong Somjit, John Cunningham, and Ian Robertson. Design study of low loss single-mode hollow core photonic crystal terahertz waveguide with support bridges. In *2015 40th International Conference on Infrared, Millimeter, and Terahertz waves (IRMMW-THz)*, pages 1–2. IEEE, 2015.

[48] Felipe A Vallejo and L Michael Hayden. Design of ultra-broadband terahertz polymer waveguide emitters for telecom wavelengths using coupled mode theory. *Optics express*, 21(5):5842–5858, 2013.

[49] JJ Wood, LA Tomlinson, O Hess, SA Maier, and AI Fernández-Domínguez. Spoof plasmon polaritons in slanted geometries. *Physical Review B*, 85(7): 075441, 2012.

[50] Anastasia Rusina, Maxim Durach, Keith A Nelson, and Mark I Stockman. Nanoconcentration of terahertz radiation in plasmonic waveguides. *Optics express*, 16(23):18576–18589, 2008.

[51] Borwen You, Ja-Yu Lu, Tze-An Liu, and Jin-Long Peng. Hybrid terahertz plasmonic waveguide for sensing applications. *Optics express*, 21(18):21087–21096, 2013.

[52] Masaya Nagai, Noriyuki Mukai, Yosuke Minowa, Masaaki Ashida, Takehito Suzuki, Jun Takayanagi, and Hideyuki Ohtake. Achromatic wave plate in thz frequency region based on parallel metal plate waveguides with a pillar array. *Optics express*, 23(4):4641–4649, 2015.

[53] Martin Mittendorff, Shanshan Li, and Thomas E Murphy. Graphene-based waveguide-integrated terahertz modulator. *ACS Photonics*, 4(2):316–321, 2017.

[54] Rajind Mendis, Abhishek Nag, Frank Chen, and Daniel M Mittleman. A tunable universal terahertz filter using artificial dielectrics based on parallel-plate waveguides. *Applied physics letters*, 97(13):131106, 2010.

[55] Hou-Tong Chen, John F O'Hara, Abul K Azad, David Shrekenhamer, Willie Padilla, Joshua M Zide, Arthur Gossard, Richard D Averitt, and Antoinette J Taylor. Active terahertz metamaterial devices. In *Plasmonics and Metamaterials*, page MMD5. Optical Society of America, 2008.

[56] Abul K Azad, Antoinette J Taylor, Evgenya Smirnova, and John F O'Hara. Characterization and analysis of terahertz metamaterials based on rectangular split-ring resonators. *Applied Physics Letters*, 92(1):011119, 2008.

[57] Zoran Jakšić, Slobodan Vuković, Jovan Matovic, and Dragan Tanasković. Negative refractive index metasurfaces for enhanced biosensing. *Materials*, 4(1):1–36, 2010.

[58] Riccardo Degl'Innocenti, David S Jessop, Yash D Shah, Juraj Sibik, J Axel Zeitler, Piran R Kidambi, Stephan Hofmann, Harvey E Beere, and David A Ritchie. Low-bias terahertz amplitude modulator based on split-ring resonators and graphene. *ACS nano*, 8(3):2548–2554, 2014.

[59] Nathaniel K Grady, Jane E Heyes, Dibakar Roy Chowdhury, Yong Zeng, Matthew T Reiten, Abul K Azad, Antoinette J Taylor, Diego AR Dalvit, and Hou-Tong Chen. Terahertz metamaterials for linear polarization conversion and anomalous refraction. *Science*, page 1235399, 2013.

[60] JB Pendry, AJ Holden, DJ Robbins, and WJ Stewart. Low frequency plasmons in thin-wire structures. *Journal of Physics: Condensed Matter*, 10 (22):4785, 1998.

[61] Constantin R Simovski, Pavel A Belov, Alexander V Atrashchenko, and Yuri S Kivshar. Wire metamaterials: physics and applications. *Advanced Materials*, 24(31):4229–4248, 2012.

[62] Fuli Zhang, Weihong Zhang, Qian Zhao, Jingbo Sun, Kepeng Qiu, Ji Zhou, and Didier Lippens. Electrically controllable fishnet metamaterial based on nematic liquid crystal. *Optics express*, 19(2):1563–1568, 2011.

[63] D Yu Shchegolkov, AK Azad, JF O'hara, and EI Simakov. Perfect subwavelength fishnetlike metamaterial-based film terahertz absorbers. *Physical Review B*, 82(20):205117, 2010.

[64] Zeyong Wei, Yang Cao, Jin Han, Chao Wu, Yuancheng Fan, and Hongqiang Li. Broadband negative refraction in stacked fishnet metamaterial. *Applied Physics Letters*, 97(14):141901, 2010.

[65] IE Khodasevych, Charan M Shah, Sharath Sriram, Madhu Bhaskaran, W Withayachumnankul, BSY Ung, Hungyen Lin, WST Rowe, Derek Abbott, and A Mitchell. Elastomeric silicone substrates for terahertz fishnet metamaterials. *Applied Physics Letters*, 100(6):061101, 2012.

[66] John B Pendry, A J_ Holden, DJ Robbins, and WJ Stewart. Magnetism from conductors and enhanced nonlinear phenomena. *IEEE transactions on microwave theory and techniques*, 47(11):2075–2084, 1999.

[67] Richard A Shelby, David R Smith, and Seldon Schultz. Experimental verification of a negative index of refraction. *science*, 292(5514):77–79, 2001.

[68] Dongmin Wu, Nicholas Fang, Cheng Sun, Xiang Zhang, Willie J Padilla, Dimitri N Basov, David R Smith, and Sheldon Schultz. Terahertz plasmonic high pass filter. *Applied Physics Letters*, 83(1):201–203, 2003.

[69] Zhi Hao Jiang, Lan Lin, Ding Ma, Seokho Yun, Douglas H Werner, Zhiwen Liu, and Theresa S Mayer. Broadband and wide field-of-view plasmonic metasurface-enabled waveplates. *Scientific reports*, 4:7511, 2014.

[70] Juan Domingo Baena, Jordi Bonache, Ferran Martin, R Marqués Sillero, Francisco Falcone, Txema Lopetegi, Miguel AG Laso, Joan Garcia-Garcia, Ignacio Gil, M Flores Portillo, et al. Equivalent-circuit models for split-ring resonators and complementary split-ring resonators coupled to planar transmission lines. *IEEE transactions on microwave theory and techniques*, 53(4):1451–1461, 2005.

[71] T Kaelberer, VA Fedotov, N Papasimakis, DP Tsai, and NI Zheludev.

Toroidal dipolar response in a metamaterial. *Science*, 330(6010):1510–1512, 2010.

[72] K Marinov, AD Boardman, VA Fedotov, and N Zheludev. Toroidal metamaterial. *New Journal of Physics*, 9(9):324, 2007.

[73] Zhaofeng Li, Rongkuo Zhao, Thomas Koschny, Maria Kafesaki, Kamil Boratay Alici, Evrim Colak, Humeyra Caglayan, Ekmel Ozbay, and CM Soukoulis. Chiral metamaterials with negative refractive index based on four "u" split ring resonators. *Applied Physics Letters*, 97(8):081901, 2010.

[74] Shuang Zhang, Yong-Shik Park, Jensen Li, Xinchao Lu, Weili Zhang, and Xiang Zhang. Negative refractive index in chiral metamaterials. *Physical review letters*, 102(2):023901, 2009.

[75] Hai Zhu, Fei Yi, and Ertugrul Cubukcu. Plasmonic metamaterial absorber for broadband manipulation of mechanical resonances. *Nature Photonics*, 10(11):709–714, 2016.

[76] Dang Hong Luu, Nguyen Van Dung, Pham Hai, Trinh Thi Giang, and Vu Dinh Lam. Switchable and tunable metamaterial absorber in thz frequencies. *Journal of Science: Advanced Materials and Devices*, 1(1):65–68, 2016.

[77] Qinfei Zhang, Qixiang Ma, Shitao Yan, Fengmin Wu, Xunjun He, and Jiuxing Jiang. Tunable terahertz absorption in graphene-based metamaterial. *Optics Communications*, 353:70–75, 2015.

[78] Ranjan Singh, Wei Cao, Ibraheem Al-Naib, Longqing Cong, Withawat Withayachumnankul, and Weili Zhang. Ultrasensitive terahertz sensing with high-q fano resonances in metasurfaces. *Applied Physics Letters*, 105(17):171101, 2014.

[79] Justyna K Gansel, Michael Latzel, Andreas Frölich, Johannes Kaschke, Michael Thiel, and Martin Wegener. Tapered gold-helix metamaterials as improved circular polarizers. *Applied Physics Letters*, 100(10):101109, 2012.

[80] Hu Tao, AC Strikwerda, K Fan, WJ Padilla, X Zhang, and RD Averitt. Reconfigurable terahertz metamaterials. *Physical Review Letters*, 103(14): 147401, 2009.

[81] Jianqiang Gu, Ranjan Singh, Xiaojun Liu, Xueqian Zhang, Yingfang Ma, Shuang Zhang, Stefan A Maier, Zhen Tian, Abul K Azad, Hou-Tong Chen, et al. Active control of electromagnetically induced transparency analogue in terahertz metamaterials. *Nat. Commun.*, 3(1151), 2012.

[82] Dibakar Roy Chowdhury, Ranjan Singh, Antoinette J Taylor, Hou-Tong Chen, and Abul K Azad. Ultrafast manipulation of near field coupling between bright and dark modes in terahertz metamaterial. *Applied Physics Letters*, 102(1):011122, 2013.

[83] Ranjan Singh, Jie Xiong, Abul K Azad, Hao Yang, Stuart A Trugman, QX Jia, Antoinette J Taylor, and Hou-Tong Chen. Optical tuning and ultrafast dynamics of high-temperature superconducting terahertz metamaterials. *Nanophotonics*, 1(1):117–123, 2012.

[84] John F O'Hara, Ranjan Singh, Igal Brener, Evgenya Smirnova, Jiaguang Han, Antoinette J Taylor, and Weili Zhang. Thin-film sensing with planar terahertz metamaterials: sensitivity and limitations. *Optics Express*, 16(3): 1786–1795, 2008.

[85] Hu Tao, Andrew C Strikwerda, Mengkun Liu, Jessica P Mondia, Evren Ekmekci, Kebin Fan, David L Kaplan, Willie J Padilla, Xin Zhang, Richard D Averitt, et al. Performance enhancement of terahertz metamaterials on ultrathin substrates for sensing applications. *Applied Physics Letters*, 97(26): 261909, 2010.

[86] Withawat Withayachumnankul, Hungyen Lin, Kazunori Serita, Charan M Shah, Sharath Sriram, Madhu Bhaskaran, Masayoshi Tonouchi, Christophe Fumeaux, and Derek Abbott. Sub-diffraction thin-film sensing with planar terahertz metamaterials. *Optics express*, 20(3):3345–3352, 2012.

[87] Manoj Gupta, Yogesh Kumar Srivastava, Manukumara Manjappa, and Ranjan Singh. Sensing with toroidal metamaterial. *Applied Physics Letters*, 110 (12):121108, 2017.

[88] P Gaal, MB Raschke, K Reimann, and M Woerner. Measuring optical frequencies in the 0–40 thz range with non-synchronized electro–optic sampling. *Nature Photonics*, 1(10):577–580, 2007.

[89] David M Pozar. *Microwave engineering*. John Wiley & Sons, 2009.

[90] John F O'Hara, Evgenya Smirnova, Abul K Azad, Hou-Tong Chen, and Antoinette J Taylor. Effects of microstructure variations on macroscopic terahertz metafilm properties. *Active and Passive Electronic Components*, 2007, 2007.

[91] S Koenig, D Lopez-Diaz, J Antes, F Boes, R Henneberger, A Leuther, A Tessmann, R Schmogrow, D Hillerkuss, R Palmer, et al. Wireless sub-thz communication system with high data rate. *Nature Photonics*, 7(12): 977–981, 2013.

[92] C Haffner, W Heni, Y Fedoryshyn, J Niegemann, A Melikyan, DL Elder, B Baeuerle, Y Salamin, A Josten, U Koch, et al. All-plasmonic mach–zehnder modulator enabling optical high-speed communication at the microscale. *Nature Photonics*, 9(8):525–528, 2015.

[93] Harri Holma and Antti Toskala. *HSDPA/HSUPA for UMTS: high speed radio access for mobile communications*. John Wiley & Sons, 2007.

[94] Wojciech Knap, S Rumyantsev, MS Vitiello, Dominique Coquillat, S Blin, N Dyakonova, M Shur, Frederic Teppe, A Tredicucci, and T Nagatsuma. Nanometer size field effect transistors for terahertz detectors. *Nanotechnology*, 24(21):214002, 2013.

[95] Dainan Zhang, Dandan Sun, Qiye Wen, Tianlong Wen, James Kolodzey, and Huaiwu Zhang. Tuning the optical modulation of wideband terahertz waves by the gate voltage of graphene field effect transistors. *Composites Part B: Engineering*, 89:54–59, 2016.

[96] Xiaopeng Shen and Tie Jun Cui. Planar plasmonic metamaterial on a thin film with nearly zero thickness. *Applied Physics Letters*, 102(21):211909, 2013.

[97] Manjakavahoaka Razanoelina, Filchito R Bagsican, Iwao Kawayama, Xiang Zhang, Lulu Ma, Hironaru Murakami, Robert Vajtai, Pulickel M Ajayan, Junichiro Kono, Daniel M Mittleman, et al. Parallel plate waveguide time domain spectroscopy to study terahertz conductivity of utltrathin materials. In *SPIE Commercial+ Scientific Sensing and Imaging*, pages 985604–985604. International Society for Optics and Photonics, 2016.

[98] Robert W McKinney, Yasuaki Monnai, Rajind Mendis, and Daniel Mittleman. Focused terahertz waves generated by a phase velocity gradient in a parallel-plate waveguide. *Optics express*, 23(21):27947–27952, 2015.

[99] Dominik Walter Vogt and Rainer Leonhardt. 3d-printed broadband dielectric tube terahertz waveguide with anti-reflection structure. *Journal of Infrared, Millimeter, and Terahertz Waves*, pages 1–10, 2016.

[100] Michael Nagel, Astrid Marchewka, and Heinrich Kurz. Low-index discontinuity terahertz waveguides. *Optics express*, 14(21):9944–9954, 2006.

[101] Diego Martin-Cano, O Quevedo-Teruel, Esteban Moreno, L Martin-Moreno,

and FJ Garcia-Vidal. Waveguided spoof surface plasmons with deep-subwavelength lateral confinement. *Optics letters*, 36(23):4635–4637, 2011.

[102] Vyacheslav A Trofimov, Svetlana A Varentsova, and Vladislav V Trofimov. Possibility of the detection and identification of substance at long distance using the noisy reflected thz pulse under real conditions. In *SPIE Sensing Technology+ Applications*, pages 94830P–94830P. International Society for Optics and Photonics, 2015.

[103] Chong Han, A Ozan Bicen, and Ian F Akyildiz. Multi-ray channel modeling and wideband characterization for wireless communications in the terahertz band. *IEEE Transactions on Wireless Communications*, 14(5):2402–2412, 2015.

[104] Yin Huang, Changjun Min, Pouya Dastmalchi, and Georgios Veronis. Slow-light enhanced subwavelength plasmonic waveguide refractive index sensors. *Optics express*, 23(11):14922–14936, 2015.

[105] Yin Huang, Changjun Min, and Georgios Veronis. Subwavelength slow-light waveguides based on a plasmonic analogue of electromagnetically induced transparency. *Applied Physics Letters*, 99(14):143117, 2011.

[106] Guoxi Wang, Hua Lu, and Xueming Liu. Dispersionless slow light in mim waveguide based on a plasmonic analogue of electromagnetically induced transparency. *Optics express*, 20(19):20902–20907, 2012.

[107] Toshihiko Baba. Slow light in photonic crystals. *Nature photonics*, 2(8): 465–473, 2008.

[108] Lingxuan Zhang, Xiaoyuan Lu, Yongkang Gong, Nigel Copner, Wei Zhao, Guoxi Wang, and Wenfu Zhang. Low-loss slow-light in periodic plasmonic waveguides. *IEEE Photonics Technology Letters*, 27(11):1208–1211, 2015.

[109] Manukumara Manjappa, Sher-Yi Chiam, Longqing Cong, Andrew A Bettiol, Weili Zhang, and Ranjan Singh. Tailoring the slow light behavior in terahertz metasurfaces. *Applied Physics Letters*, 106(18):181101, 2015.

[110] Kun Zhang, Cheng Wang, Ling Qin, Ru-Wen Peng, Di-Hu Xu, Xiang Xiong, and Mu Wang. Dual-mode electromagnetically induced transparency and slow light in a terahertz metamaterial. *Optics letters*, 39(12):3539–3542, 2014.

[111] A Keshavarz and A Zakery. A novel terahertz semiconductor metamaterial for slow light device and dual-band modulator applications. *Plasmonics*, pages 1–8, 2017.

[112] Jiangquan Zhang and D Grischkowsky. Waveguide terahertz time-domain spectroscopy of nanometer water layers. *Optics letters*, 29(14):1617–1619, 2004.

[113] Joseph S Melinger, N Laman, S Sree Harsha, ShuFan Cheng, and D Grischkowsky. High-resolution waveguide terahertz spectroscopy of partially oriented organic polycrystalline films. *The Journal of Physical Chemistry A*, 111(43):10977–10987, 2007.

[114] N Laman, S Sree Harsha, D Grischkowsky, and Joseph S Melinger. High-resolution waveguide thz spectroscopy of biological molecules. *Biophysical journal*, 94(3):1010–1020, 2008.

[115] Ugo Fano. Effects of configuration interaction on intensities and phase shifts. *Physical Review*, 124(6):1866, 1961.

[116] Amit Agrawal, Tatsunosuke Matsui, Z Valy Vardeny, and Ajay Nahata. Terahertz transmission properties of quasiperiodic and aperiodic aperture arrays. *JOSA B*, 24(9):2545–2555, 2007.

[117] Amit Agrawal, Z Valy Vardeny, and Ajay Nahata. Engineering the dielectric function of plasmonic lattices. *Optics express*, 16(13):9601–9613, 2008.

[118] T Otsuji, SA Boubanga Tombet, A Satou, H Fukidome, M Suemitsu, E Sano, V Popov, M Ryzhii, and V Ryzhii. Graphene-based devices in terahertz science and technology. *Journal of Physics D: Applied Physics*, 45(30):303001, 2012.

[119] Callum J Docherty and Michael B Johnston. Terahertz properties of graphene. *Journal of Infrared, Millimeter, and Terahertz Waves*, 33(8):797–815, 2012.

[120] Ta-Jen Yen, WJ Padilla, Nicholas Fang, DC Vier, DR Smith, JB Pendry, DN Basov, and Xiang Zhang. Terahertz magnetic response from artificial materials. *Science*, 303(5663):1494–1496, 2004.

[121] Willie J Padilla, Antoinette J Taylor, Clark Highstrete, Mark Lee, and Richard D Averitt. Dynamical electric and magnetic metamaterial response at terahertz frequencies. *Physical review letters*, 96(10):107401, 2006.

[122] Dibakar Roy Chowdhury, Xiaofang Su, Yong Zeng, Xiaoshuang Chen, Antoinette J Taylor, and Abul Azad. Excitation of dark plasmonic modes in symmetry broken terahertz metamaterials. *Optics express*, 22(16):19401–19410, 2014.

[123] Maidul Islam and Gagan Kumar. Terahertz surface plasmons propagation through periodically tilted pillars and control on directional properties. *Journal of Physics D: Applied Physics*, 49(43):435104, 2016.

[124] Sunil K Mathanker, Paul R Weckler, and Ning Wang. Terahertz (thz) applications in food and agriculture: A review. *Transactions of the ASABE*, 56(3):1213–1226, 2013.

[125] Weilu Gao, Jie Shu, Kimberly Reichel, Daniel V Nickel, Xiaowei He, Gang Shi, Robert Vajtai, Pulickel M Ajayan, Junichiro Kono, Daniel M Mittleman, et al. High-contrast terahertz wave modulation by gated graphene enhanced by extraordinary transmission through ring apertures. *Nano letters*, 14(3):1242–1248, 2014.

[126] Qian Zhao, Lei Kang, Bo Du, Bo Li, Ji Zhou, Hong Tang, Xiao Liang, and Baizhe Zhang. Electrically tunable negative permeability metamaterials based on nematic liquid crystals. *Applied physics letters*, 90(1):011112, 2007.

[127] NR Han, ZC Chen, CS Lim, B Ng, and MH Hong. Broadband multi-layer terahertz metamaterials fabrication and characterization on flexible substrates. *Optics express*, 19(8):6990–6998, 2011.

[128] Evren Ekmekci, Andrew C Strikwerda, Kebin Fan, G Keiser, X Zhang, G Turhan-Sayan, and RD Averitt. Frequency tunable terahertz metamaterials using broadside coupled split-ring resonators. *Physical Review B*, 83 (19):193103, 2011.

[129] Na Liu, Stefan Kaiser, and Harald Giessen. Magnetoinductive and electroinductive coupling in plasmonic metamaterial molecules. *Advanced Materials*, 20(23):4521–4525, 2008.

[130] Emil Prodan, Corey Radloff, Naomi J Halas, and Peter Nordlander. A hybridization model for the plasmon response of complex nanostructures. *science*, 302(5644):419–422, 2003.

[131] Zhanghua Han and Sergey I Bozhevolnyi. Plasmon-induced transparency with detuned ultracompact fabry-perot resonators in integrated plasmonic devices. *Optics express*, 19(4):3251–3257, 2011.

[132] Dibakar Roy Chowdhury, John F O'Hara, Antoinette J Taylor, and Abul K Azad. Orthogonally twisted planar concentric split ring resonators towards

strong near field coupled terahertz metamaterials. *Applied Physics Letters*, 104(10):101105, 2014.

[133] S Jagan Mohan Rao, Deepak Kumar, Gagan Kumar, and Dibakar Roy Chowdhury. Modulating the near field coupling through resonator displacement in planar terahertz metamaterials. *Journal of Infrared, Millimeter, and Terahertz Waves*, 38(1):124–134, 2017.

[134] Sher-Yi Chiam, Ranjan Singh, Carsten Rockstuhl, Falk Lederer, Weili Zhang, and Andrew A Bettiol. Analogue of electromagnetically induced transparency in a terahertz metamaterial. *Physical Review B*, 80(15):153103, 2009.

[135] Ranjan Singh, Carsten Rockstuhl, Falk Lederer, and Weili Zhang. Coupling between a dark and a bright eigenmode in a terahertz metamaterial. *Physical Review B*, 79(8):085111, 2009.

[136] Frank Hesmer, Eugen Tatartschuk, Oleksandr Zhuromskyy, Anna A Radkovskaya, Mikahil Shamonin, Tong Hao, Chris J Stevens, Grahame Faulkner, David J Edwards, and Ekaterina Shamonina. Coupling mechanisms for split ring resonators: Theory and experiment. *physica status solidi (b)*, 244(4): 1170–1175, 2007.

[137] O Sydoruk, E Tatartschuk, E Shamonina, and L Solymar. Analytical formulation for the resonant frequency of split rings. *Journal of applied physics*, 105(1):014903, 2009.

[138] Wendao Xu, Lijuan Xie, Jianfei Zhu, Xia Xu, Zunzhong Ye, Chen Wang, Yungui Ma, and Yibin Ying. Gold nanoparticle-based terahertz metamaterial sensors: mechanisms and applications. *ACS Photonics*, 3(12):2308–2314, 2016.

[139] Lijuan Xie, Weilu Gao, Jie Shu, Yibin Ying, and Junichiro Kono. Extraordinary sensitivity enhancement by metasurfaces in terahertz detection of antibiotics. *Scientific reports*, 5, 2015.

[140] Longqing Cong, Siyu Tan, Riad Yahiaoui, Fengping Yan, Weili Zhang, and Ranjan Singh. Experimental demonstration of ultrasensitive sensing with terahertz metamaterial absorbers: A comparison with the metasurfaces. *Applied Physics Letters*, 106(3):031107, 2015.

[141] Kailing Shih, Prakash Pitchappa, Manukumara Manjappa, Chong Pei Ho, Ranjan Singh, and Chengkuo Lee. Microfluidic metamaterial sensor: Selective trapping and remote sensing of microparticles. *Journal of Applied Physics*, 121(2):023102, 2017.

[142] Dibakar Roy Chowdhury, Ranjan Singh, John F O'Hara, Hou-Tong Chen, Antoinette J Taylor, and Abul K Azad. Dynamically reconfigurable terahertz metamaterial through photo-doped semiconductor. *Applied Physics Letters*, 99(23):231101, 2011.

[143] Shuang Zhang, Dentcho A Genov, Yuan Wang, Ming Liu, and Xiang Zhang. Plasmon-induced transparency in metamaterials. *Physical Review Letters*, 101(4):047401, 2008.